IN-91-CR
40380
P54

FINAL TECHNICAL REPORT

to the

NATIONAL AERONAUTICS AND SPACE ADMINISTRATION
URANUS DATA ANALYSIS PROGRAM

for

"INVESTIGATION OF THE SMALL-SCALE STRUCTURE AND DYNAMICS OF URANUS' ATMOSPHERE"

GRANT NAGW-1180

for the period
15 September 1987 through 31 March 1991

submitted by

Von R. Eshleman, Principal Investigator
Professor of Electrical Engineering
Durand Building, Room 221
(415) 723-3531

and

David P. Hinson, Associate Investigator
Senior Research Scientist
Durand Building, Room 219
(415) 723-3534

of the

Center for Radar Astronomy
Stanford University
Stanford, CA 94305-4055

(NASA-CR-188819) INVESTIGATION OF THE SMALL-SCALE STRUCTURE AND DYNAMICS OF URANUS' ATMOSPHERE Final Technical Report, 15 Sep. 1987 - 31 Mar. 1991 (Stanford Univ.) 54 p

N92-10960

CSCL 03B G3/91

Unclas
0040380

SUMMARY

This document constitutes the final technical report for grant NAGW-1180 of the Uranus Data Analysis Program, titled "Investigation of the small-scale structure and dynamics of Uranus' atmosphere." Professor Von R. Eshleman was the principal investigator. The grant covered the period 15 September 1987 through 31 March 1991, including a six-month no-cost extension.

Funding from this grant supported our contributions to the publication of three journal articles and one book chapter as well as the presentation of results at three conferences. A complete bibliography is given below. Copies of the journal articles are attached along with abstracts from the book chapter and the conference presentations.

This grant enabled a far more thorough analysis of radio occultation data obtained during the flyby of Uranus by the Voyager 2 spacecraft than would have been possible through funding from the Voyager Project alone. Consequently, this grant and others like it represent an essential component of the NASA program for Solar System exploration. Specifically, this research contributed to fundamental advances in our understanding of atmospheric dynamics on Uranus. The highlight of this study was the identification and characterization of a planetary-scale wave in the equatorial stratosphere. The resulting publication (Hinson and Magalhães 1991) currently represents the definitive work concerning atmospheric waves on Uranus and provides a foundation for future comparative studies of atmospheric dynamics on the planets of the outer Solar System. This paper also advanced our understanding of the influence of dissipating atmospheric waves on the photochemistry and circulation of the upper stratosphere.

PRECEDING PAGE BLANK NOT FILMED

BIBLIOGRAPHY

Journal Publications:

Eshleman, V. R., D. P. Hinson, G. F. Lindal, and G. L. Tyler 1987. Past and future of radio occultation studies of planetary atmospheres. *Adv. Space Res.* 7, (12)29-(12)32.

Hinson, D. P., and J. A. Magalhães 1991. Equatorial waves in the stratosphere of Uranus. *Icarus* **93**, in press.

Lindal, G. F., J. R. Lyons, D. N. Sweetnam, V. R. Eshleman, D. P. Hinson, and G. L. Tyler 1987. The atmosphere of Uranus: Results of radio occultation measurements with Voyager 2. *J. Geophys. Res.* **92**, 14987-15001.

Book Chapter:

Allison, M., R. F. Beebe, B. J. Conrath, D. P. Hinson, and A. P. Ingersoll 1991. Uranus' atmospheric dynamics and circulation. In *Uranus* (J. T. Bergstralh and E. D. Miner, Eds.), pp. 253-295. Univ. of Arizona Press, Tucson.

Abstracts and Presentations:

Hinson, D. P. Small-scale structure and dynamics in the atmosphere of Uranus. Presented at the Uranus Colloquium in Pasadena, CA, 28 June to 1 July, 1988 (hosted by the Jet Propulsion Laboratory, California Institute of Technology).

Hinson D. P., and V. R. Eshleman. Evidence for inertia-gravity waves in the stratosphere of Uranus derived from Voyager 2 radio occultation data. Presented at the 20th Annual meeting of the AAS Division for Planetary Sciences, 31 Oct. to 3 Nov. 1988, Austin, Texas. Abstract published in *Bull. American Astronom. Soc.*, vol. 20, no. 3, p. 822, 1988.

Hinson, D. P., and J. A. Magalhães. Planetary waves in the equatorial stratosphere of Uranus. Presented at the 22nd Annual meeting of the AAS Division for Planetary Sciences, 22-26 Oct. 1990, Charlottesville, Virginia. Abstract published in *Bull. American Astronom. Soc.*, vol. 22, no. 3, p. 1090, 1990.

Abstract of chapter published in *Uranus* (J. T. Bergstralh and E. Miner, Eds.), pp. 253-295, Univ. of Arizona Press, Tucson:

URANUS ATMOSPHERIC DYNAMICS AND CIRCULATION

MICHAEL ALLISON
NASA/Goddard Institute for Space Studies

RETA F. BEEBE
New Mexico State University

BARNEY J. CONRATH
NASA/Goddard Space Flight Center

DAVID P. HINSON
Stanford University

and

ANDREW P. INGERSOLL
California Institute of Technology

Uranus, with its 98° obliquity, apparently negligible internal heat source and methane-enriched, hydrogen-helium atmosphere, is a unique study in planetary meteorology. Although Voyager imaging measurements of cloud-tracked winds were disappointingly sparse, owing to the planet's low visual contrast and small number of discrete features, the available data indicate atmospheric rotation at midlatitudes nearly 200 m s^{-1} faster than that of the planetary magnetic field (presumably tied to the deep interior). Analysis of the dynamical deformation of the shape and size of isobaric surfaces measured by the Voyager radio-occultation experiment suggests a subrotating equator at comparable altitudes. Infrared temperature retrievals above the cloud deck indicate a smaller equator-to-pole contrast than expected for purely radiative-convective equilibrium, but show local variations implying a latitudinally correlated decrease with altitude in the cloud-tracked wind. While the speed of the differential motions is comparable to that on Jupiter and Saturn, the inferred shape of the zonal wind profile bears a surprising resemblance to the terrestrial circulation. If the observed flow is confined to the cloud layers, it implies an equator-to-pole temperature contrast that is not only much larger than that induced by direct solar heating but also of the opposite sign. Parametric models of the adjustment of the thermal structure by horizontal eddy fluxes successfully predict a reduced latitudinal contrast at infrared sounding levels, as compared with the radiative equilibrium value, but fail to reproduce the observed local variations in temperature and cloud-top winds. Despite the current uncertainties, the planet's unique external forcing and at least superficially simple flow structure (compared with the other Jovian planets) make the Uranian meteorology an important target for further observational and theoretical investigation.

Presented at the Uranus Colloquium in Pasadena, CA, 28 June to 1 July, 1988 (hosted by the Jet Propulsion Laboratory, California Institute of Technology).

Small-Scale Structure and Dynamics in the Atmosphere of Uranus

David P. Hinson
Center for Radar Astronomy
Stanford University, CA 94305

The dual-frequency radio occultation experiment conducted with Voyager 2 has provided new data on the equatorial atmosphere of Uranus. To date, results derived from these data include: temperature profiles extending from 0.3 to 2300 mb, a helium abundance of 15 ± 3% (from comparison with Voyager IRIS data), the detection of a thin CH_4 cloud deck near the 1.2 bar pressure level, a most likely value for the CH_4 mixing ratio below the cloud of about 2.3%, an equatorial radius and oblateness at the 1 bar pressure level of 25559 ± 4 km and 0.02293 ± 0.00080, respectively, and retrograde zonal winds of 110 ± 40 m/s near the equator. These results were obtained through analysis of gradual changes in the Doppler frequency of the signals received from the occulted spacecraft [Lindal *et al., JGR, 92,* 14987, 1987].

With this background, I am currently exploring another aspect of this experiment. The signals received during the occultation fluctuated rapidly in intensity and frequency as a result of scattering from small-scale refractive irregularities that are present throughout the troposphere and stratosphere. These scintillation data offer the only direct information currently available on atmospheric structure and dynamics on spatial scales of a few km or less. I have applied a scattering theory along with techniques of spectral analysis to the scintillation data, yielding solutions for physical characteristics of the scattering irregularities including their strength, size distribution, shape, orientation, and spatial distribution in the atmosphere. Two significant results have emerged from the research to date: the discovery of internal gravity waves propagating through the stratosphere, and the detection of closely spaced layers in the troposphere immediately above the CH_4 cloud deck.

The new result concerning internal gravity waves is remarkably similar to a previous result for Titan's atmosphere derived through analysis of radio occultation data from Voyager 1 [Hinson and Tyler, *Icarus, 54,* 337, 1983]. Taken together, these results represent a breakthrough in understanding the atmospheric process that underlies the ubiquitous intensity scintillations observed in both radio and stellar occultations by planetary atmospheres. With further analysis, I expect to estimate the wave fluxes of energy and momentum in the stratosphere of Uranus; the results will be compared to the analogous results from Titan, with possible implications for the energy balance and circulation of the tenuous upper atmospheres of both planets.

The results in the second area are more preliminary than those discussed above. Nevertheless, my analysis to date has revealed closely spaced layers in the troposphere between pressure levels of 500 and 1000 mb with a characteristic vertical separation of a few hundred meters -- a result that has strong implications for the theory for layered convection in the troposphere of Uranus [Gierasch and Conrath, *JGR, 92,* 15019, 1987]. This theory can explain some puzzling aspects of the observed temperature lapse rates and ortho/para H_2 ratio, and predicts a thickness for the convective layers on the order of tens to hundreds of meters, but there was until now no direct evidence supporting the existence of the proposed layers. By refining my initial results and extending the analysis to other pressure levels in the troposphere, I hope to provide a unique test of the theory for layered convection, which can lead in turn to improved understanding of the dynamics, the vertical stability, and the process of ortho/para conversion in the troposphere.

Presented at the 20th Annual meeting of the AAS Division for Planetary Sciences, 31 Oct. to 3 Nov. 1988, Austin, Texas. Abstract published in *Bull. American Astronom. Soc.*, vol. 20, no. 3, p. 822, 1988.

09.04

Evidence for Inertia-Gravity Waves in the Stratosphere of Uranus Derived from Voyager 2 Radio Occultation Data

D. P. Hinson and V. R. Eshleman (Stanford University)

The dual-wavelength (3.6 and 13 cm) radio signals received during the occultation of Voyager 2 by Uranus fluctuated rapidly in both intensity and phase as a result of scattering from small-scale refractive index irregularities that are present throughout the low-latitude (2° to 7° S) stratosphere and troposphere; we limit the present discussion to the stratosphere. We have applied a recently derived theory for strong scattering of radio waves (Hinson, *Radio Sci., 21*, 257, 1986) along with techniques of spectral analysis to these scintillation data, yielding solutions for characteristics of the scattering irregularities including their strength, size distribution, shape, orientation, and vertical distribution in the atmosphere. The observed vertical distribution of irregularities, when interpreted in the context of a theory for the propagation of fluid waves through the observed nonisothermal structure of the atmosphere of Uranus (Lindal *et al., JGR, 92*, 14987, 1987), gives compelling evidence that freely propagating inertia-gravity waves are the source of scattering. Rossby waves, though also consistent with the observed vertical distribution, seem less plausible as an explanation for the irregularities because their relatively small horizontal phase velocity leaves them susceptible to disruption by a weak vertical wind shear; acoustic waves are incompatible with the observations. At present, this conclusion applies to pressure levels between about 0.5 and 100 mb, where the low-pressure limit is a result of the signal-to-noise ratio of the experiment. The dominant observed vertical wavelength is a few kilometers, and the horizontal wavelength is constrained to be larger by a factor of about 100 or more, implying an upper limit to the wave frequency of $\omega < 2 \cdot 10^{-4}$ rad/sec. Future work will be directed toward: (1) estimating the energy and momentum fluxes of the waves, and (2) incorporating the results derived by French *et al.* (*Icarus, 51*, 491, 1982) through analysis of multiple-station observations of a stellar occultation by Uranus. In that case, observed intensity spikes were shown to be the result of scattering from refractive irregularities with a vertical scale of a few kilometers and a horizontal scale at least 60 times larger. This observation pertains to pressure levels of about 1-10 μb and latitudes of 18°S and 26°N. By comparing the radio occultation data to this and other stellar occultation data sets, it may be possible to characterize the dissipation of the waves and to estimate the wave-generated eddy diffusivity (*cf.* French and Gierasch, *J. Atmos. Sci., 31*, 1707, 1974).

Presented at the 22nd Annual meeting of the AAS Division for Planetary Sciences, 22-26 Oct. 1990, Charlottesville, Virginia. Abstract published in *Bull. American Astronom. Soc.*, vol. 22, no. 3, 1990.

16.01

Planetary Waves in the Equatorial Stratosphere of Uranus

D. P. Hinson and J. A. Magalhães (Stanford University)

We have identified and characterized an equatorial wave in the stratosphere of Uranus through analysis of radio occultation data from Voyager 2. Atmospheric waves modulate the ambient background structure of a planetary atmosphere, producing a distinctive spatial pattern of variations in density. This type of spatial modulation causes fluctuations in the phase and amplitude of signals received from a spacecraft during a radio occultation experiment. We compared observations of the stratosphere of Uranus at both immersion (2.0°N, 342.2°E) and emersion (6.3°N, 197.5°E) with predictions of the linear theory for equatorial waves on a β-plane. The observed vertical oscillations in atmospheric density agree closely with theoretical predictions for waves propagating vertically through the *observed* background structure of the stratosphere, providing compelling evidence for the presence of an atmospheric wave. Moreover, the observations at immersion and emersion are strikingly similar, suggesting a wave of planetary scale. The equivalent depth of the wave is 53 ± 12 m corresponding to a vertical wavelength of about 1/3 of a pressure scale height, and the wave amplitude at the 1-mb pressure level at immersion (emersion) is 1.1 ± 0.4 K (0.5 ± 0.2 K). The ratio of amplitudes at the two locations (2.1 ± 0.4, independent of pressure) is consistent with a wave that is latitudinally confined near the equator. Within the framework of the linear wave theory, quantitative comparisons between the measurements at the two locations have yielded constraints on the meridional and zonal structure of the wave. We have exploited these to identify two equatorial wave modes as the most likely explanations for the observations; each has the virtue of retaining a relatively simple spatial structure while accounting for the principal features of the data. The first mode is an inertia-gravity wave with westward zonal phase speed (relative to the mean zonal winds), a meridional index $j = 1$, and a zonal index $n = 6$. The second is an eastward inertia-gravity wave with $j = 2$ and $n = 14$. All Kelvin, Yanai, and Rossby wave modes are inconsistent with the observations. We will discuss the contribution by these wave modes to the eddy mixing and the energy and momentum budgets of the middle atmosphere.

Adv. Space Res. Vol. 7, No. 12, pp. (12)29–(12)32, 1987
Printed in Great Britain. All rights reserved.

0273–1177/87$0.00 + .50
Copyright © 1987 COSPAR

PAST AND FUTURE OF RADIO OCCULTATION STUDIES OF PLANETARY ATMOSPHERES

Von R. Eshleman,* David P. Hinson,* Gunnar F. Lindal** and G. Leonard Tyler*

**Center for Radar Astronomy, Stanford University, Stanford, CA 94305, U.S.A.*
***Jet Propulsion Laboratory, Pasadena, CA 91109, U.S.A.*

ABSTRACT

Measurements of radio waves that have propagated through planetary atmospheres have provided exploratory results on atmospheric constituents, structure, dynamics, and ionization for Venus, Mars, Titan, Jupiter, Saturn, and Uranus. Highlights of past results are reviewed in order to define and illustrate the potential of occultation and related radio studies in future planetary missions.

INTRODUCTION

The tenuous radio 'strings' that connect planetary spacecraft with earth are remarkably sensitive and versatile scientific sensors. For example they were 3 x 10(12) meters long for Voyager at Uranus in January, 1986, yet short-term perturbations to their phase path lengths as small as a millimeter could be measured with precision. One might think of the strings as having knots every few centimeters which mark each radio wavelength of 360 degrees of electrical phase, so that phase measurements can give this type of precision independent of the overall lengths of the strings. Regions that can perturb the phases and also the amplitudes of the signals include planetary atmospheres, ionospheres, surfaces, rings, and gravitational fields. Although only the radio techniques are discussed here, it should be apparent that a number of experimental methods are required to completely characterize these regions.

ATMOSPHERIC CONSTITUENTS

There are several different ways that radio occultation measurements, which are taken while spacecraft pass behind planets, have been fundamental in determining atmospheric constituents and their relative abundances. The phase path measurements can provide the vertical profile of atmospheric refractivity which is usually proportional to T/m, where T is the gas temperature and m is the mean molecular mass. For the determinations of H2 and He in the atmospheres of the giant planets given in Table 1, temperatures from the Voyager infrared instruments were used in conjunction with the radio results to find m and hence the relative abundance of the two main atmospheric constituents. The recent results for Uranus are explained in /1,2/. This same method was employed along with other experimental and theoretical considerations to reach the conclusion that nitrogen makes up nearly all of the dense atmosphere of Titan, as given in Table 1 /3,4/. There are theoretical reasons to expect that argon might be an important secondary constituent, although the measurements indicate that there could be essentially none. Hence the uncertainty shown in the table for the volume percentages of both N2 and Ar in Titan's atmosphere.

TABLE 1 Principal Atmospheric and Cloud Constituents

	Venus	Earth	Mars	Titan	Jupiter	Saturn	Uranus
1st const.	CO_2	N_2	CO_2	N_2	H_2	H_2	H_2
Vol. %	96.5	78	95	85-99	89	94	85
2nd const.	N_2	O_2	N_2	Ar?	He	He	He
Vol. %	3.5	21	2.7	0-15	11	6	15
Main Cloud const.	H_2SO_4	H_2O	H_2O	CH_4	NH_3	NH_3	CH_4
Vol.% Below Cloud	(15-30) X 10^{-4}	0 - 5 variable	0 - 1 variable	< 3	0.022	>0.007	2

Another method depends upon accurate measurements of the amplitudes of the radio signals during occultation to determine the absorptivity of the gas. When combined with profile information from the radio phase measurements and other considerations about likely or known constituents, this method has been used to determine the NH3 numbers of Table 1 for Jupiter and Saturn /5,6/, and to identify (H_2SO_4 vapor) and roughly quantify (15 to 30 parts per million) the absorber in the middle atmosphere of Venus /7/.

In a third method, the radio phase and amplitude measurements are used primarily to determine accurate refractivity profiles which sometimes clearly show that the atmosphere cannot be uniformly mixed. Additional considerations of wet and dry adiabats, vapor pressures, mixing ratios, static stability, radiative equilibrium, and the thermal and dynamic effects of condensation make it possible to home in on the probable amount of the condensible, non-uniformly-mixed constituent. This method has been used to obtain the Table1 result of less than 3% methane in the lower troposphere of Titan /4/ and the preliminary result of 2% methane below a CH_4 cloud deck in the troposphere of Uranus /1/. For example, the first result indicates that Titan is not covered by a ubiquitous methane ocean /8/, a popular early prediction, and the second shows that carbon is enhanced relative to the solar abundance by a factor of about 30, an important boundary condition in considerations of how Uranus was originally formed from icy planetesimals and nebular gases.

The other percentages for Venus and Mars in Table 1 (the column for earth is given for comparison) were obtained from other measurements, but radio occultation did provide early results such as the preponderance of CO_2 in the atmosphere of Mars at a time when most predictions were for mostly N_2 /9/. In this case, the total amount of atmospheric gas from radio occultation approximately equalled the amount of CO_2 from earth-based observations, so there was no possibility for a different major constituent.

ATMOSPHERIC STRUCTURE

Table 2 summarizes atmospheric pressure and temperature structures obtained by Voyager radio occultation for Titan /3,4/, Jupiter /5/, Saturn /6/ and Uranus /1/, and by various occultation and in situ measurements for Venus and Mars /10,11,12,13/. A black-body temperature for each planet is given for comparison. Mars is unique in that there are seasonal changes in surface pressure from the cycling of frozen CO_2 between polar caps. There are large seasonal, latitudinal, and weather variations in surface temperature for earth and Mars, mostly within the limits indicated in Table 2. The tropopause (t.p.) conditions and other temperatures also vary, but only nominal values are given for these. There are important latitudinal variations for Venus /11/ but again only nominal values are listed. Both Jupiter and Saturn display what appear to be the large-amplitude thermal effects of planetary waves in their low-latitude stratospheres /5,6/, but only average T's are shown in Table 2. In general, one should consult the original literature for more complete information on all of the material summarized in the tables.

Particular evidence on the sensitivity of the radio occultation technique is provided by the measurements made at Titan /3/. The results for the refractivity profiles on opposite sides of Titan, when expressed as atmospheric temperatures, have an rms temperature difference in the troposphere of only 0.2 K /4/. Since there are many independent measurements with height, this result simultaneously demonstrates the exceptional uniformity of Titan's equatorial troposphere, and the inherent potential sensitivity and precision of the radio technique for determining reliable results on atmospheric structure.

TABLE 2 Atmospheric Structure (p in mb, T in K; NA = not applicable or not available)

	Venus	Earth	Mars	Titan	Jupiter	Saturn	Uranus
p (surf.)	95000	1013	7 ± 1	1500	NA	NA	NA
T (surf.)	737	280±40	210±60	94	NA	NA	NA
p (t.p.)	300	100	NA	130	100	60	110
T (t.p.)	260	210	NA	71	110	82	52
T (1 mb)	180	265	170	165	160	135	NA
T (10 mb)	225	225	NA	143	145	105	68
T (100 mb)	245	210	NA	72	110	83	52
T (1000 mb)	345	280	NA	86	165	134	77
T (black body)	327	278	225	90	122	90	63

IONOSPHERES

Planetary ionospheres are complex and variable. Table 3 serves only as a general indicator of certain comparative features for the uppermost layer of each planet or moon, and as a reminder of the potential role of radio occultation for obtaining ionospheric profiles and for monitoring their temporal and positional variations. The giant planets in particular have several thin, dense, low-altitude layers of ionization /1,6,19/ In addition to this upper feature, and the extensive literature on other ionospheres measured by radio occultation with Mariner, Pioneer, Voyager and Soviet spacecraft includes /3,9,13,16,17,18/. The results for Uranus are preliminary, in Table 3 and also the other tables.

TABLE 3 Examples of Topside Ionospheres

	Venus	Earth	Mars	Io	Titan	Jupiter	Saturn	Uranus
Peak e^- concent. ($x10^{10}m^{-3}$)	50	50	15	7	<0.3	20	2	0.2?
Height of peak (km)	140	300	135	100	NA	1600	2000	4000?
Scale height (km)	25	120	30	90	NA	600	1000	2000?

OTHER RADIO RESULTS

Small-scale atmospheric irregularities cause amplitude and phase scintillations in the radio measurements. For example, freely propagating internal gravity waves were discovered in the atmosphere of Titan by this technique /20/, and related measurements can help in the study of atmospheric dynamics, wind shear, and even the planet's magnetic field orientation. Measurements on other aspects of the radio 'strings' have provided many of the basic numbers on planetary sizes, shapes, and masses that are summarized in Table 4, as well as wide-ranging results on planetary rings and surfaces. Precision is often very high. The equatorial radius of Titan, for example, is 2575.0 ± 0.5 km and its mean density is 1.881 ± 0.002 gm per cubic cm /4/.

TABLE 4 Size, Shape, and Mass (1000 mb reference level for the giant planets)

	Venus	Earth	Mars	Io	Titan	Jupiter	Saturn	Uranus
R_{eq} (km)	6051	6378	3397	1816	2575	71492	60268	25550
R_{pol} (km)	6051	6357	3372	1816	2575?	66854	54364	24950
Oblateness	~ 0	0.0034	0.0074	~ 0	~ 0?	0.0649	0.0980	0.023
Mass ($X\ 10^{24}$ kg)	4.87	5.98	0.642	0.089	0.135	1900	569	86.9
Density (gm cm^{-3})	5.25	5.52	3.94	3.54	1.88	1.33	0.688	1.27

FUTURE ATMOSPHERIC STUDIES

The Voyager experiments in particular have demonstrated the salutary effects of radio instrumentation that is well matched to the scientific potentials of the radio occultation technique. Highlights include a very stable spacecraft oscillator, versatile and accurate spacecraft orientation control to track the changing directions of the refracted radio ray paths, the use of two radio frequencies, and development of powerful signal- processing techniques.

Major improvements are feasible for future missions. Signal strengths could be improved by up to a factor of 10 thousand by reversing the direction of propagation to go from earth to spacecraft instead of from spacecraft to earth, so that the existing ground-based command and tracking transmitters could be used for the experiments. This would require spacecraft receivers and the development of advanced spacecraft signal processing units, which could also be used with other experiments to reduce telemetry requirements. Different types of experiments at different radio frequencies and polarizations would be enabled by this approach since the major part of the spacecraft instrumentation (the signal processor) would be common for all of them. Once this capability existed, the next major improvement would involve the use of simple transmitting sub-satellites to work with the main receiving spacecraft. This would make possible greatly increased atmospheric coverage. For example, with earth-spacecraft links in the studies of the major planets, only regions near the dawn and dusk terminators can be probed while all regions could be studied using links between two orbiting spacecraft.

There are many outstanding atmospheric problems that could be addressed in future radio experiments and, as in the past, these could be conducted in conjunction with refined radio studies of planetary surfaces and rings as well as with improved investigations of gravitational fields and certain relativistic phenomena. Atmospheric examples include: (1) detailed monitoring of Mars' weather including dust storm effects and their relationship to the nuclear-winter scenario for earth (several Viking measurements /13/ show extreme temperature inversions, apparently associated with dust storms, where the atmospheric temperature climbed from an unusually cold value of 170K at the surface to 225K at an altitude of 20 km); (2) study of the middle- atmospheric absorbing region on Venus /10/ and of the possible temporal variations of H_2SO_4 content with putative volcanism on Venus; (3) thorough investigations of the ammonia and methane cloud regions of the major planets and their global and possible temporal variations; (4) complete characterization of ionospheric profiles, particularly for the major planets; (5) high-precision monitoring of the Titan atmosphere including possible detection of long-term pressure changes if its atmosphere is buffered by nitrogen in solution in a hydrocarbon ocean; and (6) exploratory measurements in the Neptune-Triton system with Voyager in 1989, in the Pluto-Charon system with some future mission, and eventually in planetary systems of nearby stars.

ACKNOWLEDGEMENT

This work was supported by the National Aeronautics and Space Administration.

REFERENCES

1. G.L. Tyler, D.N. Sweetnam, J.D. Anderson, J.K. Campbell, V.R. Eshleman, D.P. Hinson, G.S. Levy, G.F. Lindal, E.A. Marouf, and R.A. Simpson, Voyager 2 radio science observations of the Uranian system: Atmosphere, rings, and satellites, Science 233, 79 (1986)

2. R. Hanel, B. Conrath, F.M. Flasar, V. Kunde, W. Maguire, J. Pearl, J. Pirraglia, R. Samuelson, D. Cruikshank, D. Gautier, P. Gierasch, L. Horn, and P. Schulte, Infrared observations of the Uranian system, Science 233, 70 (1986)

3. G.L. Tyler, V.R. Eshleman, J.D. Anderson, G.S. Levy, G.F. Lindal, G.E. Wood, and T.A. Croft, Radio science investigations of the Saturn system with Voyager 1: Preliminary results, Science 212, 201 (1981)

4. G.F. Lindal, G.E. Wood, H.B. Hotz, D.N. Sweetnam, V.R. Eshleman, and G.L. Tyler, The atmosphere of Titan: An analysis of the Voyager 1 radio occultation measurements, Icarus 53, 348 (1983)

5. G.F. Lindal, G.E. Wood, G.S. Levy, J.D. Anderson, D.N. Sweetnam, H.B. Hotz, B.J. Buckles, D. P. Holmes, P.E. Doms, V.R. Eshleman, G.L. Tyler, and T.A. Croft, The atmosphere of Jupiter: An analysis of the Voyager radio occultation measurements, J. Geophys. Res. 86, 8721 (1981)

6. G.F. Lindal, D.N. Sweetnam, and V.R. Eshleman, The atmosphere of Saturn: An analysis of the Voyager radio occultation experiment, Astron. J. 90, 1136 (1985)

7. P.G. Steffes, Laboratory measurements of the microwave opacity and vapor pressure of sulfuric acid vapor under simulated conditions for the middle atmosphere of Venus, Icarus 64, 576 (1985)

8. V.R. Eshleman, G.F. Lindal, and G.L. Tyler, Is Titan wet or dry? Science 221, 53 (1983)

9. A. Kliore, D.L. Cain, G.S. Levy, V.R. Eshleman, G. Fjeldbo, and F.D. Drake, Occultation experiment: Results of the first direct measurements of Mars's atmosphere and ionosphere, Science 149, 1243 (1965)

10. G. Fjeldbo, A.J. Kliore, and V.R. Eshleman, The neutral atmosphere of Venus as studied with the Mariner V radio occultation experiments, Astron. J. 76, 123 (1971)

11. A.J. Kliore and I.R. Patel, Thermal structure of the atmosphere of Venus from Pioneer Venus radio occultation, Icarus 52, 320 (1982)

12. D.M. Hunten, L. Colin, T.M. Donahue, V.I. Moroz, Venus, Univ. Arizona Press, Tucson 1983

13. G.F. Lindal, H.B. Hotz, D.N. Sweetnam, Z. Shippony, J.P. Brenkle, G.V. Hatsell, R.T. Spear, and W.H. Michael, Jr., Viking radio occultation measurements of the atmosphere and topography of Mars: Data acquired during one Martian year of tracking, J. Geophys. Res. 84, 8443 (1979)

14. C.W. Snyder, The planet Mars as seen at the end of the Viking mission, J. Geophys. Res. 84, 8487 (1979)

15. M.A. Kolosov, A.V. Sokolov, and O.I. Yakovlev, Investigation of radiowave propagation in the solar system, IEEE Trans. AP-27, 18 (1979)

16. G.S. Ivanov-Kholodny, M.A. Kolosov, N.A. Savich, Y.N. Alexandrov, M.B. Vasilyev, A.S. Vyshlov, V.M. Dubrovin, A.L. Zaitsev, A.V. Michailov, G.M. Petrov, V.A. Samovol, L.N. Samoznaev, A.I. Sidorenko, and A.F. Hasyanov, Daytime ionosphere of Venus as studied with Veneras 9 and 10 radio occultation , Icarus 39, 209 (1979)

17. A.J. Kliore, G. Fjeldbo, B.L. Seidel, D.N. Sweetnam, T.T. Sesplaukis, P.M. Wolceshyn, and S.I. Rasool, The atmosphere of Io from Pioneer 10 radio occultation measurements, Icarus 24, 407 (1975)

18. Mariner Stanford Group, Venus: Ionosphere and atmosphere as measured by dual-frequency radio occultation of Mariner V, Science 158, 1678 (1967)

19. G. Fjeldbo, A. Kliore, B. Seidel, D. Sweetnam, and P. Woiceshyn, The Pioneer 11 radio occultation measurements of the Jovian ionosphere, in: Jupiter, ed. T. Gehrels, Univ. Arizona Press, Tucson 1976, p. 238

20. D.P. Hinson and G.L. Tyler, Internal gravity waves in Titan's atmosphere observed by radio, Icarus 54, 337 (1983)

ICARUS 93, 000–000 (1991)

4535

Equatorial Waves in the Stratosphere of Uranus

DAVID P. HINSON

Center for Radar Astronomy, Stanford University, California 94305-4055

AND

JULIO A. MAGALHÃES

NASA Ames Research Center, Moffett Field, California 94035

Received January 25, 1991; revised June 17, 1991

We have identified and characterized an equatorial wave in the stratosphere of Uranus through analysis of radio occultation data from Voyager 2. Our methodology relies on two physical phenomena: (1) atmospheric waves modulate the ambient background structure of a planetary atmosphere, producing a distinctive pattern of spatial variations in temperature and density; and (2) this type of spatial modulation in turn causes fluctuations in the phase and amplitude of radio signals received from an occulted spacecraft. We compared predictions of the linear theory for equatorial waves on a β-plane with observations of the stratosphere at both immersion (2.0°N, 342.2°E) and emersion (6.3°N, 197.5°E). (Note that the latitude system used here is the reverse of the IAU convention.) The observed quasi-periodic vertical variations in atmospheric density agree closely with theoretical predictions for a wave propagating vertically through the observed background structure of the stratosphere, providing compelling evidence for the presence of an atmospheric wave. The wave has an equivalent depth of 53 ± 12 m, a vertical wavelength of about one-third of a pressure scale height, and an amplitude at the 1-mbar pressure level at immersion (emersion) of 1.1 ± 0.4 K (0.5 ± 0.2 K). Within the framework of the linear wave theory, quantitative comparisons between the measurements at immersion and emersion yielded constraints on the meridional and zonal structure of the wave. The ratio of amplitudes at the two locations, 2.1 ± 0.3, is consistent with a wave confined in latitude near the equator. Moreover, the observations at immersion and emersion are correlated, suggesting a wave of planetary scale. These constraints allowed us to identify two equatorial wave modes as equally likely alternatives for explaining the observations; each retains a relatively simple spatial structure while accounting for the principal features of the data. The first is an inertia–gravity wave with westward zonal phase speed (relative to the mean zonal winds), a meridional index $j = 1$, and a zonal wavenumber $n = 6$. The second is an eastward inertia–gravity wave with $j = 2$ and $n = 14$. All Kelvin, Yanai, and Rossby wave modes are inconsistent with the observations. We expect the wave to begin breaking near the 200-μbar pressure level, resulting in an eddy diffusion coefficient of about 0.6 to 1.0 × 10^4 cm^2 sec^{-1}, consistent with independent estimates of this parameter. Vertical transfer of momentum by the wave could accelerate the mean zonal wind at pressures less than 200 μbar by about ±10–20 cm sec^{-1} per planet rotation. © 1991 Academic Press, Inc.

INTRODUCTION

After a journey spanning more than 8 years, 30 astronomical units, and encounters with both Jupiter and Saturn, the Voyager 2 spacecraft visited Uranus in late January 1986. The sequence of observations conducted during the flyby included a radio occultation experiment to study the equatorial atmosphere of Uranus. Results already derived from these data include (Lindal *et al.* 1987): the first profiles of electron density in the ionosphere, a temperature profile extending from 0.25 to 2300 mbars, a helium abundance (from comparison with Voyager IRIS data) of 15 ± 3% by volume, the detection of a thin methane cloud deck near the 1200-mbar pressure level, a methane mixing ratio below the cloud of about 2.3%, an equatorial radius and oblateness at the 1000-mbar pressure level of 25,559 ± 4 km and 0.02293 ± 0.00080, respectively, and a zonal wind speed of −110 ± 40 m sec^{-1} (retrograde) near the equator. With these results serving as a foundation, we have identified and characterized an atmospheric wave in the equatorial stratosphere through further analysis of the radio occultation data. This characterization includes well-determined basic parameters, such as the amplitude and vertical wavelength, as well as tentative estimates of the contribution by the wave to the momentum budget and eddy mixing of the middle atmosphere. [We follow Andrews *et al.* (1987) in defining the middle atmosphere as the region bounded below by the tropopause and above by the homopause.] Some of our results concerning this equatorial wave appeared in a preliminary form in the comprehensive review of atmospheric dynamics on Ura-

0019-1035/91 $3.00
Copyright © 1991 by Academic Press, Inc.
All rights of reproduction in any form reserved.

nus by Allison *et al.* (1991).

This investigation is based on observations of relatively rapid, deterministic variations in the amplitude and phase of signals received from an occulted spacecraft. These signal fluctuations arise as a result of propagation of radio waves through an atmosphere whose background structure has been modulated in temperature and density by an atmospheric wave. When interpreted in the context of the linear theory for atmospheric waves along with the scalar theory for diffraction of electromagnetic waves, these data constitute a valuable resource for remote sensing of atmospheric dynamics.

In addition to deriving new and unique results concerning atmospheric dynamics on Uranus, we have also improved the basic methodology employed in this type of investigation, which originated in a closely related study of atmospheric dynamics on Titan (Hinson and Tyler 1983). Signal fluctuations observed during the radio occultation of Voyager 1 led Hinson and Tyler to consider the behavior of an internal gravity wave in a nonisothermal atmosphere. They derived a simple, approximate expression for the response of a vertically propagating wave to the background atmospheric structure—in the absence of wind shear and dissipation, the amplitude of the wave varies with altitude in a manner prescribed by the background static stability and its vertical variations. For their central result, Hinson and Tyler applied this formula in conjunction with measurements of the background thermal structure and static stability of Titan's atmosphere (Lindal *et al.* 1983) to identify the distinctive signature of an atmospheric wave in the radio occultation data from Voyager 1. In the course of the present investigation, we have improved this technique in two important respects. First, we applied a rigorous theory for atmospheric waves to interpret the observations rather than the somewhat heuristic theory employed previously. Second, we extended the analysis to include observations of both phase and amplitude fluctuations, whereas the earlier work considered only amplitude data. These improvements in the methodology, and their successful application to data from Uranus, have enhanced the credibility of this technique for remote sensing of atmospheric waves.

An earlier investigation of equatorial waves in the atmosphere of Jupiter by Allison (1990) provided not only strong motivation but also substantial guidance for the research reported here. Allison determined the vertical structure of the wave modes on Jupiter from the Voyager radio occultation measurements and deduced the meridional and zonal structure from Voyager images of the equatorial atmosphere. The combination of these complementary observations proved effective for identifying and characterizing the predominant wave mode—a meridionally confined Rossby wave—that is present in the upper troposphere and lower stratosphere of Jupiter's equatorial atmosphere. There is, however, one significant difference between our approach and the one employed by Allison. As Voyager images of the equatorial atmosphere of Uranus are bland and featureless, we were forced to rely exclusively on radio occultation data as the only direct source of information concerning the equatorial wave. Despite this limitation, we were able to derive substantial, quantitative conclusions from the radio occultation data alone. This result is both surprising and significant, with implications for future studies of equatorial waves in planetary atmospheres.

It has been noted widely that the profile of atmospheric structure on Uranus retrieved from the radio occultation data by Lindal *et al.* (1987) exhibits distinctive, large-scale temperature inflections in the stratosphere. Their vertical scale (~50 km) exceeds the pressure scale height. As part of this investigation, we considered the possibility that these thermal features represent the signature of a vertically propagating atmospheric wave. However, we found the data to be incompatible with this hypothesis, at least within the simple theoretical framework adopted here. A more plausible case can be made for interpreting these large-scale temperature inflections as part of the static thermal structure of the equatorial atmosphere, although the supporting evidence is admittedly circumstantial. In any event, the atmospheric wave identified in this study is distinct from these thermal features and has a vertical wavelength significantly smaller than a scale height.

We have constrained the scope of this investigation in several respects. We restrict our attention to data from the stratosphere and focus on the effect of the wave on the eddy mixing and momentum budget of the middle atmosphere. Considerations of data from the troposphere and of questions such as the origin of the wave are deferred to future work. To compensate for the scarcity of data, we also adopted some simplifying assumptions. Namely, we interpret the observations in terms of a single, monochromatic wave mode; the data are insufficient for a meaningful study of wave transience or of superpositions of wave modes. Moreover, arguments concerning the energy balance of the middle atmosphere favor the conclusion that the wave has an upward vertical group velocity, which we will assume throughout.

Equatorial waves have been studied extensively in the terrestrial atmosphere (e.g., Andrews *et al.* 1987 and references cited therein). By their nature, they are strongly influenced by planetary rotation acting through the Coriolis force. Given our geocentric perspective, it is therefore natural when considering this type of wave to employ a latitude–longitude coordinate system where the north pole coincides with the planet's angular momentum vector. We adopt this convention for use here; specifically, the sunlit hemisphere of Uranus at the time of the Voyager 2 flyby is defined to be the northern hemisphere (cf. Fig.

4525

1, below). The more widely used IAU coordinate system (Davies *et al.* 1983), which has the poles reversed, is inappropriate for this investigation. When intercomparing results, the reader should note that the IAU system was adopted in some (e.g., Lindal *et al.* 1987, Flasar *et al.* 1987) but not all (e.g., Connerney *et al.* 1987) of the references cited herein.

This paper is organized as follows. We begin with a general description of the occultation experiment and introduce results derived previously that are essential to this investigation. We then derive fundamental results concerning the behavior of radio waves propagating through a planetary atmosphere. We continue with an explanation of the procedures for data reduction, followed by a discussion of the theory for equatorial waves. The next section reports the results of model calculations concerning occultation measurements of equatorial waves. We identify and characterize the equatorial wave in the stratosphere of Uranus by applying this methodology to the phase data. We then discuss the possible effect of the wave on the momentum budget and eddy mixing of the middle atmosphere. The final section of the paper gives a summary of the relative reliability of the various results. In Appendix A we consider the characteristics of the large-scale inflections in the temperature profile retrieved from the radio occultation data. We present complementary results derived from amplitude data in Appendix B.

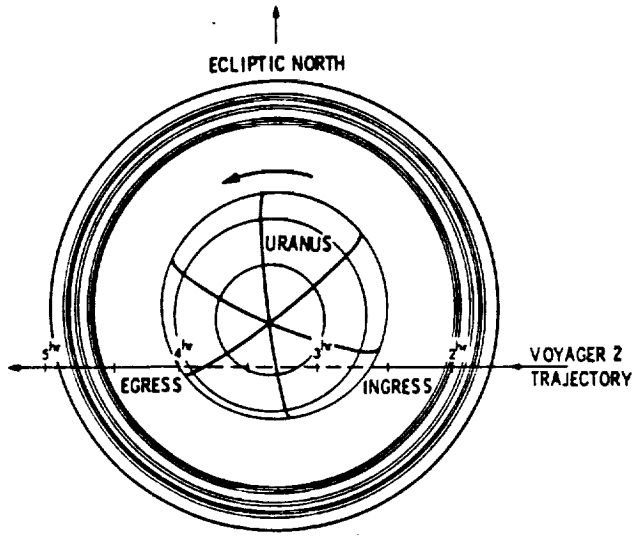

FIG. 1. View from Earth showing the trajectory of Voyager 2 past Uranus (from Lindal *et al.* 1987). During the occultation, the spacecraft-to-planet distance was about 2×10^5 km or about 8 planet radii.

EXPERIMENT DESCRIPTION

The Voyager 2 spacecraft carries a temperature-controlled "ultrastable" quartz oscillator (USO) designed to provide a steady reference signal at a frequency near 19 MHz (cf. Eshleman *et al.* 1977). During the occultation by Uranus, the spacecraft employed the USO in generating a pair of signals at coherently related frequencies (wavelengths) of 2296 MHz (13.1 cm) and 8420 MHz (3.6 cm) with an exact frequency ratio of 3 : 11. These signals are commonly referred to as *s*-band and *x*-band, respectively. Both signals were amplified and transmitted continuously without modulation in right-circular polarization through the 3.7-m-diameter spacecraft antenna. By virtue of the quality of the USO, stochastic variations in the frequency of the radiated signals did not exceed a few parts in 10^{12} over the time scales of interest here (about 1–100 sec).

The signals transmitted by Voyager 2 during the occultation by Uranus were received by two ground antennas in Australia, each 64 m in diameter, one at the NASA Canberra Deep Space Communications Complex and the other at the Parkes Radio Astronomy Observatory (cf. Tyler *et al.* 1986). The Canberra station recorded data at both wavelengths, while the Parkes station recorded data only at 3.6 cm. Each received signal was amplified, filtered, heterodyned (mixed) to baseband, digitized to 8-bit samples, and recorded on computer tapes at sampling rates of 50,000 and 80,000 sec^{-1} at Canberra and Parkes, respectively. All receiving equipment was designed to operate without degrading the inherent frequency stability of the signals radiated by Voyager 2. This combination of spacecraft and ground equipment yielded preimmersion and postemersion signal-to-noise ratios in a 1-Hz bandwidth of about 2500 (34 dB) and 12,600 (41 dB) at wavelengths of 13.1 and 3.6 cm, respectively.

Before describing the experiment geometry, we introduce a few useful physical concepts. The fundamentals of radio occultation measurements can be understood using the theory of geometrical optics, which arises from Maxwell's equations in the limit of small wavelengths (Born and Wolf 1975, p. 109). Within this theoretical framework, the energy emitted by the spacecraft can be visualized as a ray of radiation that traces a distinct path to Earth. The specific trajectory followed by the ray corresponds to a stationary value of the path integral of refractive index from transmitter to receiver (Fermat's principle). Incorporating some elements of the theory of diffraction, the effective transverse dimensions of this narrow beam of radiation are comparable in size to the radius of the first Fresnel zone (Born and Wolf 1975, p. 370). For the segment of the ray path near Uranus, this dimension is several kilometers, as determined by the experiment geometry, the wavelength of the radio signal, and the physical properties of the atmosphere of Uranus.

Figure 1 shows the experiment geometry. Prior to the occultation by Uranus, the signals transmitted by Voyager 2 followed a straight-line path to Earth with a one-way propagation time of 2^h45^m. Immersion to occultation by

4525 Cos/am/KL

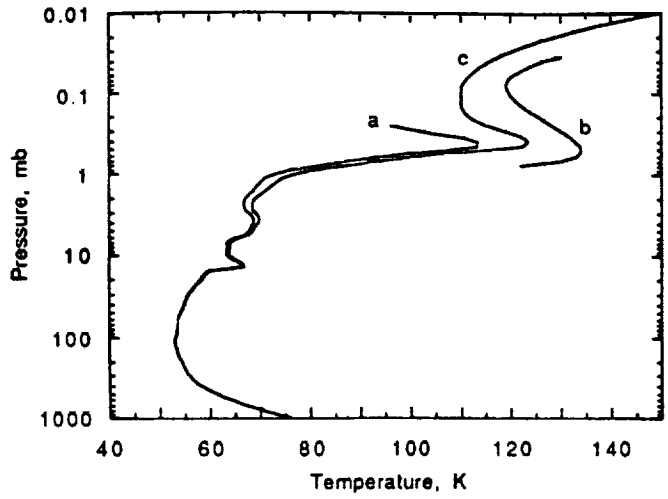

FIG. 2. Background thermal structure in the equatorial atmosphere of Uranus. (a) Temperature profile derived from radio occultation data (Lindal *et al.* 1987). (b) Temperature profile obtained from observation of solar occultation with UVS instrument (Bishop *et al.* 1990). (c) Composite profile used in this investigation.

the neutral atmosphere occurred at 20:36 UTC (spacecraft event time) on January 24, 1986. From this time until emersion, the signals followed a ray path that intercepted the atmosphere of Uranus and curved distinctively in response to atmospheric gradients of refractive index. Over the first half of the occultation, the ray path swept progressively deeper into the equatorial atmosphere, reaching a maximum pressure of about 2300 mbars midway through the occultation (Lindal *et al.* 1987). The ray path then reversed its descent and sampled for a second time but at a different location the atmospheric structure at pressures less than 2300 mbars.

Figure 2 shows key results concerning the thermal structure in the equatorial atmosphere of Uranus. The radio occultation experiment yielded a temperature profile for pressures between 0.25 and 2300 mbars (Lindal *et al.* 1987), while the UVS instrument on Voyager 2 provided complementary results at pressures less than 0.8 mbar through observations of a solar occultation (Herbert *et al.* 1987, Bishop *et al.* 1990). In the region of overlap, the radio occultation profile (curve a) is about 20 K colder than the UVS profile of Bishop *et al.* (curve b), but both exhibit a local temperature maximum near 0.4 mbar and the two profiles appear to be consistent within their respective uncertainties. [We note in passing that the temperature lapse rate is not well determined near the upper boundary of the radio occultation profile (cf. Lindal *et al.* 1987); hence, the significance of the near-adiabatic lapse rate near the 0.3-mbar pressure level in this profile is open to question.] We constructed a smoothly varying temperature profile (curve c) that is consistent with both sets of observations for use in this investigation. The composite profile has the following properties: at high pressures (>10 mbars) and low pressures (<10 μbars) it asymptotically approaches the radio occultation profile of Lindal *et al.* and the UVS solar occultation profile of Herbert *et al.*, respectively. At a pressure of 0.4 mbar, the composite profile has a temperature that falls about midway between the profiles of Lindal *et al.* and Bishop *et al.* This characterization of the ambient thermal structure of the equatorial atmosphere provides an essential foundation for studies of vertically propagating atmospheric waves.

A note on our motivation for constructing the composite temperature profile is in order. We derive our most important results using data from pressures within the range covered by the radio occultation profile (curve a); the corresponding portion of the composite profile is indispensable to this investigation. Nevertheless, the extension of the profile to lower pressures is necessary in that it allows us to establish the noise baseline of the measurements, to search for a weak signature of atmospheric waves at low pressures, and to model wave behavior at pressures where the measurement sensitivity is insufficient for direct observations.

The composite profile exhibits local maxima in temperature near pressures of 14, 4, and 0.4 mbar, with temperature minima near 9, 2, and 0.1 mbar. We explored the possibility that a vertically propagating wave could be responsible for these temperature inflections, but we found the data to be inconsistent with this hypothesis, as explained in Appendix A. Alternatively, these thermal features could be a consequence of aerosol heating. The general agreement between the locations of the temperature maxima and the respective condensation levels of ethane, acetylene, and diacetylene provides circumstantial evidence in favor of this hypothesis (Pollack *et al.* 1987). Support for this interpretation can also be found in earlier work by Appleby (1986), who studied the energy balance in the atmosphere of Uranus using radiative–convective equilibrium models. His results suggest that aerosol heating is needed to explain the relatively warm temperatures observed in the stratosphere. Hence, the weight of the evidence favors an interpretation in which these thermal features are static rather than dynamic. In the remainder of this paper we treat the temperature inflections in Fig. 2 as part of the background structure of the stratosphere through which waves propagate. As we show in subsequent sections, the wave perturbations to the thermal structure of the stratosphere are smaller in both magnitude and vertical scale than these thermal features.

We now introduce a compact notation for characterizing the geometry of the experiment. The instantaneous ray path from spacecraft to Earth can be labeled conveniently using the coordinates of periapsis—the point of closest

approach to Uranus, where the maximum pressure is encountered along the ray path through the atmosphere. (We apply the term "periapsis" with a view of the ray path as the trajectory of a photon.) We computed the coordinates of periapsis (latitude, longitude, and atmospheric pressure) as a function of time using the reconstruction of the Voyager 2 trajectory provided by the Voyager Navigation Team, the results on atmospheric composition derived by Lindal *et al.* (1987) and Conrath *et al.* (1987), and the composite profile of thermal structure shown in Fig. 2. For example, the coordinates of periapsis were 2.0°N, 342.2°E and 6.3°N, 197.5°E at the 1-mbar pressure level during immersion and emersion, respectively. The latitudes and longitudes varied by less than 0.1° and 1°, respectively, about these values when the pressure at periapsis ranged from 0.001 to 10 mbars. [For a definition of the latitude–longitude system used here, see the Introduction and Connerney *et al.* (1987).]

The duration of the experiment must be considered carefully when interpreting the observations. The ray path swept between periapsis pressures of 0.001 and 10 mbars, the range of interest here, in 73 and 78 sec during immersion and emersion, respectively. These elapsed times are smaller by orders of magnitude than the period of all atmospheric waves that we consider to be plausible interpretations of the data. Hence, we can ignore the time development of the waves during the measurement interval at immersion or emersion; the data provide a snapshot of the atmospheric structure at these two locations. However, we account for the time offset between immersion and emersion, about 84 m, in our interpretation of the results.

PROPAGATION OF RADIO WAVES

The atmosphere of Uranus imposed a distinctive signature on the radio waves propagating from the occulted Voyager 2 spacecraft to Earth, influencing both the amplitude and phase of the signals received at the ground antennas. In this section we derive fundamental relationships between the spatial structure of the occulting atmosphere and the properties of the received signals. Our intention is to explain in simple terms the information contained in the radio occultation measurements while avoiding mathematical complexity; more rigorous treatments of this problem have been reported elsewhere (e.g., Haugstad 1978, Hubbard *et al.* 1978, Hinson 1986). The relationships derived here provide an essential foundation for interpreting the observations.

We are interested primarily in effects on the received signals caused by wave-like spatial variations in atmospheric refractive index. It is therefore convenient to express the refractive index as $1 + \bar{\nu} + \nu'$, where $\bar{\nu}$ is the zonal mean component representing the background structure of the atmosphere and ν' is the perturbation caused by an atmospheric wave. For simplicity, we initially ignore the influence of $\bar{\nu}$ on the measurements; it is relatively small at the atmospheric pressures of interest here (<10 mbars). The results are generalized to include the effect of the background structure in Appendix B.

We begin by noting the physical proportions of the experiment. The distance, D_1, from Voyager 2 to Uranus during the occultation was about 2×10^5 km while the distance, D_2, from Uranus to Earth was about 3×10^9 km. Both D_1 and D_2 greatly exceeded the effective length, L, of the ray path through the atmosphere of Uranus, about 2400 km as given by the geometrical mean of the pressure scale height and the circumference of the planet. Under these conditions we can treat the atmosphere of Uranus as a thin "phase-changing" screen (cf. Salpeter 1967, Bramley 1977, Hubbard *et al.* 1978), which means that the atmosphere directly modulates the phase but not the amplitude of radio waves propagating through it. Amplitude perturbations develop through the phenomenon of diffraction only during subsequent propagation between Uranus and Earth (cf. French and Lovelace 1983).

Figure 3 shows the idealized experiment geometry. As noted above, $D_2 \gg D_1$. In addition, λ, the vacuum wavelength of the radio signal, is much smaller than l, the characteristic scale of variations in atmospheric refractive index. Under these conditions, we can use the Fresnel diffraction formula (e.g., Goodman 1968, pp. 59–61) to express the signal received at the ground antenna:

$$V \approx -\frac{iV_0}{\lambda D_1}\int_{-\infty}^{+\infty}\int_{-\infty}^{+\infty} \exp\left[i\frac{(x - x')^2 + (z - z')^2}{\lambda D_1} + i\psi_{\text{mod}}(x', z')\right]dx'dz'. \quad (1)$$

Here, V is the complex voltage measured across the antenna "terminals" and V_0 is the voltage that would be observed in the absence of the phase screen. We have suppressed the time dependence $e^{-i2\pi ft}$, where f is the frequency of the transmitted signal. The quantity ψ_{mod} is the phase modulation imposed on the radio waves emerging from the screen. The coordinates x and z denote the location of the transmitter and receiver in the directions transverse to the phase screen (cf. Fig. 3), while x' and z' are variables of integration. The surface of integration coincides with the plane of the phase screen, $y = 0$.

As a consequence of the thin-screen approximation, ψ_{mod} can be expressed as a path integral of refractive index:

$$\psi_{\text{mod}}(x, z) = \frac{2\pi}{\lambda}\int_0^L \nu'(x, y, z)dy. \quad (2)$$

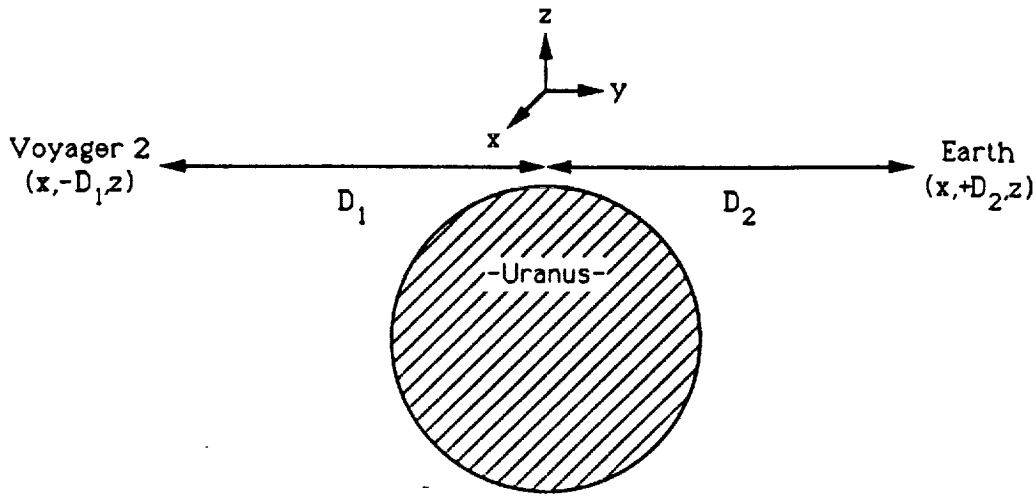

FIG. 3. Schematic representation of a radio occultation experiment. We model the occulting atmosphere as a thin phase-changing screen in the plane $y = 0$. Coordinate axes are defined so that a straight line from spacecraft to Earth coincides with the y-direction and the local acceleration of gravity at periapsis in the occulting atmosphere is opposite to the z-direction.

In a subsequent section, we present model calculations of ψ_{mod} corresponding to an occultation by an atmosphere containing planetary-scale equatorial waves. However, for the present discussion of basic principles it is more convenient to consider an idealized form for ψ_{mod}. The occultation data support the conclusion that the wave observed in the stratosphere of Uranus has a horizontal wavelength that exceeds its vertical wavelength by several orders of magnitude. Accordingly, we restrict the present derivation to the case where the occulting atmosphere contains no horizontal variations in refractive index so that ψ_{mod} is independent of x. This simplifies the discussion without changing the main conclusions. Specifically, we consider the simple case where

$$\psi_{mod}(x, z) = \psi_0 \cos(2\pi z/l) \tag{3}$$

and

$$\psi_0 \ll 1.$$

This corresponds to weak, periodic phase modulation of magnitude ψ_0 with spatial period l in the vertical direction. Substitution from (3) into (1) and integration yields

$$v \equiv V/V_0 \approx 1 + i\psi_0 \cos(2\pi z/l) \exp(-i\pi\lambda D_1/l^2), \tag{4}$$

where v is the normalized voltage. From Eq. (4) we can identify a and ψ, the weak perturbations to the amplitude and phase, respectively, of the received signal:

$$a \equiv |v| - 1 \approx \psi_0 \cos(2\pi z/l) F_a \tag{5}$$

$$\psi \equiv \tan^{-1}[\mathrm{Im}(v)/\mathrm{Re}(v)] \approx \psi_0 \cos(2\pi z/l) F_\psi. \tag{6}$$

Here, a is dimensionless while ψ is measured in radians. We have defined

$$F_a \equiv \sin(\pi\lambda D_1/l^2) \tag{7}$$

$$F_\psi \equiv \cos(\pi\lambda D_1/l^2). \tag{8}$$

Both a and ψ are direct projections of ψ_{mod}. The respective constants of proportionality, F_a and F_ψ, are sinusoidal functions whose argument involves the ratio of $\sqrt{\lambda D_1}$, the radius of the first Fresnel zone, to l, the transverse spatial scale of the phase modulation. The effects of diffraction enter through F_a and F_ψ, which are commonly referred to as Fresnel filters.

Figure 4 illustrates the variation of F_a and F_ψ with l for the occultation of Voyager 2 by Uranus. Note that F_ψ approaches unity for $l > 2\sqrt{\lambda D_1} \approx 6$ km. Over these spatial scales, the effects of diffraction on the phase data are negligible, and the phase perturbations of the received signal provide a direct measure of the phase modulation imposed by the occulting atmosphere. In contrast, the amplitude perturbations arise as a direct consequence of diffraction and are characterized by an enhanced response to spatial structure in the phase screen of Fresnel-zone size or smaller. Specifically, F_a approaches zero for large l, and the variations in the phase screen that are most efficient at producing amplitude perturbations satisfy $l <$ 6 km. For these reasons, phase data can provide a more sensitive measure than amplitude data of atmospheric structure on relatively large spatial scales. As we are

4525

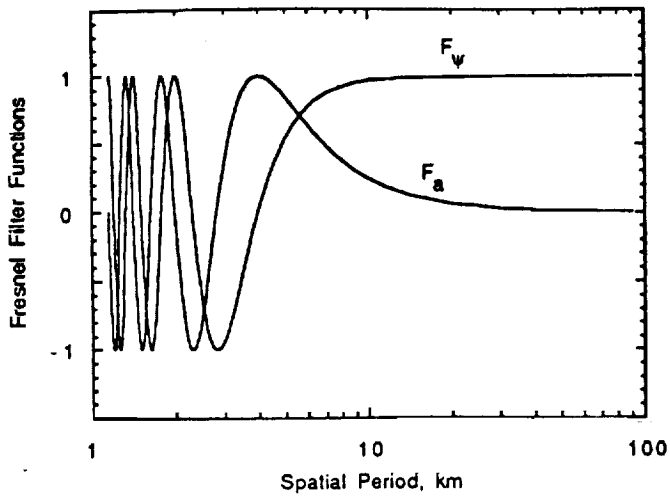

FIG. 4. Fresnel filter functions F_a and F_Ψ computed from Eqs. (7) and (8), respectively; we used parameter values appropriate to the occultation of Voyager 2 by Uranus: $\lambda = 3.6 \times 10^{-5}$ km (x-band), $D_1 = 2.2 \times 10^5$ km, and $\sqrt{\lambda D_1} = 2.8$ km. An atmospheric wave modulates the amplitude and phase of a signal received in an occultation experiment; the two curves show how the *magnitude* of the signal perturbations varies as a function of l, the spatial period of ψ_{mod} [cf. Eqs. (5) and (6)].

interested primarily in structure on vertical scales of about 10 km, these considerations led us to rely primarily on phase data in our investigation of waves in the stratosphere of Uranus. This is not to suggest that amplitude measurements are merely redundant. To the contrary, the two data types have dramatically different sensitivities to the various sources of noise in the experiment. With this in mind, we treated the amplitude and phase data as complementary measures of atmospheric structure and tested the reliability of our measurements both through intercomparison of results derived from either phase or amplitude data alone and through computation of correlations.

DATA REDUCTION

At Stanford, we received computer tapes containing the data from Canberra and Parkes. During the initial steps of data reduction, we applied established techniques of digital signal processing to isolate signal parameters of interest (cf. Bracewell 1986, Oppenheim and Schafer 1975, Brigham 1974). First, we used a band-pass filter to reduce the sampling rate by a factor of 16; at the same time we converted the data from real to complex representation. This step reduced data volume by removing thermal noise while preserving all useful information contained in the radio signals. Second, we mixed the data with a unit amplitude signal; the frequency of this reference signal was prescribed to vary gradually in such a way that the long-term variations ($\gtrsim$100 sec) in Doppler frequency would be removed from the data. This step is needed as preparation for subsequent analysis; as our interest here centers on short-term signal variations, it had no appreciable effect on our results. Finally, we obtained measures of signal amplitude, A, and phase, Ψ, through use of two techniques, which yielded the same results for the data considered here. The first involved spectral analysis (cf. Lipa and Tyler 1979). The second began with additional filtering for bandwidth reduction; A and Ψ were then calculated directly for each data sample by exploiting the complex representation of the signal as a rotating vector. Of the two techniques, the former is more robust while the latter is simpler. These steps yielded time histories, $A(t)$ and $\Psi(t)$, at sampling rates of 12.21 and 9.77 sec^{-1} for data from Canberra and Parkes, respectively. We chose these sampling rates as a compromise between lower values which reduce noise effects and higher values which provide finer spatial resolution. For these sampling rates, the separation in periapsis altitude of successive samples was about 700 m.

By using dual signals at coherently related frequencies, we can distinguish between effects arising in the neutral atmosphere of Uranus and those caused by its ionosphere. This is possible because the refractive index of a plasma varies with frequency while that of a neutral gas does not for the frequencies considered here. Within the domain of geometrical optics, the neutral atmosphere causes a phase shift in the radio signals that is inversely proportional to λ and, hence, exactly 11/3 times larger at x-band than at s-band [cf. Eq. (2)]. Conversely, the ionosphere introduces phase perturbations that are larger at s-band than at x-band by the same factor. Hence, we can largely remove plasma effects from the phase measurements, leaving only the effect of the neutral atmosphere, by computing the phase difference:

$$\Psi_n = \frac{121}{112}\left(\Psi_x - \frac{3}{11}\Psi_s\right). \tag{9}$$

The "s" and "x" subscripts refer to s- and x-bands, respectively. With this normalization, Ψ_n corresponds to the phase effect of the neutral atmosphere at x-band.

This approach to removing plasma effects has two limitations. First, we have neglected diffraction which can introduce additional dispersive effects at the two signal frequencies beyond those already accounted for in Eq. (9) [cf. Eqs. (6) and (8)]. This equation must be applied with caution when diffraction effects are important, as occurs when the occulting atmosphere includes appreciable variations in refractive index on spatial scales comparable to $\sqrt{\lambda D_1}$. Second, in adopting Eq. (9) we implicitly assumed that the two signals trace coincident ray paths to Earth. This is not always the case; differences can arise between ray trajectories as a result of the frequency dependence

4525

of refractive index in the ionosphere. When applied to the occultation data from Uranus, however, this equation yielded well-behaved results and neither limitation appeared to have a significant effect.

Subsequent steps of data analysis were designed specifically for the study of atmospheric waves whose vertical wavelength is smaller than a pressure scale height (~35 km in the stratosphere). [The large-scale (~50 km) inflections that appear in the temperature profile retrieved from the radio occultation data are considered separately in Appendix A.] The basic strategy is straightforward: isolate the signature of such waves in the radio occultation data through use of an appropriate filter. In this case the desired filter is one that removes effects due to the background structure of the atmosphere, which have spatial scales comparable to a pressure scale height, while preserving all effects that appear on smaller spatial scales. We chose for this purpose a particularly simple filter based on least-squares fitting of quadratic polynomials; it is characterized by a single parameter d, the effective spatial scale of the filter. Before applying the filter, we first labeled all data samples, $\Psi(t)$ and $A(t)$, with tags to indicate the pressure and altitude at periapsis for the corresponding ray path from spacecraft to Earth. We then implemented the filter by applying the following procedure to each sample of data: (1) find the periapsis altitude, z, of the data sample of interest; (2) identify all data samples with periapsis altitudes that fall within an interval d centered on z; (3) fit a quadratic polynomial by least squares to this segment of data using time as the independent variable; (4a) for phase measurements, compute the difference between the central data sample and the value of the fitted polynomial at altitude z; this "phase residual" represents one sample of output from the filter; (4b) for amplitude measurements, compute the difference as in step (4a), then normalize the result by the value of the fitted polynomial at altitude z to obtain one output sample [cf. Eqs. (4) and (5)]. We repeated this process for all input data samples, Ψ and A, yielding phase residuals, ψ, and amplitude residuals, a, which are the basis of all subsequent analysis and interpretation. The operation of the filter can be expressed compactly as follows:

$$\psi(z) = \Psi(z) - \Psi_{ls}(z, d) \tag{10}$$

$$a(z) = [A(z) - A_{ls}(z, d)]/A_{ls}(z, d). \tag{11}$$

Here, the argument z refers to the periapsis altitude of a data sample. The functions $\Psi_{ls}(z, d)$ and $A_{ls}(z, d)$ represent the quadratic polynomials fitted by least squares to a segment of data centered at z and spanning an interval d in periapsis altitude. The polynomials are evaluated at altitude z in computing the right-hand side of each equation. A new solution for the polynomials is obtained for each value of z.

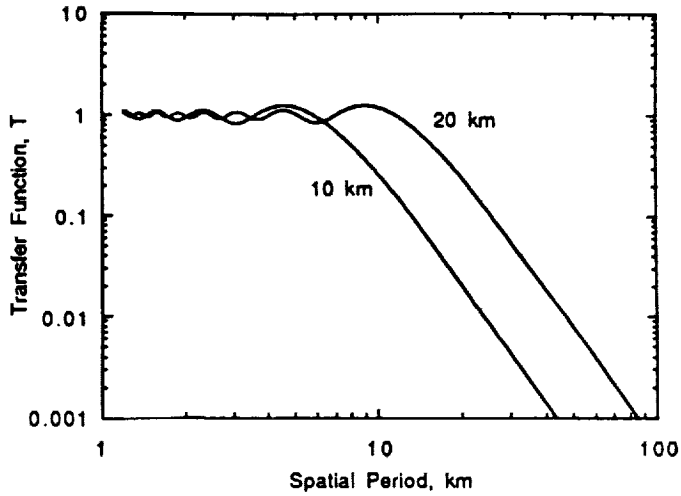

FIG. 5. Characteristics of the spatial filter applied to the radio occultation data. The dimensionless transfer function, T, gives the ratio of filter output to input when the latter is a unit amplitude sinusoid of spatial period l. The two curves correspond to different values of d, the altitude interval used in filtering.

Hamming (1989) provides a good discussion of this type of filter. Its performance can be characterized quantitatively through use of a dimensionless transfer function, $T(l)$, defined as the ratio of filter output to input when the latter is a unit amplitude sinusoid with spatial period l. Figure 5 shows examples of T computed for two values of d. The filter strongly attenuates Fourier components of the input signal with spatial periods of about $d/2$ or larger. Consequently, the output signal comprises approximately the Fourier components of the input signal with periods smaller than about $d/2$, but with a slight distortion introduced by the small oscillations of T about unit value for small l.

We attempted to optimize the performance of the least-squares filter for the present application using two approaches. First, we applied the filter to the occultation data and explored the sensitivity of a and ψ to variations in the choice of d. We show representative examples in a subsequent section (cf. Fig. 11). Second, we generated test data using a model atmosphere that consisted of wave-like temperature oscillations superimposed on a background structure similar to that observed for Uranus (cf. Fig. 2). We then applied the filter to the simulated measurements to study its performance while systematically varying d as well as the amplitude and vertical scale of the waves. On the basis of these exercises, we selected 20 km as an effective value for d.

As the 64-m antennas at Parkes and Canberra are separated by about 300 km, the signals received at these two stations traced different ray paths from spacecraft to Earth. However, for the geometry of this experiment, the

separation of the rays within the atmosphere of Uranus never exceeded about 20 m. It is therefore not surprising that the x-band data recorded at the two antennas are highly correlated and exhibit virtually identical time histories of signal variations caused by the atmosphere of Uranus. In comparing these data sets, we determined that the amplitude data from Parkes and the phase data from Canberra were of noticeably higher quality than their respective counterparts. For the sake of brevity, we show only the higher quality data in all figures presented below. However, we obtained mutually consistent results when we analyzed the complete data from each antenna independently.

We restricted our attention to data from pressures less than 10 mbars for several reasons. First, these data are sufficient to derive a reasonably complete characterization of the wave in the equatorial stratosphere of Uranus. By focusing on these data, we can derive significant results while limiting the complexity of the analysis. Second, the amplitude of a vertically propagating atmospheric wave generally increases exponentially with decreasing pressure. The signature of an atmospheric wave is therefore easier to distinguish from the effect of the background structure of the atmosphere at lower pressures, at least within the pressure range accessible through radio occultation measurements. Moreover, the wave amplitude is enhanced in regions where the background stability of the atmosphere is high. The static stability in the atmosphere of Uranus generally increases with decreasing pressure (cf. Fig. 2) which again favors measurements at relatively low pressures. Finally, data at greater pressures are more difficult to interpret because the signal-to-noise ratio of the radio occultation data generally decreases with increasing pressure. For these and other reasons, we deferred analysis of data from pressures exceeding 10 mbars to future work.

The results obtained from these steps of data reduction are shown below in Figs. 8, 9, and B2. Before discussing these data in more detail, however, we turn our attention to the theory for atmospheric waves that will be used to interpret them.

THEORY OF ATMOSPHERIC WAVES

In this section we derive equations governing the behavior of atmospheric waves near the equator of a rotating planet. Although this subject has been discussed extensively in the literature (e.g., Andrews *et al.* 1987, Gill 1982, Beer 1978, Allison 1990), we require certain results that are not included in standard treatments of this problem; for this reason we include a complete derivation here.

The following approximations are inherent in this dynamical model. We treat the atmosphere as an ideal gas. We consider only wave motion that weakly perturbs the background state of the atmosphere, and we linearize all equations accordingly. We assume that a hydrostatic balance is maintained in the vertical direction. We neglect the Coriolis force associated with the horizontal component of the rotation vector of Uranus. We model the curvature of the planet near the equator through use of a β-parameter, defined below, which amounts to the approximation $\sin\theta \approx \theta$, where θ is the planetographic latitude. Finally, we model the background circulation of the atmosphere near the equator as a uniform zonal flow without horizontal or vertical shear. This is potentially the most serious limitation of the theory; we discuss the possible effect of wind shear on our results in a subsequent section.

We adopt a Cartesian coordinate system rotating with angular frequency Ω, the rotation rate of Uranus, and with origin at the equator at a distance r_0 from the center of the planet. The x and y coordinates coincide with the eastward and northward directions, respectively. Under conditions of hydrostatic equilibrium, it is convenient to introduce a log-pressure vertical coordinate,

$$\hat{z} \equiv \ln(p_s/p), \tag{12}$$

where p is pressure and p_s is a reference value. In linearizing the dynamical equations, we express all variables as the sum of a zonal mean component, denoted by an overbar, and a perturbation due to the wave, denoted by a prime. For example, $u = \bar{u} + u'$, where u is the zonal wind. We also use a geopotential function defined as

$$\phi(x, y, \hat{z}, t) \equiv \int_{z_s}^{z(\hat{z})} g\,dz, \tag{13}$$

where g is the acceleration of gravity, z is geometric height, and z_s is a reference value. These definitions and approximations lead to the following set of equations:

$$\left(\frac{\partial}{\partial t} + \bar{u}\frac{\partial}{\partial x}\right)u' - \beta y v' + \frac{\partial \phi'}{\partial x} = -X' \tag{14}$$

$$\left(\frac{\partial}{\partial t} + \bar{u}\frac{\partial}{\partial x}\right)v' + \beta y u' + \frac{\partial \phi'}{\partial y} = -Y' \tag{15}$$

$$\frac{\partial \phi'}{\partial \hat{z}} - RT' = 0 \tag{16}$$

$$\frac{\partial u'}{\partial x} + \frac{\partial v'}{\partial y} + \frac{\partial \hat{w}'}{\partial \hat{z}} - \hat{w}' = 0 \tag{17}$$

$$\left(\frac{\partial}{\partial t} + \bar{u}\frac{\partial}{\partial x}\right)\frac{\partial \phi'}{\partial \hat{z}} + \Gamma \hat{w}' = -Z'. \tag{18}$$

Here, t is time; R is the gas constant; u', v', and $\hat{w}' \equiv d\hat{z}/dt$ are the eastward, northward, and upward components,

TABLE I
Physical Characteristics of the Equatorial Stratosphere of Uranus

Parameter	Definition	Value
r_0	Radius of planet[a]	25,737 km
Ω	Rotation rate of magnetic field	1.0124×10^{-4} sec^{-1}
β	Latitudinal gradient of Coriolis parameter	7.9×10^{-9} km^{-1} sec^{-1}
f_{H_2}	Mole fraction of H_2	85%
f_{He}	Mole fraction of He	15%
R	Gas constant	3.6×10^7 erg g^{-1} K^{-1}
c_p	Specific heat at constant pressue (for mixture[b])	9.5×10^7 erg g^{-1} K^{-1}
g	Gravitational acceleration[a]	853 cm sec^{-2}
g/c_p	Adiabatic lapse rate[a]	0.90 K km^{-1}
$\bar{T}$	Background temperature[a]	77 K
H	Scale height[a]	32 km
Γ	Stability parameter[a]	0.18 km^2 sec^{-2}
α	Constant of proportionality between ρ' and ν'	0.86 g cm^{-3}

[a] Value given at 1-mbar pressure level for vertically varying parameters.
[b] Assuming "frozen equilibrium" hydrogen.

respectively, of fluid velocity associated with the wave; $\hat{w}'$ is in units of pressure scale heights per unit time; ϕ' and T' are the wave perturbations to geopotential and temperature, respectively. The terms X', Y', and Z' represent dissipation which results from effects such as molecular viscosity, Rayleigh friction, and Newtonian cooling. For the immediate derivation we assume that X', Y', and Z' are negligible so that the wave motion is isentropic and inviscid. The stability parameter Γ is defined as

$$\Gamma(\hat{z}) = R\left(\frac{\partial \bar{T}}{\partial \hat{z}} + \frac{R\bar{T}}{c_p}\right) = H^2N^2, \tag{19}$$

where c_p is the specific heat at constant pressure; $\bar{T}(\hat{z})$ is the temperature of the unperturbed atmosphere; the scale height $H = R\bar{T}/g$; and N is the buoyancy frequency. Under the conditions imposed above, Γ is a function of $\hat{z}$ only. Finally, β is the latitudinal gradient of f, the Coriolis parameter, at the equator:

$$f = 2\Omega \sin\theta \tag{20}$$

$$\beta = \left.\frac{\partial f}{\partial y}\right|_{y=0} = \frac{2\Omega}{r_0}. \tag{21}$$

Table I lists parameter values for the equatorial stratosphere of Uranus.

The quantities measured most directly in a radio occultation experiment are ν' and ρ', the wave perturbations to the atmospheric refractive index and density, respectively. In the present application, $\rho' = \alpha\nu'$, where the factor α depends on the molecular weights, microwave properties, and relative abundances of the constituent gases in the atmosphere. In the stratosphere of Uranus, α is nearly constant with the value given in Table I. Moreover, the following relation applies for adiabatic motion of an ideal gas in hydrostatic equilibrium:

$$\rho'(x, y, \hat{z}, t) = -\frac{\bar{\rho}}{R\bar{T}}\frac{\partial \phi'}{\partial \hat{z}} \tag{22}$$

Here, $\bar{\rho}(\hat{z})$ is the density of the unperturbed atmosphere; from the ideal gas law, $\bar{\rho} \propto e^{-\hat{z}}/\bar{T}$. In the discussion that follows, we obtain solutions for ϕ' that satisfy Eqs. (14)–(18). We can then compute ρ' and ν' from Eq. (22).

We seek solutions with longitudinal and temporal variations of the form $e^{i(n/r_0)(x-ct)}$, where c is the zonal phase speed measured relative to $\bar{u}$, and n is the zonal wavenumber. The wave frequency for an observer moving with the mean flow is $\sigma \equiv cn/r_0$. We adopt the convention that n is always positive so that c and σ are negative for a wave traveling toward the west. With this assumption about the dependence of the solutions on x and t, Eqs. (14)–(18) can be reduced to a single equation for v':

$$\frac{\partial^2 v'}{\partial y^2} - \left(\frac{n}{r_0}\right)^2 v' - \frac{\beta}{c}v' + \left(\frac{\partial}{\partial \hat{z}} - 1\right)\frac{(\beta y)^2 + (cn/r_0)^2}{\Gamma}\frac{\partial v'}{\partial \hat{z}} = 0. \tag{23}$$

We can simplify this equation through separation of variables:

$$v'(x, y, \hat{z}, t) = V(y) \cdot G(\hat{z}) \cdot e^{i(n/r_0)(x-ct)}. \tag{24}$$

Substitution into (23) yields distinct equations for the vertical and meridional structure:

$$\left(\frac{d}{d\hat{z}} - 1\right)\left(\Gamma^{-1}\frac{dG}{d\hat{z}}\right) + \frac{G}{gh} = 0 \tag{25}$$

$$\frac{d^2V}{dy^2} + \left[\frac{(cn/r_0)^2 - (\beta y)^2}{gh} - \left(\frac{n}{r_0}\right)^2 - \frac{\beta}{c}\right]V = 0. \tag{26}$$

We have introduced a separation constant gh, where h is the so-called equivalent depth.

To match the observations (cf. Fig. 9 below), we seek solutions to Eq. (25) such that the oscillations in $G(\hat{z})$ are rapid compared to the gradual vertical variations of Γ. We

can therefore solve Eq. (25) through use of the WKB approximation,

$$G(\hat{z}) \approx G_0 \frac{\Gamma^{1/2} e^{\hat{z}/2}}{[\mu(\hat{z})]^{1/2}} \exp\left[\pm i \int^{\hat{z}} \mu(\hat{z}')d\hat{z}'\right], \quad (27)$$

where G_0 is a dimensionless complex constant and

$$\mu(\hat{z}) \approx \left(\frac{\Gamma}{gh} - \frac{1}{4}\right)^{1/2}. \quad (28)$$

In this expression for $\mu(\hat{z})$, the vertical wavenumber, we have neglected terms that involve vertical derivatives of Γ; these are negligible for the wave considered here.

The general solutions to Eq. (26) comprise the parabolic cylinder functions (Lebedev 1972). Among these, we consider only solutions that remain bounded as $y \to \pm\infty$:

$$V(y) = (2^j j! \pi^{1/2})^{-1/2} e^{-\eta^2/2} H_j(\eta), \quad (29)$$

where j, the meridional index of the solution, is a nonnegative integer (0, 1, 2, . . .) and

$$\eta \equiv y/L_y, \quad L_y \equiv (\sqrt{gh}/\beta)^{1/2}. \quad (30)$$

The parameter L_y appears as a characteristic length scale in the meridional direction. The functions $H_j(\eta)$ are Hermite polynomials [e.g., $H_0(\eta) = 1$, $H_1(\eta) = 2\eta$, $H_2(\eta) = 4\eta^2 - 2$]. The requirement for bounded solutions yields the dispersion relation:

$$2j + 1 = \frac{\sqrt{gh}}{\beta}\left[\frac{(cn/r_0)^2}{gh} - \left(\frac{n}{r_0}\right)^2 - \frac{\beta}{c}\right]. \quad (31)$$

We can express ϕ' in terms of this solution for v' through Eqs. (14), (17), and (18):

$$\phi'(x, y, \hat{z}, t) = \frac{ir_0/n}{1 - (c^2/gh)}\left(\frac{dV(y)}{dy} - \beta y V(y)\right) \cdot G(\hat{z}) \cdot e^{i(n/r_0)(x - ct)}. \quad (32)$$

Substitution into (22) yields solutions for ρ' and v'.

To complete the derivation, we must consider a special case not covered by Eq. (23). Equations (14)–(18) allow a solution where v' is identically zero. In this case, the simplified equations can be solved to yield

$$\phi'(x, y, \hat{z}, t) \equiv \Phi(y) \cdot G(\hat{z}) \cdot e^{i(n/r_0)(x - ct)}, \quad (33)$$

where

$$\Phi(y) = \frac{c}{\pi^{1/4}} e^{-\eta^2/2}. \quad (34)$$

The solution for $G(\hat{z})$ and the definition of η are the same as before. The dispersion relation for this mode, commonly known as the Kelvin wave, is particularly simple:

$$c = +\sqrt{gh}. \quad (35)$$

As with Eq. (31), this expression is a consequence of the requirement that the solutions remain bounded as $y \to \pm\infty$.

We now introduce the traditional nomenclature applied to these solutions and briefly describe the behavior of each mode (see also Allison 1990). First, it is convenient to define a dimensionless frequency, ω, and zonal wavenumber, k:

$$\omega \equiv \frac{cn/r_0}{(\beta\sqrt{gh})^{1/2}} \quad (36)$$

$$k \equiv \left(\frac{\sqrt{gh}}{\beta}\right)^{1/2}\left(\frac{n}{r_0}\right). \quad (37)$$

With these definitions, Eq. (31) becomes

$$\omega^3 - [k^2 + (2j + 1)]\omega - k = 0. \quad (38)$$

This cubic equation for $\omega(k)$ can be solved exactly through standard techniques (e.g., Abramowitz and Stegun 1972, p. 17).

According to Eq. (35), the *Kelvin wave* propagates without dispersion and the zonal phase speed is exclusively eastward relative to the mean flow. Expressed in terms of ω and k, Eq. (35) becomes

$$\omega = k. \quad (39)$$

Combining Eqs. (22) and (33), the meridional variation of ρ' for the Kelvin wave can be expressed as

$$\rho' \propto e^{-\eta^2/2}. \quad (40)$$

We consider next the solution where the meridional index $j = 0$, commonly referred to as the *Yanai wave*. Of the three solutions to Eq. (38) for this case, one must be rejected since it yields nonphysical results. The remaining two valid solutions are

$$\omega = \frac{1}{2}\left[k \pm \left(k^2 + 4\right)^{1/2}\right]. \quad (41)$$

In the limit where $k \to \infty$, the roots corresponding to the

plus and minus signs approach the familiar behavior of an internal gravity wave propagating eastward and a Rossby wave propagating westward, respectively, at temperate latitudes. Accordingly, this mode is often referred to as a mixed Rossby–gravity wave. From Eqs. (22), (29), and (32), we obtain the meridional variation of ρ' for the Yanai wave:

$$\rho' \propto \eta e^{-\eta^2/2}. \tag{42}$$

Equation (38) has three distinct solutions when $j \geq 1$:

$$\omega_1 = 2 \cdot B \cdot \cos\left(\frac{\delta}{3}\right)$$

$$\omega_2 = 2 \cdot B \cdot \cos\left(\frac{\delta}{3} + \frac{2\pi}{3}\right) \tag{43}$$

$$\omega_3 = 2 \cdot B \cdot \cos\left(\frac{\delta}{3} - \frac{2\pi}{3}\right),$$

where

$$B \equiv \left[\frac{k^2 + (2j+1)}{3}\right]^{1/2}$$

$$\cos\delta \equiv \frac{k}{2B^3}.$$

The first two modes are *inertia–gravity waves* traveling eastward and westward, respectively, relative to the mean flow. The third solution, a *Rossby wave*, propagates exclusively toward the west. As with the Yanai wave, the nomenclature is indicative of the asymptotic behavior as $k \to \infty$. From Eqs. (22), (29), and (32), we obtain the meridional variation of ρ' for these three modes:

$$\rho' \propto \left\{\frac{\omega}{k}[2jH_{j-1}(\eta) - \eta H_j(\eta)] - \eta H_j(\eta)\right\} e^{-\eta^2/2}. \tag{44}$$

We computed $\omega(k)$ from Eqs. (39), (41), and (43), as well as representative results for the meridional variations of ρ' from Eqs. (40), (42), and (44); these appear in Figs. 6 and 7, respectively. For future reference, we also give an explicit expression for the vertical variation of ρ'. Combining Eqs. (22), (27), and (32) or (33), we obtain

$$\rho' \propto G_0 \cdot (\bar{\rho}N^3)^{1/2} \cdot \exp\left[\pm i \int^{\hat{z}} \mu(\hat{z}')d\hat{z}'\right]. \tag{45}$$

This expression is more accurate than the simple, heuristic result derived previously by Hinson and Tyler (1983),

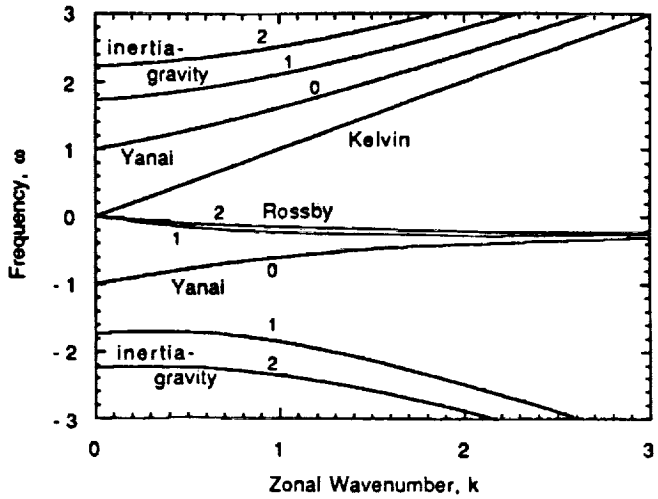

FIG. 6. Dispersion diagram for equatorial waves. The zonal phase speed, ω/k, of inertia–gravity and Yanai waves can be either eastward ($\omega > 0$) or westward ($\omega < 0$), while the Kelvin waves (Rossby waves) propagate exclusively eastward (westward). Numbers adjacent to curves indicate values of j for Yanai, inertia–gravity, and Rossby wave modes.

although the main difference is that the exponent of N is 3/2 rather than 2. In practice, this amounts to a small correction. Equation (45) is valid for all the equatorial wave modes.

MODEL CALCULATIONS

We previously considered the general effect of wave-like atmospheric structure on occultation measurements [cf. Eqs. (3), (5), and (6)]. We now extend those results by considering a more realistic model for the occulting atmosphere, one that consists of an equatorial wave propagating vertically through the background structure observed in the atmosphere of Uranus. Our objective is to relate the three-dimensional spatial structure of the atmospheric wave to phase perturbations measured in an occultation experiment. Specifically, we use model calculations to demonstrate the validity of a key approximation that simplifies the interpretation of the data.

The behavior of vertically propagating atmospheric waves depends sensitively on the vertical structure and static stability of the unperturbed atmosphere through the parameter Γ [cf. Eqs. (19), (27), and (28)]. For the present application, we computed $\Gamma(\hat{z})$ from the composite profile of thermal structure in the equatorial atmosphere that appears in Fig. 2.

We implemented the model calculations as follows. First, we selected an equatorial wave mode and specified the complete spatial structure of the associated variations in atmospheric density and refractive index using the equations derived earlier. For example, we considered

4525

Dg/am/KR

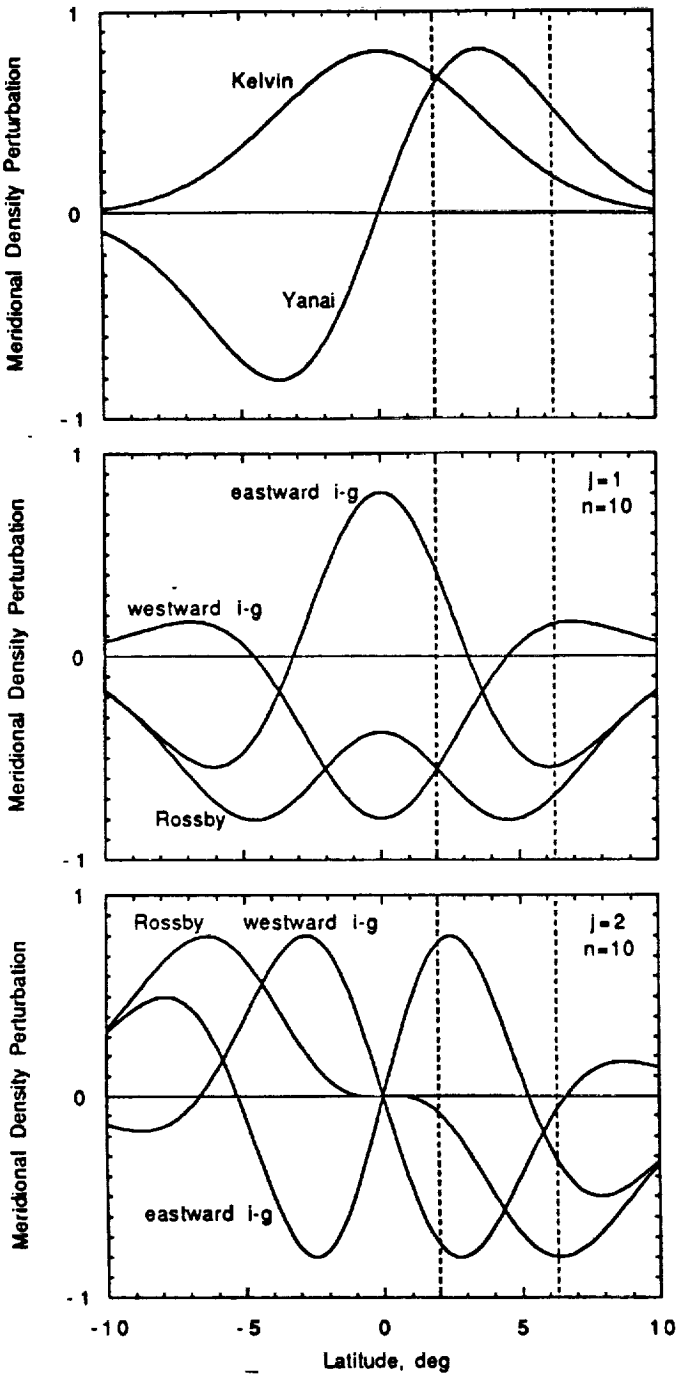

FIG. 7. Meridional structure of variations in atmospheric density caused by equatorial waves. For these calculations, we used a meridional length scale L_y = 1600 km, or about 3.6° lat, consistent with the observations. (Top) Kelvin and Yanai waves; the results are independent of n. (Middle) Inertia–gravity (i–g) and Rossby waves for $j = 1$, $n = 10$. (Bottom) Inertia–gravity and Rossby waves for $j = 2$, $n = 10$. Meridional structure grows in complexity as j increases. Dashed vertical lines show the latitudes of immersion and emersion. Curves have been scaled for convenient comparisons.

the westward inertia–gravity wave ($j = 1$, $n = 10$) whose spatial structure is given by Eqs. (22) and (27)–(32); the meridional structure of this mode appears in Fig. 7. Next, we computed the phase modulation that would result from this atmospheric structure in a hypothetical radio occultation experiment. In this step, we evaluated Eqs. (2) and (6) for the geometry of the occultation of Voyager 2, where the path of integration nearly coincides with the meridional direction at the equator (cf. Fig. 1). Finally, we tabulated the results (phase residuals ψ as a function of the atmospheric pressure at periapsis) for each wave mode considered.

We adopt an important approximation in evaluating the path integral in Eq. (2). For periapsis pressures less than 10 mbars, the refractive bending of the ray path was less than 10^{-3} rad and the corresponding deflection of the ray path within the atmosphere of Uranus was less than 1 km. As this deflection was considerably smaller than both the vertical wavelength of the observed atmospheric wave (~10 km) and the pressure scale height (~35 km), we modeled the ray path as a straight line in these calculations. This simplified the numerical algorithms and reduced computation time significantly.

There is a subtlety in evaluating Eq. (2) that deserves mention. In the preceding section on the theory for atmospheric waves, the integrand in Eq. (2)—ν', or equivalently ρ'—was expressed in log-pressure coordinates, but Cartesian coordinates are most suitable for specifying the path of integration. The relationship between these coordinate systems is complicated by the fact that atmospheric waves modulate the geometric height (i.e., ϕ') of surfaces of constant pressure. However, this modulation leads only to a second-order correction to ψ, which can be ignored at the level of approximation used in deriving the wave theory. Hence, we used the relation between pressure and geometric height in the unperturbed atmosphere for the coordinate transformation. The resulting calculations of ψ are valid to first order in the wave perturbations.

Our model calculations included examples of Kelvin, Yanai, inertia–gravity, and Rossby waves. For the latter two wave modes, we included cases where $1 \le j \le 3$ and $5 \le n \le 30$. In all calculations we used values of general parameters, such as β and g, appropriate to Uranus (see Table I). For wave-specific parameters, such as the separation constant gh, we used values derived from the observations (see subsequent sections). Accordingly, the wave modes used in the model calculations had a vertical wavelength of about 10 km and a characteristic meridional scale of L_y = 1600 km, or about 3.6° of latitude on Uranus (cf. Fig. 7).

In evaluating Eq. (2), we found that considerable cancellation occurs during path integration through this type of periodic spatial structure, yielding a result that is heav-

4525 DG/L

TABLE II
Constraints on the Equatorial Wave in the Stratosphere of Uranus

Parameter	Value or constraint
Separation constant, gh	450 ± 100 m^2 sec^{-2}
Characteristic zonal phase speed, $\sqrt{gh}$	21 ± 2 m sec^{-1}
Equivalent depth, h	53 ± 12 m
Vertical wavenumber,[a] μ	20 ± 2
Wave amplitude[a]	
T_i' (immersion)	1.1 ± 0.4 K
T_e' (emersion)	0.5 ± 0.2 K
Density ratio, $\lvert\rho_i'/\rho_e'\rvert$	2.1 ± 0.3
Characteristic meridional length scale, L_y	1600 ± 260 km ($3.6 \pm 0.6°$ lat)
Zonal structure	Oscillations of data nearly "in phase" at immersion and emersion
Zonal phase speed	$c > 0$ m sec^{-1} or $c < -60$ m sec^{-1}

[a] At 1-mbar pressure level.

ily weighted toward the properties of the wave near periapsis. This cancellation leads to an equivalent length for the path of integration of about 500 km, or about 1.1° of latitude, for all wave modes considered here. The measurements represent a meridional average of ρ' over the length of this equivalent path, which is small compared to the meridional scale of the wave. Hence, to a good approximation, ψ is directly proportional to the value of ρ' at periapsis. These results greatly simplify the interpretation of the data.

RESULTS

In this section we present the fully reduced phase data from Canberra. When compared with predictions of the theory for atmospheric waves, these data reveal the presence of a vertically propagating wave in the equatorial stratosphere of Uranus. We exploit characteristics of the data at both immersion and emersion to obtain constraints on the vertical, meridional, and zonal structure of the wave; we also apply results derived from observations with the IRIS instrument on Voyager 2 to constrain the zonal phase speed. We then search for individual equatorial wave modes that are consistent with the observations. After applying these constraints to eliminate a large number of wave modes from further consideration, we identify two modes, both inertia–gravity waves, as equally likely solutions. These modes, though not unique, have the virtue of explaining the observations while retaining the simplest possible spatial structure. Although superpositions of wave modes could also account for the observations, the available data are insufficient to support a meaningful investigation of this possibility. The results are summarized in Tables II and III. We show in Appendix B that the reduced amplitude data verify the accuracy of the phase data and corroborate the results derived in this section.

Observations at low pressures. Figure 8 shows phase residuals measured at low pressures where the separate contributions due to the neutral atmosphere and ionosphere of Uranus as well as measurement noise can be readily identified. The three profiles in each panel correspond to data at s-band (ψ_s), at x-band (ψ_x), and with plasma effects removed (ψ_n). After processing data over time intervals widely separated from the occultation, we concluded that the observations at periapsis pressures less than 0.003 mbar during emersion are representative of the measurement noise level.

At immersion, ψ_s and ψ_x exhibit highly correlated ionospheric effects at pressures between 0.001 and 0.4 mbar, while the signature of the neutral atmosphere predominates in ψ_x and ψ_n at pressures exceeding 0.4 mbar. Our attempt to remove plasma effects worked reasonably well in that ψ_n is generally reduced in magnitude relative to either ψ_s or ψ_x at pressures less than 0.4 mbar. There is one notable exception, however, an oscillatory feature in ψ_n centered near 0.01 mbar. This feature is probably attributable to the limitations of our procedure for removing plasma effects [see discussion following Eq. (9)]. Our interpretation of results at immersion will be based on ψ_n.

In contrast to immersion, the measurements at emersion show no evidence for plasma effects over the spatial scales considered here. We therefore decided to forgo the plasma correction for these data. Instead, our interpretation of the results at emersion will be based on ψ_x which has a smaller noise level than ψ_n. Substantial effects of the neutral atmosphere are apparent in ψ_x for periapsis pressures exceeding about 0.4 mbar, similar to the observations at immersion. In addition, close inspection of ψ_x reveals a weak oscillatory pattern at pressures between 0.02 and 0.06 mbar. Although the magnitude of these effects is close to the noise level of the spacecraft oscillator, this feature also could be attributable to the neutral atmosphere.

Vertical structure. Figure 9 displays the phase residuals from immersion and emersion over the full pressure range of interest. At each location, there is a distinct onset of effects from the neutral atmosphere at a pressure of about 0.4 mbar and the phase residuals oscillate with a vertical scale of about 10 km at larger pressures. The magnitude of the oscillations generally increases with pressure, but the residuals at immersion are about twice as large as those at emersion for all pressures exceeding 0.4 mbar.

We interpreted the measurements in Fig. 9 using of the theory for atmospheric waves. Equation (45) expresses the vertical variations of ρ' expected for an equatorial wave in the form of an oscillatory exponential function modulated by factors that vary relatively slowly with z.

TABLE III
Inferred Properties of the Equatorial Wave in the Stratosphere of Uranus

Parameter	Solution 1[a]	Solution 2[a]	Units
Wave type	Inertia–gravity	Inertia–gravity	
Meridional index, j	1	2	
Zonal wavenumber, n	6	14	
Zonal phase speed, c	-95 ± 15 (westward)	$+59 \pm 9$ (eastward)	m sec^{-1}
Frequency, σ	-2.2 ± 0.4	$+3.2 \pm 0.5$	10^{-5} rad sec^{-1}
Period, $2\pi/\lvert\sigma\rvert$	79 ± 13	55 ± 9	hr
Pressure at breaking level, p_b	$200 + 200/-100$	$200 + 200/-100$	μbar
Eddy diffusion coefficient at $p = p_b$	0.6 ± 0.3	1.0 ± 0.5	10^4 cm^2 sec^{-1}
Wave forcing of mean flow, $\langle \partial\bar{u}/\partial t \rangle$, at $p = p_b$	$-13 + 7/-13$	$+20 + 20/-10$	cm sec^{-1} per planet rotation

[a] The two solutions are equally good alternatives for explaining the observations.

These factors determine the "envelope" of vertical variations in wave amplitude. Moreover, Eq. (45) contains two free parameters: (1) the separation constant gh, which sets the vertical scale of the wave oscillations, and (2) a complex constant G_0, which determines the amplitude and phase of the wave at a reference level [cf. Eqs. (27) and (28)]. Aside from a multiplicative constant, the theoretical envelope of the wave is completely determined by the ambient background structure of the atmosphere through $\bar{\rho}$ and $\bar{T}$ [cf. Eq. (19)].

We computed the theoretical envelope appropriate to the observed background structure in the atmosphere of Uranus; the results are superimposed on the measured phase residuals in Fig. 9. (Recall that our model calculations demonstrated that ψ is directly proportional to ρ' at periapsis.) The scaling factor for the envelope was adjusted independently at immersion and emersion so that 75% of the data samples at pressures between 0.4 and 10 mbars fall within the bounds of the envelope. The close agreement in Fig. 9 between the theory and observations provides unambiguous, compelling evidence for the presence of an atmospheric wave in the stratosphere of Uranus. This comparison reveals that the observed vertical variations in the magnitude of the residuals represent the natural response of a vertically propagating wave to the background structure of the atmosphere. At pressures exceeding about 0.4 mbar, the wave appears to propagate vertically without appreciable attenuation.

We solved for gh through comparisons between the measurements in Fig. 9 and the theoretical predictions for the full vertical structure of the wave, Eq. (45). We took as the solution for gh the value that yields the same number of phase oscillations as were observed in the pressure interval between 0.4 and 10 mbars. The result is the same at both immersion and emersion:

$$gh = 450 \pm 100 \text{ m}^2 \text{ sec}^{-2}. \quad (46)$$

After scaling by g, we obtain the equivalent depth:

$$h = 53 \pm 12 \text{ m}. \quad (47)$$

The uncertainties assigned to these results correspond to the change in gh that would yield one more or one less phase oscillation than observed within the relevant pressure interval. Figure 10 shows the vertical structure computed from Eq. (45) for this value of gh. Again, the predictions of the theory bear a striking similarity to the measurements.

The results displayed in Figs. 9 and 10 provide a powerful means for identifying the signature of a stratospheric wave. However, the analysis of vertical structure at a single location does not by itself allow a more specific identification of the wave mode, since the vertical structure predicted by Eq. (45) is not only common to all the equatorial wave modes (Kelvin, Yanai, inertia–gravity, and Rossby) but also independent of the meridional index j and the zonal wavenumber n. To obtain a more complete characterization of the wave, we must rely on comparisons between the measurements at immersion and emersion.

Wave amplitude. We solved for the amplitude of the atmospheric wave at both immersion and emersion as well as the ratio of amplitudes at the two locations using the envelopes fitted to the measurements in Fig. 9. In this step we relied on results concerning the proportionality between the observed phase residuals and the properties of the underlying atmospheric wave that were derived through model calculations. At the 1-mbar pressure level, where $\bar{T} = 77$ K, the amplitude of the wave expressed as a temperature perturbation was $T_i'(1 \text{ mbar}) = 1.1 \pm 0.4$ K at immersion and $T_e'(1 \text{ mbar}) = 0.5 \pm 0.2$ K at emersion; the subscripts "i" and "e" refer to immersion and emersion, respectively. The ratio of the density perturbations at immersion and emersion on a surface of constant $\hat{z}$ had an absolute value:

$$|\rho_i'/\rho_e'| = 2.1 \pm 0.3. \quad (48)$$

(4525)

Dg/am/KK

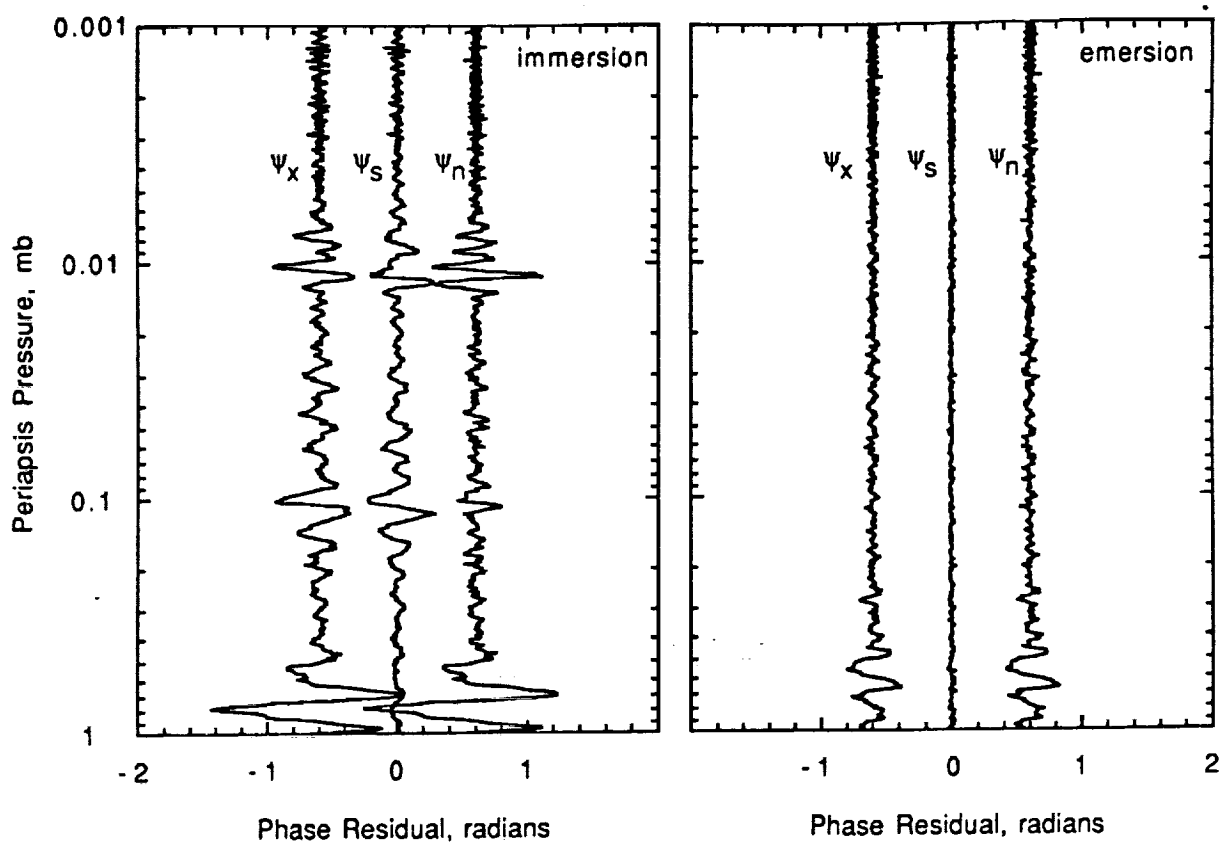

FIG. 8. Phase residuals at low pressures. Data have been reduced with the 20-km filter of Fig. 5. The three profiles in each panel show measurements at s-band (ψ_s), x-band (ψ_x), and with plasma effects removed (ψ_n). We scaled ψ_s by a factor of 3/11 so that plasma effects will appear with the same magnitude in ψ_s and ψ_x. With this scaling, the effect of the neutral atmosphere will be larger in both ψ_x and ψ_n than ψ_s by a factor of 121/9. We have also shifted ψ_n and ψ_s so that the profiles can be easily distinguished. *Immersion*: The ionosphere of Uranus produced highly correlated fluctuations in ψ_s and ψ_x at pressures less than 0.4 mbar, while the neutral atmosphere imposed a distinctive signature in ψ_s and ψ_n for pressures exceeding 0.4 mbar. The prominent, oscillatory feature in ψ_n centered near 0.01 mbar is most likely an artifact of the procedure for removing plasma effects from the data. *Emersion*: Unlike observations at immersion, these data show no evidence for plasma effects. Note that ψ_s and ψ_n exhibit weak oscillations for pressures between 0.02 and 0.06 mbar. Due to the absence of comparable effects in ψ_x, this feature is attributable to either the neutral atmosphere or, possibly, phase noise from the spacecraft oscillator. More prominent effects of the neutral atmosphere appear in ψ_x and ψ_n for pressures exceeding 0.4 mbar.

To explain the uncertainties assigned to these results, we must digress briefly to illustrate the sensitivity of the phase residuals to variations in d, the interval for filtering the data. Figure 11 shows ψ_n at immersion for d = 15, 20, and 25 km. The three curves are highly correlated; the principal difference among them is a modest reduction in the magnitude of the phase residuals with decreasing d (cf. Fig. 5). This introduces what we believe is the predominant source of uncertainty in measurements of wave amplitude. We used the variations among the profiles in Fig. 11 to estimate the size of the uncertainties in T_i' and T_e'. However, the measurements from both immersion and emersion exhibit a similar sensitivity to variations in d. Hence, the measurement of $|\rho_i'/\rho_e'|$ is insensitive to variations in d within the range considered here. The uncertainty in this quantity arises from two other sources. First, measurement noise leads to an uncertainty of about 10%. Second, the measured phase oscillations (Fig. 9) are somewhat less regular than the predictions of the theory (Fig. 10) leading to an additional uncertainty which we estimate to be about 10%. Taking these two sources of uncertainty to be statistically independent, we arrive at the result given above.

There are two reasons why the wave perturbations are not readily apparent in the temperature profiles of Fig. 2. First, neither the radio occultation profile (curve a) nor the UVS profile (curve b) has a vertical resolution that is well suited to direct investigation of a wave with a vertical scale of about 10 km. Given the behavior of vertically propagating atmospheric waves, the temperature perturbations should be most apparent at pressures less than about 1 mbar where the background density is small and

(4525)

Dg/am/KL

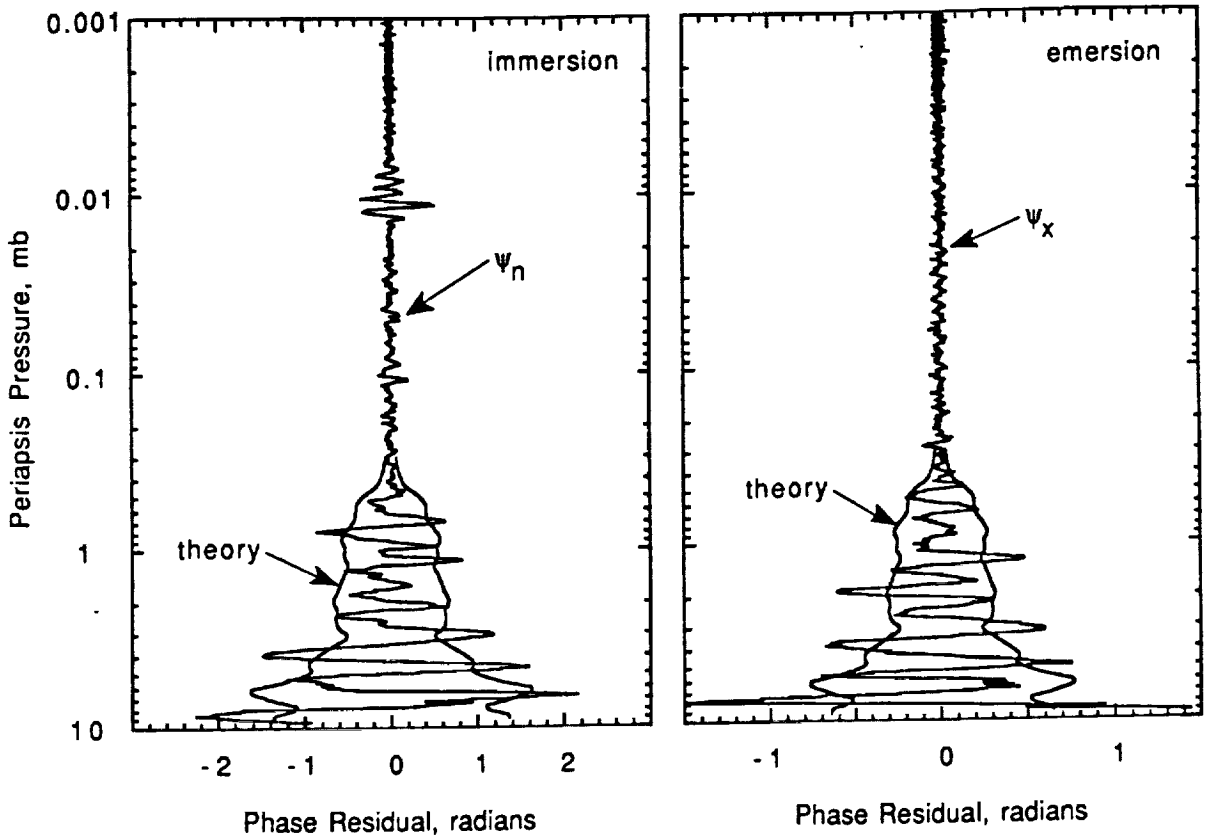

FIG. 9. Phase residuals from immersion (ψ_n) and emersion (ψ_x) over the full pressure range of interest. The measurements exhibit a distinct onset of effects from the neutral atmosphere at a pressure of about 0.4 mbar. At larger pressures, the phase residuals oscillate with a vertical scale of about 10 km and the magnitude of the oscillations generally increases with pressure. We computed the theoretical envelope appropriate to an equatorial wave propagating through the observed background structure in the atmosphere of Uranus; the results are superimposed on the measurements. The theory agrees closely with the observations, revealing the presence of an atmospheric wave. The observed vertical variations in the magnitude of the residuals represent the natural response of a vertically propagating wave to the background structure of the atmosphere. Phase residuals at emersion closely resemble those at immersion but are smaller in magnitude by about a factor of 2; note difference between scales in panels.

the static stability (i.e., N) is large [cf. Eqs. (16), (22), and (45)]. But the radio occultation profile has been smoothed to a resolution of about 5 km at these pressures [see Table 1 of Lindal *et al.* (1987)] while the resolution of the UVS profile is about 10 km at best (Bishop *et al.* 1990). Second, the amplitude of the temperature perturbations is so small—about 1 K at 1 mbar but only about 0.2 K at 10 mbars—that it is difficult to see them in a display like Fig. 2.

Meridional structure. The difference in the magnitude of the phase residuals at immersion (2.0°N) and emersion (6.3°N) suggests a wave confined in latitude near the equator. We can exploit this constraint on meridional structure to identify a few equatorial wave modes that are consistent with the observations.

We previously derived theoretical expressions for the meridional variations in ρ' that accompany equatorial waves; specifically, Eqs. (40), (42), and (44) give the meridional structure for Kelvin, Yanai, and inertia–gravity and Rossby waves, respectively (cf. Fig. 7). We evaluated these functions at the latitudes of immersion and emersion for a variety of cases and tabulated the results in the form of ρ_i'/ρ_e', the ratio of the density perturbations on a surface of constant $\hat{z}$. The predictions of the theory expressed in the form of this "density ratio" can be tested against the data through comparison to the measured ratio of wave amplitudes. For all calculations, we used the solution for gh obtained above. This parameter is essential to a meaningful investigation of meridional structure [cf. Eqs. (29)–(31)] and yields a value for the characteristic meridional length scale:

$$L_y = 1600 \pm 260 \text{ km}. \quad (49)$$

The uncertainties assigned to this result and to subsequent

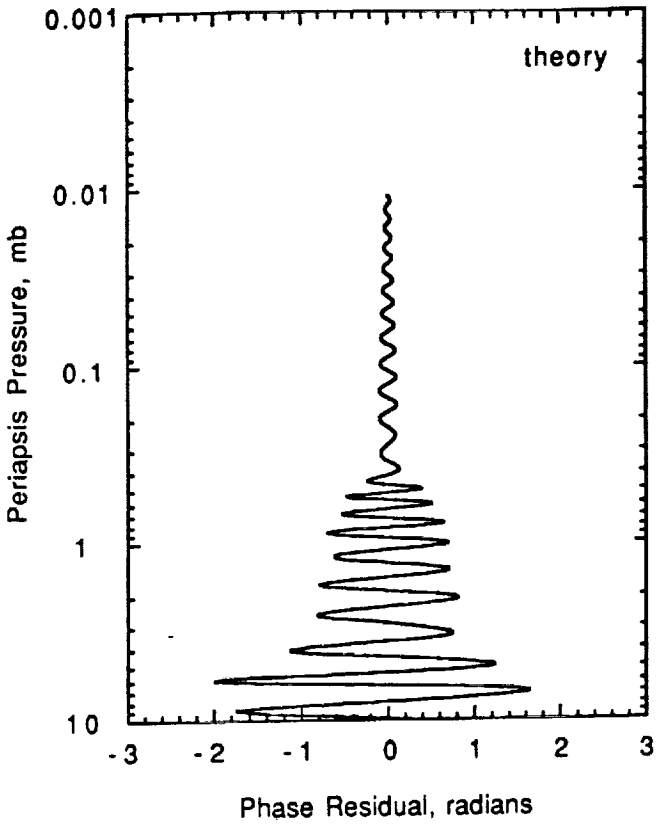

FIG. 10. Theoretical predictions for the vertical structure of an equatorial wave propagating vertically without attenuation through the atmosphere of Uranus. The amplitude of the wave, G_0, has been scaled for comparison with measurements at immersion. Note striking similarity to observations in Fig. 9.

estimates of σ and c are explained at the end of this section.

Figure 12a shows theoretical predictions of ρ_i'/ρ_e' for Kelvin and Yanai waves. For these wave modes, the density ratio is independent of n. The error bars for each curve (and for similar curves presented below) result from the uncertainty in the measurement of gh. As neither prediction is consistent with the measured density ratio, we eliminated Kelvin and Yanai waves as candidates for explaining the observations.

We computed theoretical predictions for the density ratios that characterize inertia–gravity and Rossby waves using Eq. (44) combined with the solutions for ω from Eq. (43). The results corresponding to two values of the meridional index appear in Figs. 12b ($j = 1$) and 12c ($j = 2$). From these calculations, we identified three wave modes that are consistent with the observations: (1) the westward inertia–gravity wave where $j = 1$ and $n = 5 + 3/-3$; (2) the eastward inertia–gravity wave where $j = 2$ and $n = 13 + 10/-5$; and (3) the westward inertia–gravity wave where $j = 2$ and $n = 29 + 26/-9$. In each case, we selected as the solution for n the value that yields the best fit to the observations and assigned errors that reflect the uncertainties in the measurements of $|\rho_i'/\rho_e'|$ and gh. Figures 12b and 12c also show that Rossby waves are inconsistent with the observations for any choice of n when $j = 1$ or 2.

The meridional structure of equatorial inertia–gravity and Rossby waves grows in complexity as j increases (cf. Fig. 7). Hence, we can undoubtedly find wave modes for $j > 2$ that produce the same density ratio as observed. However, the available data are too sparse to support a meaningful investigation of waves with complex spatial structure. For this reason, we decided not to search for additional wave modes that are consistent with the observations. Instead we restrict our attention to the three modes already identified; these have the virtue of retaining the simplest possible spatial structure while still accounting for the principal features of the observations.

Zonal structure. We now derive an additional constraint on n. Close comparison of the two profiles in Fig. 9 reveals a notable similarity in their detailed structure. This appar-

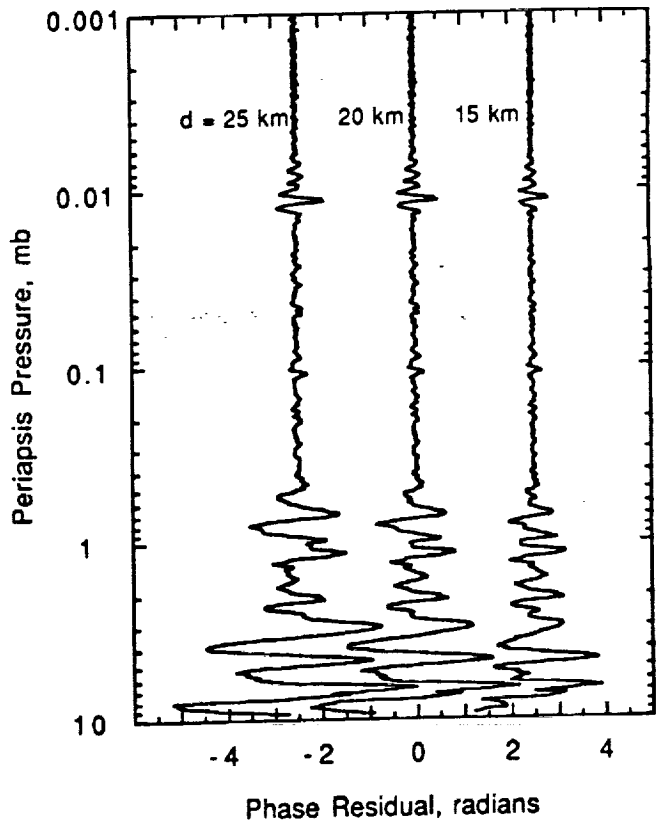

FIG. 11. Phase residuals at immersion (ψ_a) corresponding to three different values of the filtering interval, d. The middle profile ($d = 20$ km) appeared in Fig. 9. The other two profiles have been shifted so that the three profiles can be easily distinguished. As d decreases from 25 to 15 km, the residuals decrease in magnitude but remain highly correlated.

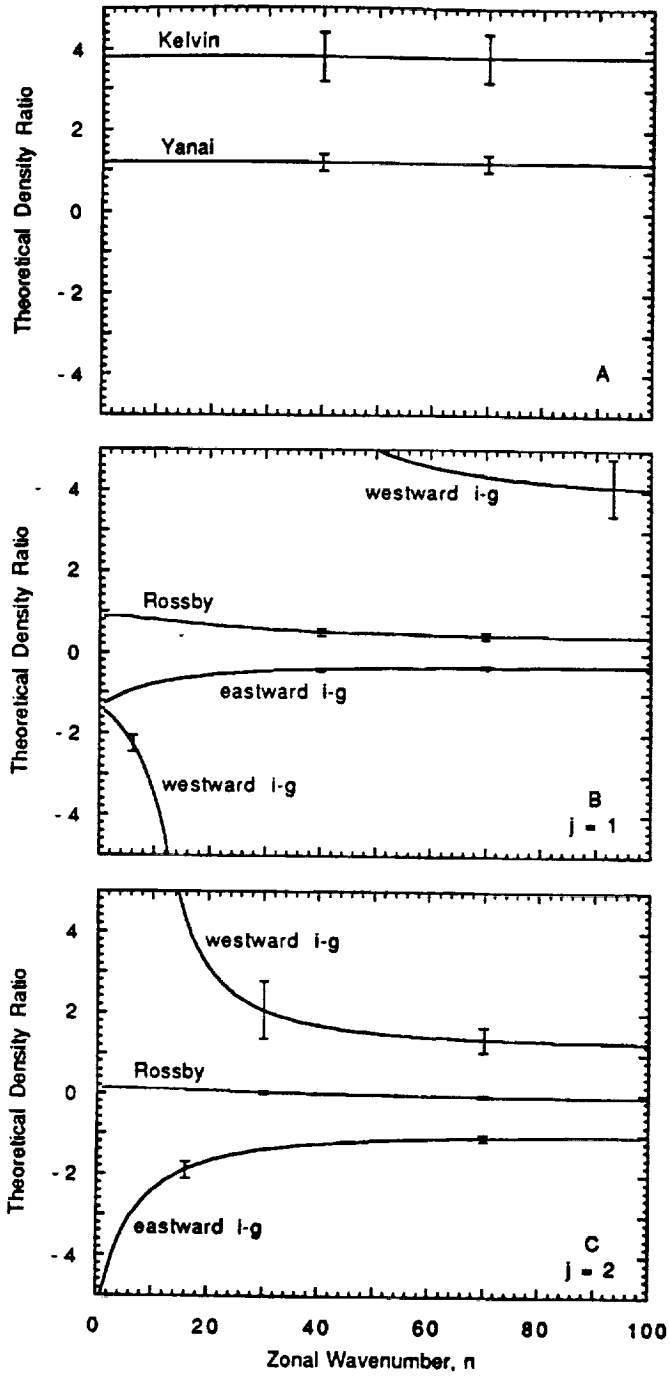

FIG. 12. Theoretical predictions of ρ_i'/ρ_e' for equatorial wave modes as a function of n, the zonal wavenumber. (Top) Kelvin and Yanai waves. (Middle) Inertia–gravity and Rossby waves for $j = 1$. (Bottom) Inertia–gravity and Rossby waves for $j = 2$.

ent correlation between the observations at immersion and emersion, separated by about 145° in longitude, suggests a wave of planetary scale.

We quantified this comparison by computing auto- and cross correlations of the phase residuals for periapsis pressures between 0.4 and 10 mbars. Figure 13 shows the results as a function of the vertical offset, or lag, applied to the data. The cross-correlation function bears a strong resemblance to the autocorrelations; a significant maximum near zero lag indicates that the oscillations of the residuals are nearly "in phase" at immersion and emersion. All three correlation functions also exhibit secondary peaks for lags of about ±10 km which reflect the fundamental periodicity of the phase residuals in the vertical direction.

The location of the maximum in the cross correlation provides a useful constraint on n. We exploited this measurement to reduce the range of permissible values for n associated with each of the three wave modes identified above. For example, Fig. 13 shows the predicted location

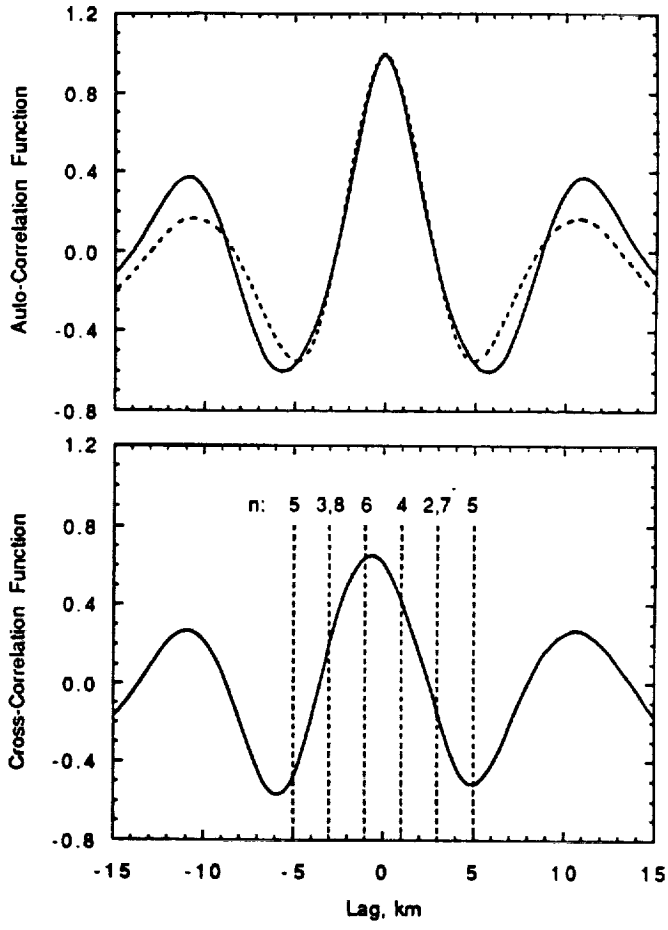

FIG. 13. (Top) Autocorrelations of phase residuals measured at immersion (solid line) and emersion (dashed line). Secondary maxima appear at lags of about ±10 km, corresponding to the fundamental vertical period of the phase oscillations. (Bottom) Cross correlation between phase residuals at immersion and emersion. The result is similar in appearance to the autocorrelations. A significant maximum near zero lag indicates that the residuals oscillate nearly "in phase" at the two locations. Dashed vertical lines show predicted position of the correlation peak as a function of the zonal wavenumber, n, for the westward ($j = 1$) inertia–gravity wave.

of the peak in the cross correlation for each possible value of n listed above for the westward ($j = 1$) inertia–gravity wave. As $\rho_i'/\rho_e' \approx -2$ for this mode, we must select a value for n that yields a net phase shift of about π rad between the longitudes of immersion and emersion in order to be consistent with the observations. Applying these considerations to each of the three wave modes, we obtain the refined solutions: (1) the westward inertia–gravity wave where $j = 1$ and $n = 6$; (2) the eastward inertia–gravity wave where $j = 2$ and $n = 14$; and (3) the westward inertia–gravity wave where $j = 2$ and $n = 32$. In these calculations we accounted for the time development of the atmospheric wave that occurs in the 84-min interval separating immersion and emersion. As this time span is smaller than the period of the waves by a factor of about 40, this amounts to a small correction. From Eqs. (36) and (43), the frequencies, σ, of these three modes are -2.2 ± 0.4, $+3.2 \pm 0.5$, and -3.8 ± 0.6, respectively, in units of 10^{-5} rad sec^{-1}.

Zonal phase speed. To be consistent with the observations, the equatorial wave must satisfy one additional constraint that arises in connection with the background circulation of the atmosphere. Measurements by the IRIS instrument on Voyager 2 suggest that the zonal wind near the equator of Uranus has a vertical shear ($\partial\bar{u}/\partial\hat{z}$) of about $+50$ m sec^{-1} per scale height in the pressure interval between 60 and 200 mbars, near the tropopause (Flasar *et al.* 1987); the integrated wind shear between these two pressure levels is about $+60$ m sec^{-1}. If the wave observed at pressures less than 10 mbars originates in the troposphere, as seems likely, it is reasonable to assume that it traversed this region of wind shear without encountering a critical level. (At a critical level, the intrinsic frequency of the wave measured relative to the local mean wind is Doppler-shifted to zero. When the local gradient Richardson number greatly exceeds unity, as it does near the tropopause of Uranus, virtually no wave energy would be expected to pass through this level [Turner 1973].) These considerations lead to a constraint on c, the zonal phase speed of the wave measured relative to the local mean flow. In the pressure interval where we make our observations ($p < 10$ mbars), either the zonal phase speed is eastward ($c > 0$), or it must be westward with a magnitude that exceeds about 60 m sec^{-1} ($c < -60$ m sec^{-1}). We tested the behavior of the equatorial wave modes against this constraint using results from the wave theory. Combining Eqs. (36) and (37),

$$c = \sqrt{gh}\frac{\omega}{k}. \tag{50}$$

This expression can be evaluated using the measured value of gh along with Eqs. (39), (41), and (43), which give expressions for ω/k appropriate to each wave mode. The three inertia–gravity wave modes identified above have zonal phase speeds of -95 ± 15, $+59 \pm 9$, and -30 ± 5 m sec^{-1}, respectively. Hence, the first two can pass through the region of wind shear near the tropopause without encountering a critical level, but the third cannot, so we eliminate this mode from further consideration.

We previously showed that Rossby waves are inconsistent with the observations for $j = 1$ or 2; we now generalize this result to all values of j. The zonal phase speed of the Rossby wave is exclusively westward ($c < 0$) with a magnitude that satisfies the condition

$$|c| < \sqrt{gh}/(2j + 1). \tag{51}$$

For the measured value of gh, $|c| \ll 60$ m sec^{-1} for all possible values of j. This leads to a logical inconsistency: Rossby waves whose characteristics match the observations at pressures less than 10 mbars could not have reached this region of the stratosphere without first encountering a critical level near the tropopause. For this reason, Rossby waves are unacceptable for explaining the observations for any choice of j.

The neglect of wind shear. In deriving the theory for atmospheric waves, we modeled the background circulation of the atmosphere near the equator as a uniform zonal flow. The neglect of wind shear reduced the complexity of the theory to a manageable level, thus permitting straightforward comparisons between the observations and specific predictions of the theory. Nevertheless, wind shear—both vertical and horizontal—can have a significant effect on the type of waves considered here (Lindzen 1971, 1972, Holton 1979); its neglect is potentially the most serious limitation of the wave theory. We now attempt to assess the validity of this approximation in light of the results derived in this section.

This task is inhibited by the scarcity of data. The vertical shear is unknown at pressures less than 10 mbars where we compared predictions of the simple wave theory to the observed phase residuals. [It can be inferred from Voyager 2 IRIS observations only at pressures exceeding about 60 mbars (Flasar *et al.* 1987).] However, vertical variations in the mean zonal wind $\bar{u}$ would be expected to cause substantial variations in both the amplitude and vertical wavelength (or equivalent depth) of a vertically propagating wave, provided that the vertically integrated shear is comparable to $|c - \bar{u}|$. As effects of this sort are not apparent in the comparisons between theory and observations in Figs. 9 and 10, the neglect of vertical shear in $\bar{u}$ would appear to be justified.

Turning our attention to horizontal variations in $\bar{u}$, we would argue that these can be neglected if two conditions are satisfied: (1) $|\partial^2\bar{u}/\partial y^2| \ll \beta$; and (2) the variation in $\bar{u}$ over a horizontal distance corresponding to the meridional scale of the wave is much smaller than the zonal phase

speed c. The first condition can be understood as follows: when $\bar{u}$ varies as y^2 near the equator, the addition of a term $v' = \partial\bar{u}/\partial y$ will reduce the effective value of β in Eq. (14) by an amount $\partial^2\bar{u}/\partial y^2$. The second condition arises from consideration of critical levels. Using a simple analytic expression for $\bar{u}$ [see Eq. (2) and Fig. 8 of Allison *et al.* (1991)], we find that $|\partial^2\bar{u}/\partial y^2| \approx \beta/3$ at the equator. Similarly, the change in $\bar{u}$ over a distance $(2j + 1)^{1/2} L_y$—the meridional scale of an inertia–gravity wave (Allison 1990)—is about 10–20 m sec^{-1} for the wave modes in Table III. These parameter values are at least three times smaller than β and c, respectively, which tends to support the neglect of horizontal shear in the wave theory.

However, it should be noted that the available data on $\bar{u}$ are sparse, particularly near the equator. Consequently, the estimates of the latitudinal curvature of the mean zonal wind and our conclusions about the validity of neglecting horizontal shear are both subject to sizable uncertainties. The preceding qualitative discussion of the effective value of β in the presence of horizontal shear suggests a reasonable approach to handling this difficulty. By attributing an uncertainty of 33% to the value for β given in Table I, we can quantify, at least approximately, the possible effect of horizontal shear on our results. Our error analysis, which yielded the uncertainties given in Tables II and III, reflects not only the measurement uncertainty associated with parameters like $\sqrt{gh}$ but also this assumed uncertainty in the effective value of β. This had a significant effect on the stated accuracy of the results for L_y, σ, and c.

A final note is in order concerning the results given in Table III. We computed the uncertainties for the parameter values in each column as though j and n were known a priori. This gives some indication of the sensitivity of the data for inferring various quantities of interest. However, either wave mode in Table III is an equally good alternative for explaining the observations. Hence, the difference between the parameter values for solutions 1 and 2 may give a more realistic indication of the reliability of the various results.

DISCUSSION

We now apply the results of the previous section to model the behavior of the wave at pressures less than 0.4 mbar, where the signal-to-noise ratio of the data is insufficient for direct observations. Our goal is to assess the effect of the wave on the eddy mixing and circulation of the equatorial middle atmosphere.

Dissipation. The amplitude, T', of a wave propagating vertically without attenuation increases with height approximately as $e^{z/2}$ [cf. Eq. (27)]. However, this behavior cannot persist above the so-called "breaking level" defined by the condition

$$\left|\frac{dT'}{d\hat{z}}\right| = \frac{d\bar{T}}{d\hat{z}} + \frac{R\bar{T}}{c_p}. \tag{52}$$

At this level (denoted by its pressure, p_b), the combination of wave and mean temperature fields yields an adiabatic lapse rate; continued growth in wave amplitude during propagation above this level would produce a convective instability. Hence, the wave must begin to dissipate at the breaking level, leading to mechanical mixing, heating, and acceleration of the atmosphere at pressures less than p_b. We estimated the breaking level for the wave observed in the stratosphere of Uranus using Eq. (52) and measured values for the relevant parameters (cf. Fig. 2 and Tables I and II). At 2.0°N, $p_b \approx 200 + 200/-100$ μbars, where the errors reflect the uncertainty in the measurement of T'.

In modeling the behavior of the wave at pressures less than p_b, we adopt a procedure applied previously in closely related studies of atmospheric waves by French and Gierasch (1974), Lindzen (1981), and Allison (1990). In this formulation, it is assumed that wave breaking causes eddy mixing that acts to dissipate the wave in a manner akin to molecular viscosity. To avoid a convective instability, the amount of eddy dissipation generated by the wave must be sufficient, when combined with the effect of molecular viscosity, to cancel the exponential growth of wave amplitude with height. We model the dissipation by introducing a nonzero value for X' in Eq. (14), which becomes

$$\left(\frac{\partial}{\partial t} + \bar{u}\frac{\partial}{\partial x}\right)u' - \beta y v' + \frac{\partial\phi'}{\partial x} = -X' \equiv \frac{\nu_{\text{total}}}{H^2}\frac{\partial^2 u'}{\partial\hat{z}^2}, \tag{53}$$

where

$$\nu_{\text{total}} \equiv \nu_{\text{eddy}} + \nu_{\text{mol}}.$$

Here, ν_{eddy} is the eddy diffusion coefficient that results from wave breaking and ν_{mol} is the molecular viscosity of the background atmosphere. At the same time, we insert analogous terms involving v' and $\partial\phi'/\partial\hat{z}$ on the right-hand sides of Eqs. (15) and (18), respectively. The combined effect of these terms is mathematically equivalent to perturbing the frequency of the wave through addition of a small imaginary component:

$$\sigma \rightarrow \sigma + i\frac{\mu^2\nu_{\text{total}}}{H^2}. \tag{54}$$

The dispersion relation, Eq. (31), leads in turn to the requirement that the vertical wavenumber μ (or equivalently, gh) must also have a small imaginary component:

$$\mu \rightarrow \mu + i\mu_1. \tag{55}$$

We must set $\mu_1 \approx \pm 1/2$ in order to cancel the exponential growth of the wave [cf. Eq. (27)]; the choice of signs arises in the expression for $G(\hat{z})$ and ensures that damping occurs for a wave whose vertical group velocity is positive. Substitution of these generalized expressions for σ and μ into (31) yields

$$\nu_{\text{total}} \approx \frac{H^2|\sigma|}{2\mu^3} \cdot R(\sigma, j, n) \tag{56}$$

to first order in the perturbations to σ and μ. The function R can be expressed as

$$R \equiv \frac{2\omega^2 - (2j+1)}{3\omega^2 - (2j+1) - k^2}. \tag{57}$$

Substitution of parameter values from Tables I–III into Eq. (56) yields estimates for ν_{total} of $(0.7 \pm 0.3) \times 10^4$ cm^2 sec^{-1} for solution 1 and $(1.1 \pm 0.5) \times 10^4$ cm^2 sec^{-1} for solution 2. We reiterate that ν_{total} represents the combination of eddy dissipation and molecular viscosity required at altitudes above the breaking level to offset the exponental growth of wave amplitude with height. Consequently, we expect ν_{total} to be nearly independent of height in the region bounded below by the breaking level and bounded above by the level where ν_{mol} becomes large (see below).

We computed the vertical profile of ν_{mol} appropriate to the thermal structure in the atmosphere of Uranus using experimental data on the viscosities of hydrogen and helium from Touloukian *et al.* (1975). We then obtained ν_{eddy} by taking the difference between ν_{total} and ν_{mol}; the results appear in Fig. 14. The largest value of ν_{eddy} occurs at the breaking level where $\nu_{\text{mol}} \approx 900$ cm^2 sec^{-1}, which is much smaller than ν_{total}. Above the breaking level, ν_{eddy} decreases with height as a result of the increase in ν_{mol} with decreasing atmospheric density. At about the 20-μbar pressure level, ν_{mol} approaches ν_{total} and ν_{eddy} falls rapidly to zero, marking the upper boundary of the region where wave breaking contributes to mechanical mixing of the atmosphere. The wave amplitude diminishes rapidly with height at pressures less than about 20 μbars as a result of the continuing exponential growth in damping due to molecular viscosity.

The UVS instrument on Voyager 2 observed a solar occultation by Uranus, providing complementary data on the equatorial middle atmosphere (Broadfoot *et al.* 1986). Due to the similar viewing geometries of the solar and radio occultations, the two experiments provide near-concurrent observations of the same location on the planet, but over a different range of pressures (e.g., Fig. 2). A

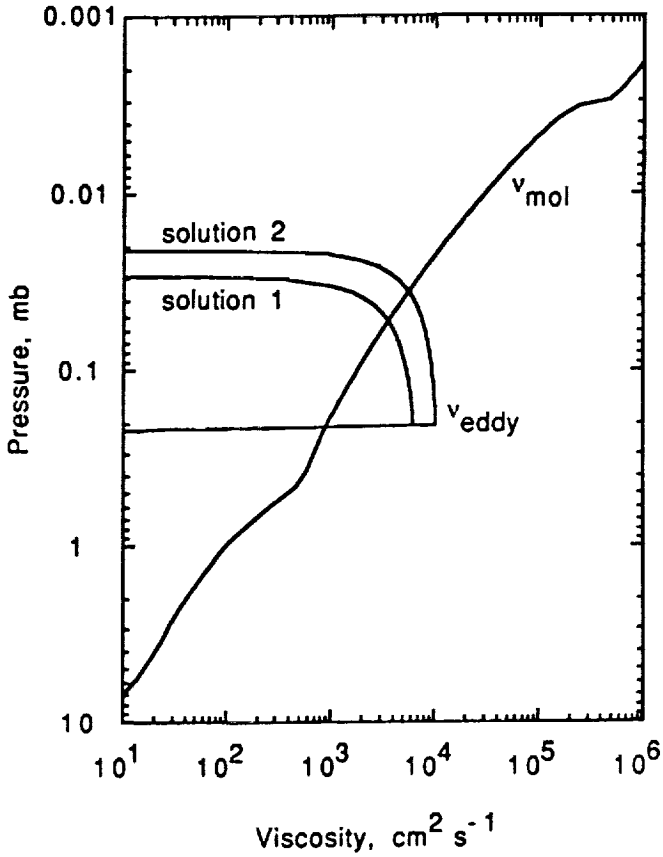

FIG. 14. Results from modeling the dissipation of the observed equatorial wave. We computed ν_{mol}, the molecular viscosity of the background atmosphere, using a standard formula wherein $\nu_{\text{mol}} \approx A\bar{T}^s/\bar{\rho}$. Here A and s are constants, while $\bar{T}$ and $\bar{\rho}$ are the temperature and density of the background atmosphere, respectively. The eddy diffusion coefficient that results from wave breaking, ν_{eddy}, is shown for the two possible characterizations for the equatorial wave given in Table III.

number of authors have interpreted the UVS measurements through use of one-dimensional models that include photochemistry, condensation, eddy mixing, and molecular diffusion (e.g., Herbert *et al.* 1987, Atreya *et al.* 1991, Bishop *et al.* 1990). Comparisons between model predictions and observations imply that $\nu_{\text{eddy}} \approx 10^3$–$10^4$ cm^2 sec^{-1} at a pressure of a few tens of microbars. [See French *et al.* (1983) for discussion of a complementary constraint derived from observations of stellar occultations.] This estmate of ν_{eddy} is in good agreement with the independent result derived here, which implies that wave dissipation is an important source of eddy mixing in the equatorial middle atmosphere of Uranus.

All parameters in the formula for ν_{total} are well determined from the data with the exception of σ. (For inertia–gravity waves, the function R ranges smoothly in value from 0.5 for small n to 1.0 for large n so that to lowest order its dependence on σ, j, and n can be ignored.) In

this regard, it is significant that we were able to eliminate Kelvin, Yanai, and Rossby waves as candidates for explaining the observations while identifying two inertia–gravity wave modes that are consistent with the data. As a consequence of the dispersion relation for equatorial inertia–gravity waves (cf. Fig. 6), this conclusion leads to a lower bound on the magnitude of σ [cf. Eq. (38), (43), or Beer 1978]:

$$|\sigma| \geq 1.71(\beta\sqrt{gh})^{1/2} \equiv \sigma_{\min}. \tag{58}$$

This lower bound on $|\sigma|$ in turn yields a lower bound on ν_{eddy}. For the parameter values in Tables I and II, these minimum values for $|\sigma|$ and ν_{eddy} are numerically equal to the results for solution 1 given in Table III. We note also that any attempt to interpret the radio occultation data in terms of a wave with $|\sigma| \gg \sigma_{\min}$ would imply a value for ν_{eddy} that conflicts with the UVS results. This corroborates our interpretation of the data as the signature of a planetary-scale equatorial wave.

One way to characterize the effect of radiative damping on an equatorial wave is through the product of the radiative time constant, τ_r, and the group velocity of the wave, $\mathbf{c}_g \equiv (c_g^{(x)}, 0, c_g^{(z)})$. The vertical and horizontal components of the resulting vector correspond to the characteristic scales over which damping occurs. For a spatially periodic disturbance with a characteristic scale of $H/3$, the vertical scale of the observed wave, $\tau_r \approx 2 \times 10^9$ sec at the 10-mbar pressure level on Uranus (F. M. Flasar, private communication, 1990; cf. Flasar *et al.* 1987). At lower pressures, we expect τ_r to be comparable to or larger than this value (cf. Conrath *et al.* 1990). We computed $\mathbf{c}_g \cdot \tau_r$ for the two wave modes in Table III using the value for τ_r at 10 mbars and group velocities obtained through differentiation of Eq. (31). The characteristic vertical (horizontal) scale for damping exceeds $10^3 \times H$ ($20 \cdot 2\pi r_0$) for both solutions. Hence, the effect of radiative damping is negligible for the wave of interest here.

Effect of the wave on the zonal circulation. Boyd (1976) considered the behavior of time-harmonic, linear, hydrostatic waves in a spherical atmosphere with a zonal mean wind that varies with latitude and pressure; he showed that in the absence of dissipation, heating, and critical levels, the waves and the mean flow do not interact (see also Andrews and McIntyre 1976). This result is often called the nonacceleration theorem (Andrews *et al.* 1987). Moreover, in the presence of dissipation, the wave forcing of the mean flow can be expressed approximately as [Boyd 1976, Eq. (VI), Andrews and McIntyre 1976, Eq. (7.7)]

$$\langle \partial\bar{u}/\partial t \rangle \approx c^{-1}\langle \overline{X'u'} + \overline{Y'v'} + \overline{Z'\partial\phi'/\partial\hat{z}}/\Gamma \rangle. \tag{59}$$

Here, X', Y', and Z' are the dissipation terms that appear in Eqs. (14), (15), and (18). We have simplified the problem by considering only meridional averages of all quantities of interest (cf. Andrews and McIntyre 1976),

$$\langle\ \rangle \equiv \frac{1}{2(2j+1)^{1/2}L_y}\int_{-\infty}^{+\infty}(\ )dy, \tag{60}$$

where $(2j+1)^{1/2}L_y$ is the characteristic meridional scale of an equatorial inertia–gravity wave with meridional index j (Allison 1990). The form of Eq. (59) is convenient for computing $\langle \partial\bar{u}/\partial t \rangle$ but provides little physical insight. For this reason, we note that Eq. (59) accounts not only for the familiar wave momentum flux, $\overline{u'\hat{w}'}$, but also for the effect of the mean meridional circulation driven by wave forcing; the latter can influence $\langle \partial\bar{u}/\partial t \rangle$ both through a Coriolis torque and through advection [cf. Andrews *et al.* 1987, Eqs. (3.5.1)–(3.5.3) and (8.3.3)]. Finally, we have also ignored two other terms in writing Eq. (59) (cf. Boyd 1976); one is negligible for the case considered here, and the other represents the effect of the *residual* circulation driven by wave forcing (i.e., the perturbation to the mean meridional circulation that accompanies dissipation).

We now apply these results to the problem at hand. At altitudes below the level of wave breaking ($p > p_b$), we expect the conditions of the nonacceleration theorem to be satisfied so that wave forcing of the mean flow is negligible. However, for $p < p_b$, wave dissipation leads to nonzero values for the wave forcing terms on the right-hand side of (59). We computed the approximate value of these terms using the following expressions for X', Y', and Z' [cf. Eq. (53)]:

$$\begin{Bmatrix} \widehat{X'} \\ \widehat{Y'} \\ \widehat{Z'} \end{Bmatrix} \approx \left\langle \frac{\mu^2\nu_{\text{total}}}{H^2} \right\rangle \begin{Bmatrix} \widehat{u'} \\ \widehat{v'} \\ \partial\phi'/\partial\hat{z} \end{Bmatrix}. \tag{61}$$

At $p = p_b$, $\langle \partial\bar{u}/\partial t \rangle \approx -13 + 7/-13$ and $+20 + 20/-10$ in units of cm sec^{-1} per planet rotation for solutions 1 and 2, respectively. These results should be nearly independent of pressure for $p < p_b$ up to the level where ν_{mol} becomes large ($p \approx 20$ μbars); at lower pressures the wave is rapidly attenuated and wave forcing becomes negligible.

We are faced with considerable uncertainty in evaluating the effect of the wave on the circulation of the middle atmosphere for the following reason. The sign of the wave forcing is reversed, though the magnitude is comparable, for the two possible characterizations of the wave given in Table III, but we cannot distinguish between these two solutions on the basis of available data. This is one reason for adopting the approximations in Eq. (59). However, the magnitude of the wave forcing for either solution is

sufficient to cause a substantial change in $\bar{u}$ provided that the wave persists for a period exceeding several tens of planet rotations. This is an interesting possibility since the vertical transfer of momentum by equatorial Kelvin and Rossby–gravity waves is believed to drive the "quasi-biennial oscillation" in the mean zonal wind observed in the lower stratosphere on Earth (Holton and Lindzen 1972, Andrews *et al.* 1987). Terrestrial Kelvin waves may also contribute in a similar manner to the semiannual oscillation of the mean zonal wind observed near the equatorial stratopause and mesopause (Dunkerton 1979, 1982, Andrews *et al.* 1987). A similar phenomenon could be occurring on Uranus.

SUMMARY

Our principal results are given in the abstract and are not repeated here. However, it is worthwhile to discuss briefly the relative reliability of the results in Tables II and III, which depend to different degrees on a variety of assumptions and approximations.

The strong agreement between the predictions of the wave theory and the observed vertical structure of the phase residuals gives convincing evidence for the presence of a wave in the equatorial stratosphere (cf. Figs. 9 and 10). This agreement also tends to confirm the validity of the simple wave theory in this application. Comparisons between theoretical predictions and the observed vertical structure of the wave yield reliable, straightforward estimates for the characteristic zonal phase speed $\sqrt{gh}$, the vertical wavenumber μ, and the wave amplitude T'. The solution for $\sqrt{gh}$ in turn gives a value for the characteristic meridional length scale L_y, while the measures of T' and μ yield an estimate of the pressure p_b at the breaking level. Moreover, the fact that $T' \ll \bar{T}$ justifies our use of a linearized wave theory. We are confident of the accuracy of these results and conclusions.

A more complete characterization of the wave requires some measure of its horizontal structure, which we obtained through comparisons between data at immersion and emersion. This effort yielded two reliable constraints, one through comparison of wave amplitudes at immersion and emersion, and another that exploits the correlation between the vertical structure observed at the two locations. These constraints, while insufficient for determining the full spatial structure and frequency of the wave, provide persuasive evidence for a wave of planetary scale confined in latitude near the equator. In deriving the results in Table III we therefore adopted the plausible assumption that a single equatorial wave mode underlies the observations. There is a corresponding uncertainty in the estimates of the meridional index j, the zonal wavenumber n, the zonal phase speed c, and the wave frequency σ due to their dependence on this hypothesis as well as the scarcity of the data. Finally, the estimates of the eddy diffusion coefficient ν_{eddy} and the wave forcing of the mean flow $\langle \bar{u}/\partial t \rangle$ are the least well-determined results. They are subject to the same uncertainties as j, n, c, and σ; in addition they were derived through extrapolation of wave behavior at low pressures where direct observations are not available.

For these reasons the two solutions identified in Table III are somewhat speculative. Nonetheless, each provides a compact explanation for the principal features of the data.

APPENDIX A: INFLECTIONS IN THE TEMPERATURE PROFILE RETRIEVED FROM RADIO OCCULTATION DATA

The composite profile in Fig. 2 exhibits local maxima in temperature near pressures of 14, 4, and 0.4 mbar, with temperature minima near 9, 2, and 0.1 mbar. This section presents evidence against a wave interpretation for these thermal features.

We attempted to model the observed vertical structure of these large-scale temperature inflections using theoretical predictions for the temperature perturbations caused by a vertically propagating wave [cf. Eqs. (16), (22), and (45)]. There are two free parameters in the theory: (1) the separation constant gh, which sets the vertical scale of the wave oscillations, and (2) a complex constant G_0, which determines the amplitude and phase of the temperature oscillations at a reference level. As a model for the background structure of the atmosphere through which the waves propagate, we used calculations by Appleby (1986) for an atmosphere in radiative–convective equilibrium. We included the effect of wave breaking in the calculations by suppressing the exponential growth of wave amplitude with height above the level where the wave perturbation first leads to a superadiabatic lapse rate. Figure A1 shows representative results from these calculations.

We found that no choice of the free parameters could reconcile the theory with the observations. For example, parameter values chosen to match the data at pressures between 2 and 20 mbars ($\sqrt{gh}$ = 64 m sec^{-1}; panel B) produce vertical oscillations in temperature outside this pressure interval that are far more rapid and pronounced than those observed. Similarly, a choice of parameter values that fits the temperature maximum near 0.4 mbar ($\sqrt{gh}$ = 150 m sec^{-1}; panel C) fails to reproduce the thermal features observed between 2 and 20 mbars. This incompatibility between theory and observation is in sharp contrast to the situation for the "small-scale" wave, where the same theory showed remarkably good agreement with the data (cf. Figs. 9 and 10). From these considerations, we must reject a wave interpretation for these thermal features, at least within the context and constraints of the simple wave theory adopted here.

This conclusion rests, of course, on the basic assumptions and approximations that were adopted in deriving the underlying theory for atmospheric waves. Hence, it is conceivable that a more general wave theory—one that includes, for example, the effects of wind shear and nonlinearity—might be capable of explaining the observed vertical structure of these large-scale thermal features. While we cannot discount this possibility, there is at present no tangible evidence in its favor. However, the development and application of such a theory is beyond the scope of the present work.

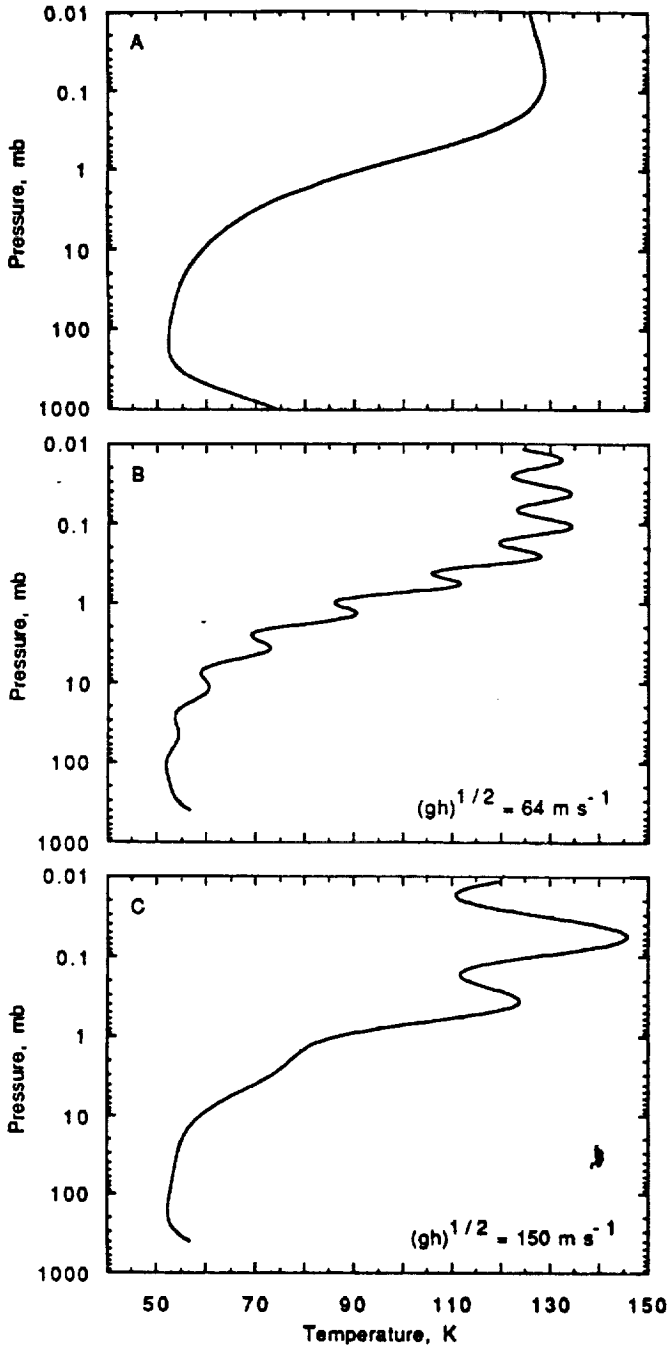

FIG. A1. (A) Radiative–convective equilibrium model for the thermal structure in the atmosphere of Uranus [i.e., curve c in Fig. 2 of Appleby (1986)]. This computed profile compares favorably with the measurements shown in Fig. 2 when the temperature inflections in the latter are smoothed out. (B) Theoretical predictions for the temperature perturbations caused by a wave propagating vertically through the background structure in panel A. Input parameters to the theory were adjusted to fit the observed temperature inflections at pressures between 2 and 20 mbars (cf. Fig. 2), but the theory deviates significantly from the measurements at other pressures. (C) Theoretical predictions as in panel B using different values for input parameters. In this case, the theory fits the measurements near 0.4 mbar but no longer reproduces the thermal features observed between 2 and 20 mbars. For no choice of input parameters did the quality of the fit between theory and observation approach that obtained in Figs. 9 and 10.

APPENDIX B: AMPLITUDE RESIDUALS

In this section we generalize the formulas for the propagation of radio waves in the occultation geometry to include the effect of the background structure of the atmosphere. Although these modifications are important for interpreting some aspects of the amplitude data, they do not change our qualitative conclusions based on Eqs. (5)–(8). We then present the fully reduced amplitude data from Parkes and compare it with the phase data. Overall, the amplitude measurements corroborate the results and interpretation derived independently from phase measurements.

Our model for the phase shift imposed by the occulting atmosphere, Eq. (3), includes the effect of wave-like spatial variations but neglects the contribution from the ambient background structure of the atmosphere. This was done in the interest of simplicity. When the influence of the background structure is included in the derivation, the resulting expressions for a and ψ differ in two important respects from Eqs. (5) and (6) (Haugstad 1978, Hubbard *et al.* 1978, Hinson 1986). First, rays passing through the phase screen at different altitudes experience varying amounts of refraction as a result of the vertical gradient of refractive index associated with the background structure. This differential refrac-

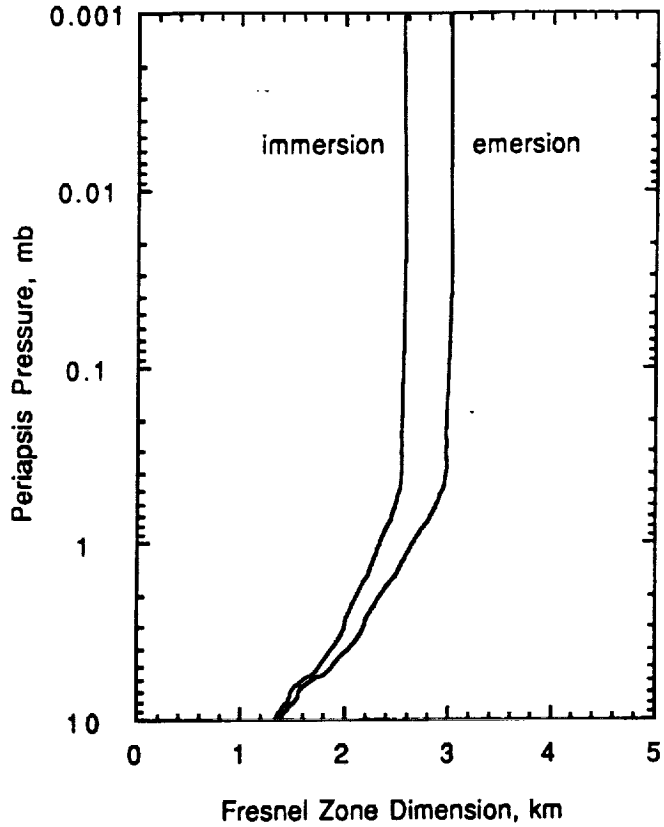

FIG. B1. Vertical dimension of Fresnel zone for the occultation of Voyager 2 by Uranus as computed from standard formulas (Haugstad 1978, Hubbard *et al.* 1978, Hinson 1986). The calculations require an accurate reconstruction of the spacecraft trajectory, which was provided by the Voyager Navigation Team, as well as measurements of the ambient background structure of the atmosphere (cf. Fig. 2). As periapsis pressure increases, the vertical dimension of the Fresnel zone decreases steadily from its free-space value. The nonisothermal structure of the atmosphere causes the inflections that appear in the curves. Fresnel-zone dimension is larger at emersion than at immersion due to an increase in spacecraft to planet distance, D_1.

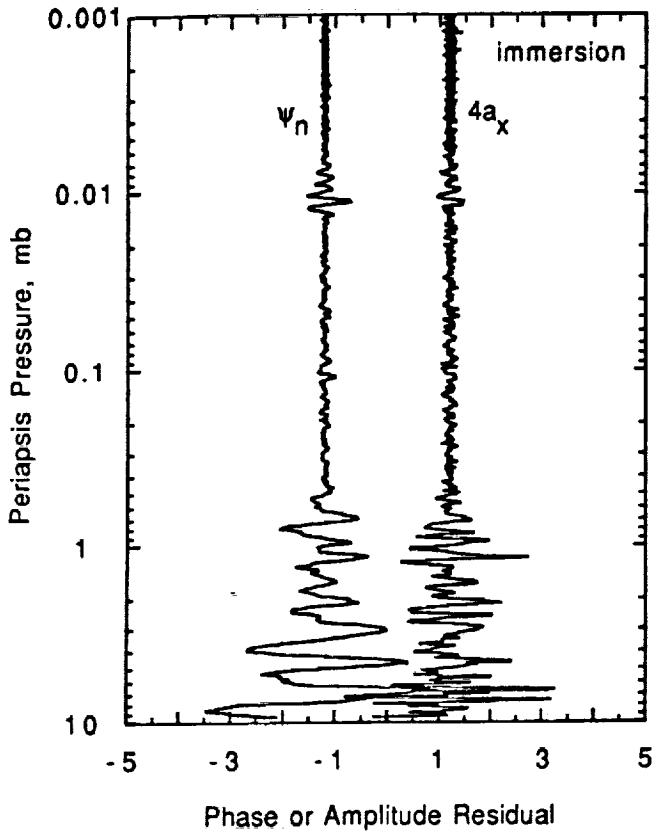

FIG. B2. Amplitude residuals at x-band, a_x, from data recorded at Parkes along with plasma-corrected phase residuals, ψ_n, from immersion. The latter also appeared in Fig. 9. The high degree of correlation between the two profiles, including the oscillatory feature centered near 0.01 mbar, confirms the accuracy of both sets of data. Moreover, the relative magnitude of the effects in a_x and ψ_n is consistent with diffraction theory [Eqs. (5)–(8)], which also predicts that the characteristic spatial scale of the amplitude residuals should decrease with increasing periapsis pressure, as observed [cf. Eq. (B1) and Fig. B1].

tion distorts the diffraction pattern observed at the receiving antenna. Second, the formulas for the Fresnel filters become

$$F_a = \sin(\pi\lambda D_1\zeta/l^2) \tag{B1}$$

$$F_\phi = \cos(\pi\lambda D_1\zeta/l^2). \tag{B2}$$

The factor ζ, which represents the effect of the background structure, acts to distort the vertical dimension of the Fresnel zone, F_z, to size $\sqrt{\lambda D_1\zeta}$. Using an explicit formula for ζ, which can be found in the references cited above, we calculated the variation of F_z during the occultation of Voyager 2 by the stratosphere of Uranus; the results appear in Fig. B1. As the ray path moves deeper into the atmosphere, F_z decreases steadily from its free-space value; it is reduced by a factor of about 2 for periapsis at 10 mbars.

As diffraction effects are inherently more prominent in amplitude data than phase data [cf. Eqs. (5)–(8)], we were unable to find a simple formula analogous to Eq. (9) for removing plasma effects from the amplitude residuals. Instead, we focus on amplitude data at x-band for which plasma effects are greatly reduced relative to data at s-band.

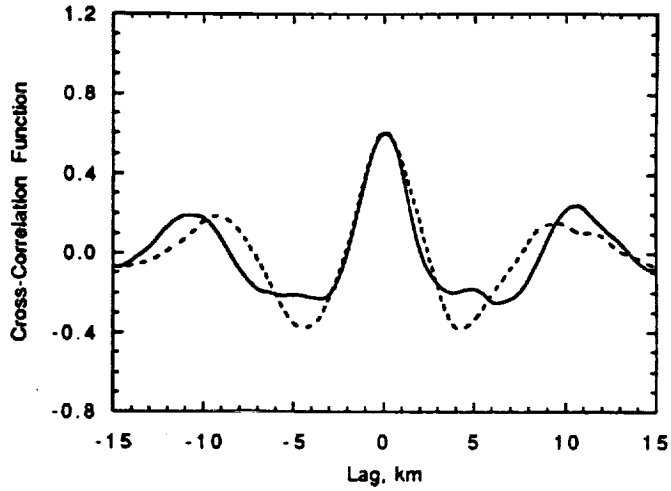

FIG. B3. Cross correlation of amplitude and phase residuals. Measurements at both immersion (solid line) and emersion (dashed line) show a strong positive peak at zero lag, as expected from Eqs. (5)–(8), and a periodicity of about 10 km, the same as was observed in correlations of phase data (Fig. 13).

Figure B2 displays amplitude residuals at x-band, a_x, along with plasma-corrected phase residuals, ψ_n, measured during immersion. The analogous comparison of phase and amplitude residuals at emersion is similar in apperance.

As noted earlier in connection with Fig. 9, the phase residuals oscillate with a vertical scale of about 10 km for pressures exceeding 0.4 mbar. Recall that atmospheric structure on this spatial scale is more efficient at producing phase perturbations than amplitude perturbations [see discussion following Eqs. (5)–(8)]. Specifically, the Fresnel filter for phase, F_ϕ, is four times larger than the Fresnel filter for amplitude, F_a, for atmospheric structure with a scale of 10 km (cf. Fig. 4). With this in mind, we scaled a_x by a factor of 4 in Fig. B2 so that the signature of the neutral atmosphere should appear the same in both sets of data.

A close comparison of the amplitude and phase residuals in Fig. B2 reveals a strong similarity for pressures exceeding 0.4 mbar where the effects of the neutral atmosphere predominate over measurement noise. The amplitude residuals also mimic the phase residuals in exhibiting an oscillatory feature centered near 0.01 mbar at immersion. Hence, the amplitude measurements generally confirm the accuracy of the phase measurements. This corroboration is particularly strong for two reasons. First, the amplitude and phase measurements have distinctly different sensitivities to the various sources of noise in the experiment. Second, these phase and amplitude data were recorded at different ground antennas (Canberra and Parkes, respectively).

The spatial variations in the occulting atmosphere that are most efficient at producing amplitude fluctuations are roughly the size of the Fresnel zone or smaller. Moreover, the vertical scale of the Fresnel zone decreases as periapsis pressure increases due to the influence of the ambient background structure of the atmosphere [cf. Eq. (B1) and Fig. B1]. Consequently, we expect the characteristic spatial scale of the amplitude residuals to decrease as periapsis pressure increases. This behavior is evident in Fig. B2 and accounts for the principal difference between the amplitude and phase residuals.

Finally, we compared the amplitude and phase residuals quantitatively by computing cross correlations. The results, shown in Fig. B3, substantiate the qualitative interpretation of the amplitude and phase residuals given in connection with Fig. B2.

sel/ca/KL

AUTHOR SEE QUERY ON MS P 45

ACKNOWLEDGMENTS

This work was made possible through funding from NASA under Grant NAGW-1180 of the Uranus Data Analysis Program. We are grateful to F. M. Flasar for computing radiative time constants for the stratosphere of Uranus; to G. L. Tyler for advice about digital filters and for comments on an early version of the manuscript; to both M. D. Allison and J. Bishop for providing preliminary versions of their respective manuscripts on related research; and to J. F. Appleby for providing a tabulation of his favorite radiative–convective equilibrium model for Uranus. We are indebted to the Voyager Project in general and the Radio Science Team in particular for their roles in planning and executing the highly successful flyby of Uranus with Voyager 2. Finally, we thank F. M. Flasar and M. D. Allison for thought-provoking comments as reviewers of the manuscript.

REFERENCES

ABRAMOWITZ, M., AND I. A. STEGUN 1972. *Handbook of Mathematical Functions*, 10th ed. U.S. Govt. Printing Office, Washington, DC.

ALLISON, M. 1990. Planetary waves in Jupiter's equatorial atmosphere. *Icarus* **83**, 282–307.

ALLISON, M., R. F. BEEBE, B. J. CONRATH, D. P. HINSON, AND A. P. INGERSOLL 1991. Uranus' atmospheric dynamics and circulation. In *Uranus* (J. T. Bergstralh and E. Miner, Eds.), Univ. of Arizona Press, Tucson. ? pp. 253–315

ANDREWS, D. G., J. R. HOLTON, AND C. B. LEOVY 1987. *Middle Atmosphere Dynamics*. Academic Press, Orlando.

ANDREWS, D. G., AND M. E. MCINTYRE 1976. Planetary waves in horizontal and vertical shear: The generalized Eliassen–Palm relation and the mean zonal acceleration. *J. Atmos. Sci.* **33**, 2031–2048.

APPLEBY, J. F. 1986. Radiative–convective equilibrium models of Uranus and Neptune. *Icarus* **65**, 383–405.

ATREYA, S. K., B. R. SANDEL, AND P. N. ROMANI 1991. Photochemistry and vertical mixing. In *Uranus* (J. T. Bergstralh and E. Miner, Eds.), Univ. of Arizona Press, Tucson. ? pp. 110–146

BEER, T. 1978. Tropical waves. *Rev. Geophys. Space Phys.* **16**, 567–582.

BISHOP, J., S. K. ATREYA, F. HERBERT, AND P. ROMANI 1990. Reanalysis of Voyager 2 UVS occultations at Uranus: Hydrocarbon mixing ratios in the equatorial stratosphere. *Icarus* **88**, 448–464.

BORN, M., AND E. WOLF 1975. *Principles of Optics*, 5th ed. Pergamon, Oxford.

BOYD, J. P. 1976. The noninteraction of waves with the zonally averaged flow on a spherical Earth and the interrelationships of eddy fluxes of energy, heat and momentum. *J. Atmos. Sci.* **33**, 2285–2291.

BRACEWELL, R. N. 1986. *The Fourier Transform and Its Applications*, 2nd ed., revised. McGraw-Hill, New York.

BRAMLEY, E. N. 1977. The accuracy of computing ionospheric radio-wave scintillation by the thin-phase-screen approximation. *J. Atmos. Terr. Phys.* **39**, 367–373.

BRIGHAM, E. O. 1974. *The Fast Fourier Transform*. Prentice-Hall, Englewood Cliffs, NJ.

BROADFOOT, A. L., F. HERBERT, J. B. HOLBERG, D. M. HUNTEN, S. KUMAR, B. R. SANDEL, D. E. SHEMANSKY, G. R. SMITH, R. V. YELLE, D. F. STROBEL, H. W. MOOS, T. M. DONAHUE, S. K. ATREYA, J. L. BERTAUX, J. E. BLAMONT, J. C. MCCONNELL, A. J. DESSLER, S. LINICK, AND R. SPRINGER 1986. Ultraviolet spectrometer observations of Uranus. *Science* **233**, 74–79.

CONNERNEY, J. E. P., M. H. ACUNA, AND N. F. NESS 1987. The magnetic field of Uranus. *J. Geophys. Res.* **92**, 15329–15336.

CONRATH, B., D. GAUTIER, R. HANEL, G. LINDAL, AND A. MARTEN 1987. The helium abundance of Uranus from Voyager measurements. *J. Geophys. Res.* **92**, 15,003–15,010.

CONRATH, B. J., P. J. GIERASCH, AND S. S. LEROY 1990. Temperature and circulation in the stratosphere of the outer planets. *Icarus* **83**, 255–281.

DAVIES, M. E., V. K. ABALAKIN, J. H. LIESKE, P. K. SEIDELMANN, A. T. SINCLAIR, A. M. SINZI, B. A. SMITH, AND Y. S. TJUFLIN 1983. Report of the IAU working group on cartographic coordinates and rotational elements of the planets and satellites: 1982. *Celest. Mech.* **29**, 309–321.

DUNKERTON, T. J. 1979. On the role of the Kelvin wave in the westerly phase of the semiannual zonal wind oscillation. *J. Atmos. Sci.* **36**, 32–41.

DUNKERTON, T. J. 1982. Theory of the mesopause semiannual oscillation. *J. Atmos. Sci.* **39**, 2681–2690.

ESHLEMAN, V. R., G. L. TYLER, J. D. ANDERSON, G. FJELDBO, G. S. LEVY, G. E. WOOD, AND T. A. CROFT 1977. Radio science investigations with Voyager. *Space Sci. Rev.* **21**, 207–232.

FLASAR, F. M., B. J. CONRATH, P. J. GIERASCH, AND J. A. PIRRAGLIA 1987. Voyager infrared observations of Uranus' atmosphere: Thermal structure and dynamics. *J. Geophys. Res.* **92**, 15,011–15,018.

FRENCH, R. G., J. L. ELLIOT, E. W. DUNHAM, D. A. ALLEN, J. H. ELIAS, J. A. FROGEL, AND W. LILLER 1983. The thermal structure and energy balance of the Uranian upper atmosphere. *Icarus* **53**, 399–414.

FRENCH, R. G., AND P. J. GIERASCH 1974. Waves in the Jovian upper atmosphere. *J. Atmos. Sci.* **31**, 1707–1712.

FRENCH, R. G., AND R. V. E. LOVELACE 1983. Strong turbulence and atmospheric waves in stellar occultations. *Icarus* **56**, 122–146.

GILL, A. E. 1982. *Atmosphere–Ocean Dynamics*. Academic Press, San Diego.

GOODMAN, J. W. 1968. *Introduction to Fourier Optics*. McGraw-Hill, San Francisco.

HAMMING, R. W. 1989. *Digital Filters*, 3rd ed. Prentice-Hall, Englewood Cliffs, NJ.

HAUGSTAD, B. S. 1978. Effects of the inhomogeneous background on radiation propagating through turbulent planetary atmospheres. *Radio Sci.* **13**, 435–440.

HERBERT, F., B. R. SANDEL, R. V. YELLE, J. B. HOLBERG, A. L. BROADFOOT, D. E. SHEMANSKY, S. K. ATREYA, AND P. N. ROMANI 1987. The upper atmosphere of Uranus: EUV occultations observed by Voyager 2. *J. Geophys. Res.* **92**, 15,093–15,109.

HINSON, D. P. 1986. Strong scintillations during atmospheric occultations: Theoretical intensity spectra. *Radio Sci.* **21**, 257–270.

HINSON, D. P., AND G. L. TYLER 1983. Internal gravity waves in Titan's atmosphere observed by Voyager radio occultation. *Icarus* **54**, 337–352.

HOLTON, J. R. 1979. Equatorial wave-mean flow interaction: A numerical study of the role of latitudinal shear. *J. Atmos. Sci.* **36**, 1030–1040.

HOLTON, J. R., AND R. S. LINDZEN 1972. An updated theory for the quasi-biennial cycle of the tropical stratosphere. *J. Atmos. Sci.* **29**, 1076–1080.

HUBBARD, W. B., J. R. JOKIPII, AND B. A. WILKING 1978. Stellar occultations by turbulent planetary atmospheres: A wave-optical theory including a finite scale height. *Icarus* **34**, 374–395.

LEBEDEV, N. N. 1972. *Special Functions and Their Applications*. Dover, New York.

LINDAL, G. F., G. E. WOOD, H. B. HOTZ, D. N. SWEETNAM, V. R. ESHLEMAN, AND G. L. TYLER 1983. The atmosphere of Titan: An

pel/am/KL

analysis of the Voyager 1 radio occultation measurements. *Icarus* **53**, 348–363.

LINDAL, G. F., J. R. LYONS, D. N. SWEETNAM, V. R. ESHLEMAN, D. P. HINSON, AND G. L. TYLER 1987. The atmosphere of Uranus: Results of radio occultation measurements with Voyager 2. *J. Geophys. Res.* **92**, 14,987–15,001.

LINDZEN, R. S. 1971. Equatorial planetary waves in shear: Part I. *J. Atmos. Sci.* **28**, 609–622.

LINDZEN, R. S. 1972. Equatorial planetary waves in shear: Part II. *J. Atmos. Sci.* **29**, 1452–1463.

LINDZEN, R. S. 1981. Turbulence and stress owing to gravity wave and tidal breakdown. *J. Geophys. Res.* **86**, 9707–9714.

LIPA, B., AND G. L. TYLER 1979. Statistical and computational uncertainties in atmospheric profiles from radio occultation: Mariner 10 at Venus. *Icarus* **39**, 192–208.

OPPENHEIM, A. V., AND R. W. SCHAFER 1975. *Digital Signal Processing*. Prentice-Hall, Englewood Cliffs, NJ.

POLLACK, J. B., K. RAGES, S. K. POPE, M. G. TOMASKO, P. N. ROMANI, AND S. K. ATREYA 1987. Nature of stratospheric haze on Uranus: Evidence for condensed hydrocarbons. *J. Geophys. Res.* **92**, 15,037–15,065.

SALPETER, E. E. 1967. Interplanetary scintillations. I. Theory. *Astrophys. J.* **147**, 433–448.

TOULOUKIAN, Y. S., S. C. SAXENA, AND P. HESTERMANS 1975. *Thermophysical Properties of Matter, Vol. 11, Viscosity*. IFI/Plenum, New York.

TURNER, J. S. 1973. *Buoyancy Effects in Fluids*. Cambridge Univ. Press, Cambridge.

TYLER, G. L., D. N. SWEETNAM, J. D. ANDERSON, J. K. CAMPBELL, V. R. ESHLEMAN, D. P. HINSON, G. S. LEVY, G. F. LINDAL, E. A. MAROUF, AND R. A. SIMPSON 1986. Voyager 2 radio science observations of the Uranian System: Atmosphere, rings, and satellites. *Science* **233**, 79–84.

JOURNAL OF GEOPHYSICAL RESEARCH, VOL. 92, NO. A13, PAGES 14,987–15,001, DECEMBER 30, 1987

The Atmosphere of Uranus: Results of Radio Occultation Measurements With Voyager 2

G. F. LINDAL, J. R. LYONS, AND D. N. SWEETNAM

Jet Propulsion Laboratory, California Institute of Technology, Pasadena

V. R. ESHLEMAN, D. P. HINSON, AND G. L. TYLER

Center for Radar Astronomy, Stanford University, Stanford, California

During Voyager 2's occultation by Uranus the radio link from the spacecraft probed the atmosphere of the planet at latitudes ranging from 2° to 7° south. The measurements, which were conducted at two coherently related wavelengths, namely, 13 cm (S band) and 3.6 cm (X band), did not show any clear signs of microwave absorption. However, the Doppler frequency perturbations observed on the radio link have provided new data on the equatorial radius and atmosphere of the planet. From integral inversion of the Doppler data, profiles in height of the electron number density in the ionosphere and the gas refractivity, number density, pressure, temperature, and methane abundance in the troposphere and stratosphere have been determined. The gas data were acquired in the pressure range from about 0.3 mbar to 2.3 bars over an altitude interval of approximately 250 km. At the 2.3-bar level the nominal model has a temperature of 101 K with a 1σ uncertainty of 2 K when the uncertainty in the composition is assumed to be negligible. The corresponding temperature lapse rate is 0.95 ± 0.1 K/km. A 2- to 4-km-thick layer with a small refractivity scale height was detected during ingress and egress, which is consistent with the presence of a methane cloud layer centered at the 1.2-bar level. For the nominal model the methane mixing ratio below the base of the cloud is 2.3% by number density. At the tropopause, which was observed near the 100-mbar level, the temperature is 53 ± 1 K. A comparison with infrared data acquired with the infrared interferometer spectrometer instrument on board the Voyager spacecraft indicates that the gas in this region consists of $85 \pm 3\%$ hydrogen with the remainder being mostly helium. Above the tropopause the gas temperature increases with increasing altitude, reaching 114 ± 10 K near the 0.5-mbar level. Several warm layers, which may be produced by absorption of solar radiation by hydrocarbon aerosols, were detected in the stratosphere. From the data acquired at ingress and egress the shape and size of the isobaric surfaces of Uranus have been determined. The shape indicates that the gas in the region probed by the link rotates with an average period of about 18 hours, which corresponds to a zonal wind velocity of 110 m/s relative to the magnetic field. This implies that the equatorial atmosphere rotates slower than the interior, in contrast to the situation at Jupiter and Saturn. The 1-bar isobaric surface has an equatorial radius of $25,559 \pm 4$ km. Extrapolating from the equator to the south pole by using available data on the gravity field and the zonal wind velocities gives a polar radius of $24,973 \pm 20$ km. The corresponding oblateness, $(R_{eq} - R_p)/R_{eq}$, is 0.02293 ± 0.00080.

INTRODUCTION

On January 24, 1986, the Voyager 2 spacecraft was occulted by Uranus and its rings [*Stone and Miner*, 1986]. Both events were observed with radio tracking systems at NASA's Deep Space Network and at the Parkes Radio Astronomy Observatory [*Tyler et al.*, 1986]. Figure 1 depicts the geometry of the encounter as viewed from Earth.

Two coherently related radio signals were transmitted from Voyager 2 during the occultation experiments, one at S band (2.3 GHz) and the other at X band (8.4 GHz). Both signals were derived from a stable spacecraft oscillator located in a temperature-controlled oven, and transmission to Earth was accomplished with a 3.66-m-diameter parabolic dish rigidly fastened to the spacecraft.

In order to keep the refracted radio beam pointed at the receiving stations during the atmospheric occultation experiment the spacecraft was turned so the antenna boresight tracked the virtual image of Earth on the limb of Uranus throughout the data acquisition period. This approach allowed the radio signals from the spacecraft to be recorded during the entire occultation period and the atmosphere to be sampled at planetographic latitudes ranging from about 2° to 7°S.

Station instrumentation employed in the recording of the spacecraft signals consisted of wideband and phase-locked-loop receiver channels with digitized outputs. The recording bandwidths used in the wideband receiver channels were 20 kHz at both S and X band. A 2-MHz backup recording system was also in operation. Detailed descriptions of the instrumentation have been provided in earlier publications [*Eshleman et al.*, 1977; *Edelson et al.*, 1979].

The wideband recordings are usually considered the primary data sets for atmospheric studies. That is because they allow detection of many signal modes appearing simultaneously at different frequencies during periods of multipath propagation and also because they provide the highest signal-to-noise ratios. The phase-locked-loop data, which contain samples of the amplitude and frequency of the signal mode that was tracked by the receiver loop, are being used mainly for preliminary studies when limited time is available for data processing. Results from the initial reduction of the phase-locked-loop records were included in the preliminary team paper [*Tyler et al.*, 1986]. The primary objective of this paper is to summarize what has been learned about the Uranian atmosphere from a detailed analysis of the wideband recordings.

Copyright 1987 by the American Geophysical Union.

Paper number 7A8930.
0148-0227/87/007A-8930$05.00

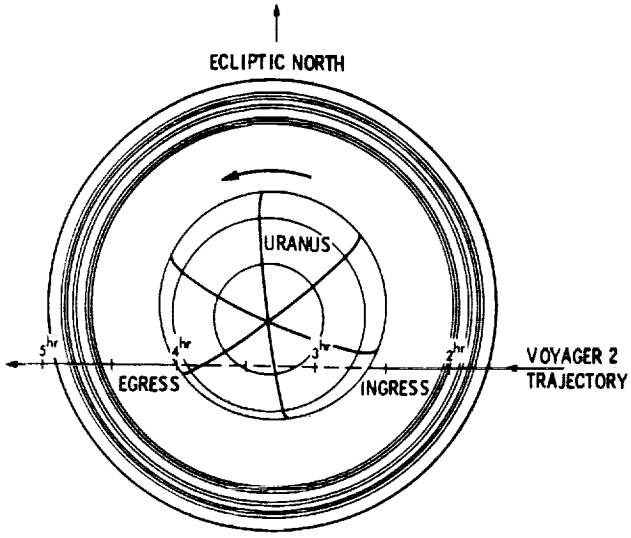

Fig. 1. View from Earth of Voyager 2's encounter with Uranus. The spacecraft was occulted by both the planet and its rings. Time is marked along the spacecraft trajectory in hours past periapsis passage, which occurred at 1759 UT on January 24, 1986. At ingress and egress the spacecraft was 185,400 km and 255,700 km behind the occulting limb, respectively. According to current International Astronomical Union conventions, the south pole of Uranus was facing Earth at the time of the encounter [*Davies et al.*, 1983]. Viewed from the Earth, the planet was rotating in the anticlockwise direction.

DATA ANALYSIS AND RESULTS

The first step in the processing of the wideband recordings consisted of digitally filtering and decimating the data. The bandwidth reduced data were subsequently mixed with the signal from a local oscillator that was programmed to compensate for the changing Doppler shifts. Signal detection was performed with the help of computer software which determines the amplitude and frequency of the various propagation modes.

Figure 2 shows the power and Doppler frequency perturbations observed while the tracking link was being refracted in the atmosphere of Uranus. These data were acquired with the X band receiver channel at Deep Space Station (DSS) 43. As illustrated in the upper portion of the figure, the spacecraft signal was affected by atmospheric defocusing and scintillations. For example, the drop in the signal intensity observed at about 2321 UT was caused by defocusing as the link moved down below the 10-mbar level in the stratosphere during ingress. Another abrupt signal power drop at 2337 UT was due to defocusing in a turbulent layer with a relatively small scale height, located at the 1.2-bar level. This region, which is believed to contain a methane cloud layer [*Tyler et al.*, 1986; *Eshleman et al.*, 1986; *Lindal et al.*, 1986], also produced multipath propagation. The multipath effects, which started at about 2343 UT and lasted for several minutes, caused three different signals to appear simultaneously in the radio recordings. The frequency separation between these multipath modes is too small to be distinguishable in the lower panel of Figure 2. Instead these effects are illustrated with the power spectra displayed in Figure 3. Ingress ended at about 0002 UT as the link reached its lowest level in the troposphere of Uranus—approximately 2.3 bars. Similar effects were observed during egress.

The signal perturbations recorded during the occultation experiment have been used to study the vertical structure of the Uranian atmosphere. This was done by assuming perfect horizontal stratification in the atmospheric region probed by the radio link and by inverting the integral equations relating the observed intensity and frequency perturbations to the vertical absorption coefficient and refractivity profiles of the atmosphere. Inversion of the signal intensity data did not reveal any clear evidence of microwave absorption. However, the Doppler measurements provided interesting new data on the refractive properties of the atmosphere.

As discussed below, the ingress and egress Doppler data files have been used to derive two separate vertical refractivity profiles in the equatorial region of Uranus. The mathematical solution employed in these calculations was obtained by noting that each recorded Doppler value corresponds to a ray, or photon trajectory, which at its lowest point in the atmosphere tangentially grazes a geoid. By starting with the ray grazing the top of the atmosphere and proceeding downward, the refractivity was computed in a sequential manner at the altitudes corresponding to the lowest geodetic level reached by each ray. The shape of the geoids was determined from data on the external gravity field and the zonal wind velocity or rotation period of the atmosphere.

Haze prevented the imaging system on the spacecraft from detecting any cloud motion in the equatorial atmosphere of Uranus [*Smith et al.*, 1986]. In the preliminary phase of the occultation analysis it therefore seemed appropriate to use the magnetic field rotation period in lieu of a more direct observation of the gas rotation period. However, this led to a discrepancy between the refractivity profiles computed from the ingress and egress measurements, in that the two profile computations did not yield the same gas refractivity at the occultation midpoint. Since the uncertainties in the spacecraft ephemeris and in the external gravity field and pole direction of Uranus [*French et al.*, 1986; J. K. Campbell, personal communication, 1986] appear to be too small to account for the refractivity difference, it was concluded that the discrepancy was caused by the use of an incorrect rotation period in the computation of the shape of the geoids. The problem was therefore resolved by using the radio occultation data to iteratively solve for the gas rotation period that produced the same refractivity at the occultation midpoint for both the ingress and the egress data sets.

Utilizing the radio occultation data to solve for the gas rotation period yielded an average value of 18.0 ± 0.3 hours in the region sampled by the link. By comparison, the magnetic field rotates with a period of 17.24 ± 0.1 hours [*Ness et al.*, 1986; *Stone et al.*, 1986; *Warwick et al.*, 1986]. Since the magnetic field is believed to be tied to the interior of the planet [*Ness et al.*, 1986], this result implies that the equatorial atmosphere rotates slower than the interior. Such an equatorial subrotation has been predicted by *Read* [1986] based on studies of axisymmetric circulation models.

The equatorial rotation period calculated from the radio occultation measurements corresponds to a zonal wind velocity of -110 ± 40 m/s relative to the magnetic field. Figure 4 illustrates how this result compares with studies of the cloud motion between 25 and 71° S latitude conducted by *Smith et al.* [1986]. As can be seen from the figure, the gas evidently rotates faster than the interior to the south of $-20°$ latitude and slower than the interior near the equator. This latitude dependence is suggestive of the meridional type circulation expected in a Hadley cell. Indeed, Read's work indicates that solar heating in the polar region may cause the gas in that

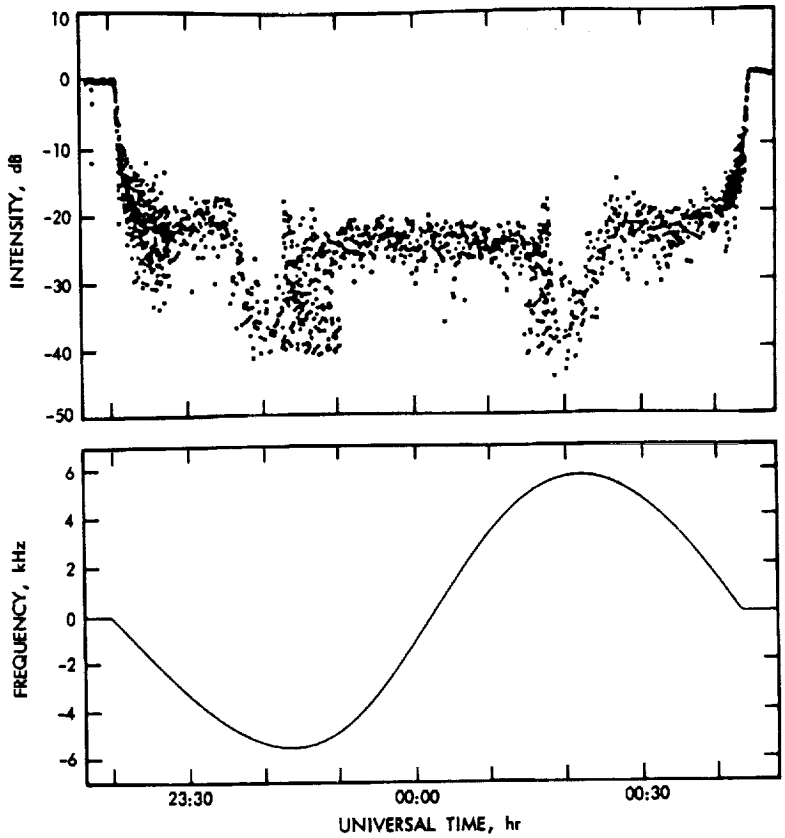

Fig. 2. Signal intensity and Doppler frequency perturbations recorded at X band during Voyager 2's occultation by Uranus. The data were acquired with a wideband receiver channel at Deep Space Station (DSS) 43 located in Australia. The measurements were made on January 24–25, 1986. Time of signal reception is marked in hours past midnight. It took about 2 hours 45 min for the signal to travel from the spacecraft to Earth. In order to maximize the signal-to-noise ratio during the atmospheric measurements the spacecraft was maneuvered so that its antenna tracked the virtual image of Earth on the limb of Uranus. The radio link probed the Uranian atmosphere at latitudes ranging from 2° to 7°S.

area to rise and flow toward the equator at high altitudes and return to the pole at lower levels [*Read*, 1986]. Due to quasi-conservation of angular momentum, this type of circulation is expected to cause subrotation in the equatorial region and superrotation at higher latitudes. A somewhat more complex circulation model containing several Hadley cells has been proposed by *Flasar et al.* [this issue] based on studies of the latitudinal temperature variations observed with the infrared interferometer spectrometer (IRIS) instrument carried on board the Voyager spacecraft. However, both models indicate that the global circulation should cause gas to descend and subrotate in the equatorial region. In this regard, Uranus appears to differ from Jupiter and Saturn, where internal heat sources may play a more important role in controlling the circulation [*Read*, 1986].

Figure 5 depicts the vertical refractivity profile computed from the signal modes detected during ingress. As is common in studies of microwave propagation in the terrestrial troposphere, the refractivity (N) is defined here as the refractive index of the atmosphere reduced by one and multiplied by 10^6 [*Evans and Hagfors*, 1966]. The profile calculations were performed by assuming that horizontal changes in the number density and composition, and hence the refractivity, are negligible in the region probed by the radio link. This seems to be a reasonable assumption, since the pressure is expected to remain relatively constant along geoids and furthermore because infrared measurements [*Hanel et al.*, 1986; *Flasar et al.*, this issue] and model studies [*Friedson and Ingersoll*, 1987] indicate that the horizontal temperature variations are small within the latitude range of interest here. It should also be noted that horizontal stratification appears to be confirmed by the results of the calculations, since there is little difference between the ingress and egress profiles computed in this manner.

In order to determine the number density distribution of the atmosphere from the refractivity data it is necessary to know the composition. Earth-based observations indicate that the Uranian atmosphere consists primarily of hydrogen (H_2), helium (He), and methane (CH_4) [*Hunten*, 1984; *Trafton*, 1981; *Wallace*, 1980]. Additional information on the gas composition can be obtained from the thermal structure of the atmosphere. Infrared data acquired with the IRIS instrument yielded tropopause temperatures ranging from 51.5 to 54.5 K [*Hanel et al.*, 1986]. Using these temperature measurements together with data on the vapor pressure of methane gives an upper limit for the mixing ratio or mole fraction of CH_4 near the tropopause of the order of 0.01%. Even lower values have been reported for the stratosphere [*Herbert et al.*, this issue; *Orton et al.*, 1987]. This implies that methane is expected to have negligible effects on the atmospheric refractivity and mean molecular mass near the tropopause and in the stratosphere, and the same appears to be true with regard to the other hydrocarbon vapors and aerosols that have been detected in this region of the Uranian atmosphere [*Herbert et al.*, this issue; *Orton et al.*, 1987; *Pollack et al.*, this issue]. As we shall come back to later, the methane abundance does not

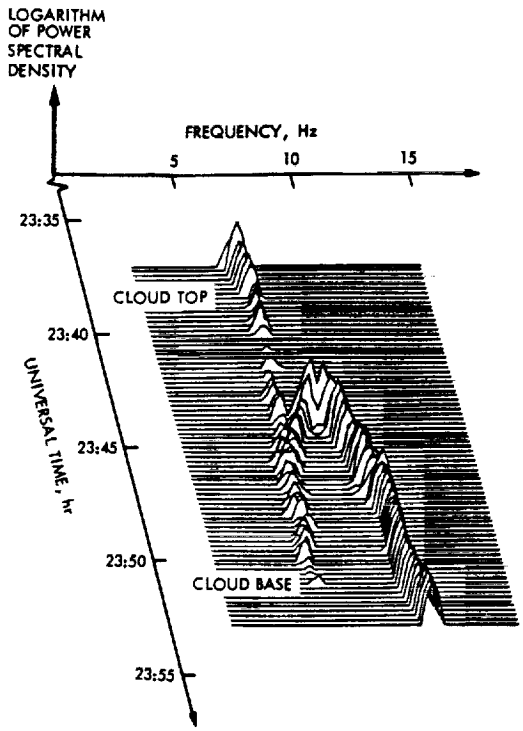

Fig. 3. Power spectra showing defocusing, multipath propagation, and scintillations on the X band link as it passed through a turbulent methane cloud layer in the troposphere of Uranus. Time of signal reception is marked in hours past midnight. The small refractivity scale height of the cloud layer caused multipath propagation, with the signal radiated from the spacecraft reaching the tracking station simultaneously via three different paths through the cloud layer, one with ray-periapsis within the cloud and two below. Since the Doppler shifts for the three ray paths differ, they give rise to three separate signals in the radio recordings. The spectra labeled "cloud top" and "cloud base" correspond to rays that tangentially graze the top and the base of the cloud layer, respectively. Note that the signal modes have been heterodyned by using a variable local oscillator frequency which compensates for the changing Doppler shift. In order to obtain reliable refractivity profiles it is necessary to detect all signal modes passing through the atmosphere.

seem to be negligible below the 700-mbar level, however, and this is a region where infrared observations indicate a CH_4 mixing ratio in the range of 0.3–10% [*Owen*, 1966; *Wallace*, 1980; *Trafton*, 1981; *Baines*, 1983; *Teifel*, 1983; *Bergstralh and Baines*, 1984; *Baines and Bergstralh*, 1986].

In the appendix of this paper it is shown that the atmospheric temperature calculated from the radio refractivity data is approximately proportional to the mean molecular mass when the constituents are uniformly mixed. Solving for the mean molecular mass, which makes the radio temperature profiles agree with the infrared temperature data acquired near the equatorial tropopause, yields a value of 2.31 ± 0.06 amu. This value for the mean molecular mass gives an upper limit for the helium mixing ratio of $15 \pm 3\%$ by number density when the remainder is assumed to be hydrogen [*Conrath et al.*, this issue; *Hanel et al.*, 1986; *Tyler et al.*, 1986; *Eshleman et al.*, 1986; *Gautier et al.*, 1986; *Lindal et al.*, 1986]. Of course, if the atmosphere contains heavier gases such as nitrogen [*Orton and Appleby*, 1984; *Orton et al.*, 1986], then less helium is needed in order to produce a mean molecular mass of 2.31 amu. By comparison, data on the solar system abundances of the elements [*Cameron*, 1982; *Anders and Ebihara*, 1982] suggest a helium mixing ratio of 12–16% for Uranus if differentiation has not occurred.

For the purpose of interpreting the refractivity data we have adopted an atmospheric composition of 85% hydrogen and 15% helium by number density near the tropopause, and the helium to hydrogen abundance ratio is assumed to be independent of altitude. The bottom scale in Figure 5 shows the result of converting the radio refractivity to number density. As discussed in the appendix, the conversion was performed by utilizing microwave data on the refractive indexes of hydrogen, helium, and methane published by *Essen* [1953], *Orcutt and Cole* [1967], and *Bose et al.* [1972].

A detailed study of the refractivity data has revealed that the multipath propagation observed during ingress and egress was caused by a layer with a relatively small scale height centered at the 1.2-bar level. This layer, which is 2–4 km thick, is shown in the insert in the upper right-hand corner of Figure 5. We believe the abrupt change in the refractivity scale height seen in this region is caused by methane saturation. (Note that methane is expected to saturate at some level in the troposphere if its mixing ratio is greater than 0.01%.) Below the base of the layer the scale height is about 50 km, and here, methane presumably is uniformly mixed with hydrogen and helium. However, within the layer the scale height is only about 20 km, and what we see is apparently the effect of methane being frozen out as the temperature drops with increasing altitude.

It should be emphasized here that the refractivity profiles do not uniquely define the vertical changes in both the temperature and the composition of the gas. Thus in order to derive the temperature and methane distribution of the atmosphere from the radio data it was necessary to introduce constraints that would alleviate this ambiguity. The interpretation discussed below is based on the assumption that the layer with the small scale height is a region where methane is in the process of being frozen out of the atmosphere and presumably forms a cloud layer containing ice crystals and supercooled droplets. (The triple point of methane is at 90.7 K and 117 mbar.)

In order to use the refractivity data to determine the methane distribution in the cloud layer it was assumed that the temperature lapse rate in this region is equal to the so-called wet adiabat [*Houghton*, 1977]. For the remaining portions of the atmosphere some simplifying auxiliary assumptions were made regarding the methane distribution so that the refractivity data could be used instead to calculate the temperature profile. For example, below the base of the cloud the methane mixing ratio was taken to be constant and independent of altitude. Above the cloud top the methane mixing ratio is expected to vary greatly with altitude, and here, two different approaches were used in computing temperature profiles. In one set of calculations it was assumed that the relative humidity between the cloud top and the tropopause is constant and independent of altitude. (Note that the term relative humidity is defined here to mean the ratio between the partial pressure of methane and the saturation pressure of the vapor at the same temperature.) In another set of computations the methane distribution was modeled by considering the effects of upward eddy diffusion in an equatorial layer where the global circulation produces a downdraft. Both these approaches led basically to the same conclusion, namely, that the gas above the cloud top was not saturated with methane in the region sampled by the link. From the tropopause and upward the methane mixing ratio was taken to be constant. This is a reasonable simplification because the methane mixing ratio in the stratosphere is too low to have an appreciable effect on the

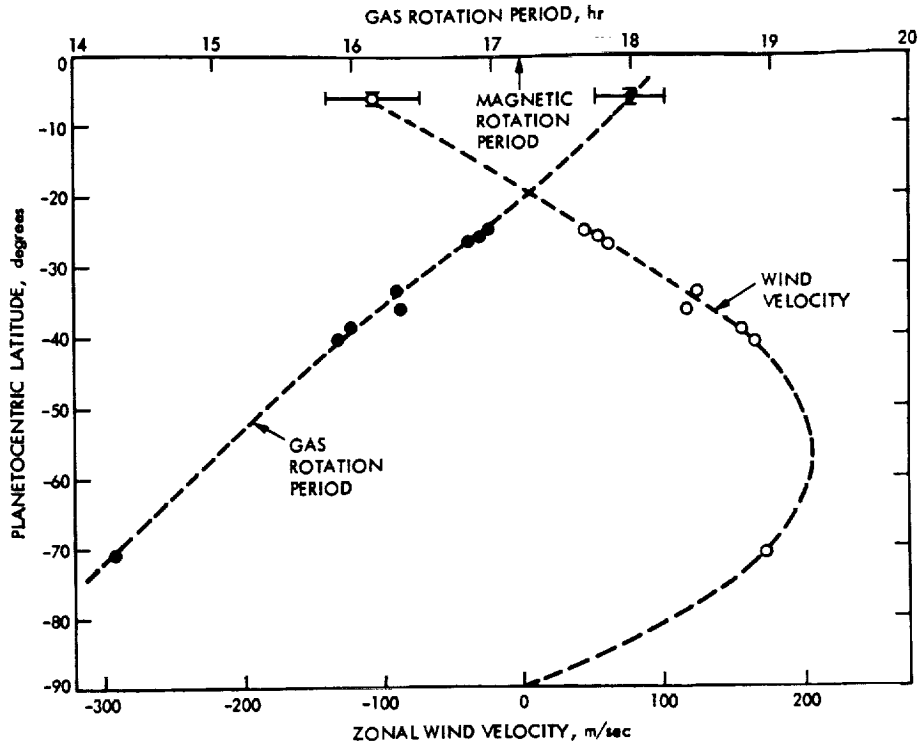

Fig. 4. Gas rotation period and westward zonal wind velocity in the southern hemisphere of Uranus. As discussed in the text, the wind velocity is given relative to the magnetic field, which presumably is tied to the interior of the planet [*Ness et al.*, 1986]. The data points shown near 5°S were derived from the radio occultation recordings, and the remaining points were obtained by tracking cloud features with the Voyager cameras [*Smith et al.*, 1986].

computed profiles [*Atreya and Romani*, 1983; *Herbert et al.*, this issue].

By using the assumptions outlined above the total number density (n_t), pressure (p), temperature (T), and methane mixing ratio (f_{CH_4}) were determined in a sequential manner for one geodetic altitude level at a time by starting at the top of the detectable atmosphere and moving downward. For the nominal model depicted in Figures 5 and 6 and listed in Table 1 the profiles were computed as follows. In the stratosphere the number density was calculated from the refractivity by using a methane mixing ratio of 3×10^{-5}, which corresponds to a relative humidity of 30% at the tropopause. (This is not a critical assumption, since, as we shall see in the next section, the methane abundance does not significantly influence the computed profiles above the 700-mbar level.) The pressure distribution was obtained by integrating the density using the equation for hydrostatic equilibrium. The temperature was determined, in turn, from the number density and the pressure by utilizing the equation of state.

From the tropopause and down to the cloud top the nominal atmosphere was assumed to have a relative humidity of 30%, and the gas state parameters were computed in an iterative manner at each altitude level where the refractivity profile was sampled. The iterative process was started by first selecting an initial value for the methane mixing ratio. The corresponding number density, pressure, and temperature were then computed as before. Next the methane saturation pressure was calculated from the gas temperature and vapor pressure data on methane. From this vapor saturation pressure and the value selected for the relative humidity a new methane mixing ratio was calculated. Before moving down to the next altitude level the computational procedure was repeated with the new methane mixing ratio until the solution converged.

Within the cloud layer the temperature profile was assumed to have a lapse rate corresponding to the so-called wet adiabat, and the refractivity data were used instead to determine f_{CH_4}, n_t, and p in an iterative manner at each altitude level where the refractivity was sampled. In the middle of the cloud layer, 10% of the methane was assumed to be in the condensed phase. The adiabatic lapse rate was computed for the case of "frozen" equilibrium hydrogen. (The term "frozen" equilibrium is used here to describe equilibrium H_2 in a situation where the rates of conversion between ortho and para H_2 states are too slow to have an appreciable effect on the temperature lapse rate [*Trafton*, 1967; *Wallace*, 1980; *Massie and Hunten*, 1982; *Orton et al.*, 1986]. For the nominal model shown in Figures 5 and 6 this led to a methane mole fraction of 2.3% at the cloud base. Below the cloud the methane mixing ratio was kept constant, and the refractivity data were again used to calculate n_t, p, and T. More information on the profile computations is available in the appendix.

The gas profiles obtained from the radio occultation experiment extend over an altitude interval of 250 km and a pressure range of 2.3 bars to 0.3 mbar. In the troposphere the depth of the measurements was limited by the spacecraft trajectory, which did not allow link bending angles greater than 3.07° to be observed. The height to which the gas could be detected in the stratosphere was limited by the stability of the spacecraft oscillator and by ionospheric scintillations, which produced spectral broadening of the received signals.

In the stratosphere the refractivity profiles show several changes in the scale height. We interpret these features in the refractivity data as thermal layers rather than vertical variations in the composition. The reason is that the mixing ratios reported for the hydrocarbons that make up the vapors and aerosol layers in the stratosphere [*Herbert et al.*, this issue;

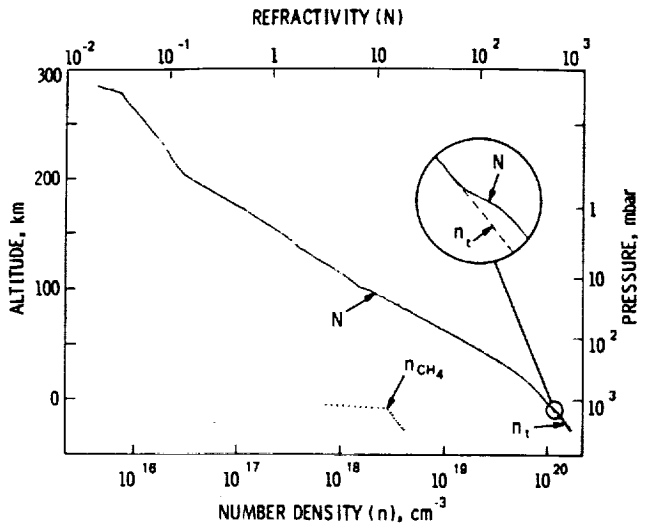

Fig. 5. Vertical refractivity profile derived from radio recordings made during ingress. The ordinate scale gives the local altitude of the measurements relative to the 1-bar (or 10 N/cm^2) pressure level. An expanded view of the refractivity in the altitude region where methane is believed to be condensing and forming a cloud layer is shown magnified 10 times in the upper right-hand corner of the graph. The scale at the bottom of the chart gives the number density for the nominal model. In this model, methane is 30% saturated above the cloud top. The methane distribution in the cloud layer was determined by setting the temperature lapse rate in this region equal to the adiabatic rate expected when CH_4 is condensing. Note that the number density distribution of methane (n_{CH_4}) derived in this manner includes molecules in the gas, liquid, and solid states. The total number density of the atmosphere is denoted n_t. As measured by the height of the first X band Fresnel zone, the altitude resolution of the data ranged from about 5 km near the top of the stratosphere to 50 m in the cloud layer. The corresponding horizontal resolution longitudinal to the link changed from about 700 to 100 km over the same altitude interval. (The horizontal resolution is defined here as the horizontal distance that a photon is traveling while being inside the lowest layer that it penetrates. In altitude this layer is centered on the lowest geodetic level reached by the photon, and it has a thickness equal to the vertical resolution of the data.)

Orton et al., 1987; *Pollack et al.*, this issue] are several orders of magnitude too low to account for the observed structure in the refractivity profiles.

Above the stratosphere one may use the radio data to study the vertical distribution of free electrons. Figure 7 depicts the electron number density profiles derived from the dispersive Doppler effects observed during ingress and egress. As in previous studies of Jupiter and Saturn the measurements show several dense, sharp layers in the lower ionosphere. These layers, which were detected below the 2000-km level, may consist of heavy ions of meteoric, ring, or satellite origin [*Chen*, 1981]. Above the 2000-km level there appears to be an extended ionized region with a low plasma density and large scale height. This region of the Uranian ionosphere is difficult to observe with the radio occultation experiment, however, since the subtle phase changes it produces on the radio link are easily masked by the effects of small plasma variations along the rest of the ray path, i.e., in the interplanetary medium and Earth's ionosphere. The high-altitude measurements therefore do not provide very precise information on the topside plasma scale height and temperature. It is nevertheless interesting to note that the topside of the ingress profile has a scale height of the order of 2400 km, which corresponds to a plasma temperature of roughly 800 K if the principal ion is H^+ and the plasma distribution is controlled by ambipolar diffusion. By comparison, the UV measurements conducted with Voyager 2 yielded a neutral gas temperature of 750 K in this altitude region [*Broadfoot et al.*, 1986; *Sandel et al.*, 1986].

Another aspect of the radio occultation experiment involves the amplitude scintillations caused by scattering from small-scale refractivity irregularities. These scintillations contain information concerning atmospheric structure and dynamics on spatial scales of a few kilometers or less and make possible the study of a variety of phenomena. For instance, past investigations of radio wave scattering observed during Voyager occultations have yielded magnetic field orientations in the ionospheres of Jupiter and Saturn that complement and extend the magnetometer data [*Hinson and Tyler*, 1982; *Hinson*, 1984] and have revealed internal gravity waves (or density waves) propagating through Titan's upper troposphere and stratosphere [*Hinson and Tyler*, 1983]. The scintillation data from Uranus are the subject of a separate investigation, which will be discussed in a later paper.

Figure 8 summarizes the data on the physical size and shape of Uranus. The two discrete points in the left-hand portion of the graph show the radii observed at the 1-bar level during ingress and egress. The solid curve represents the horizontal surface or geoid of a rotating fluid which best fits the radio occultation data. This geoid has an equatorial radius of 25,559 ± 4 km. Extrapolation to the south pole, which was performed by integrating data on the external gravity field [*French et al.*, 1986; J. K. Campbell, personal communication, 1986] and the zonal wind velocities observed with the imaging system on board the spacecraft [*Smith et al.*, 1986], yielded a polar radius of 24,973 km. (A detailed discussion on how the

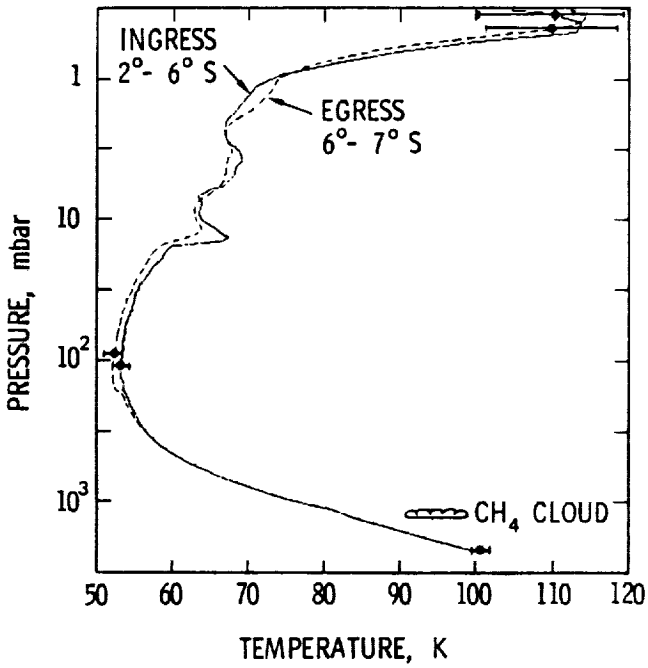

Fig. 6. Vertical temperature profiles for the nominal model. The solid curve was derived from the radio refractivity data acquired during ingress at planetographic latitudes ranging from 2° to 6° S. The dashed curve was obtained from measurements between 6 and 7° S latitude during egress. Both measurements were conducted near the terminator. The calculations were performed by using a helium to hydrogen abundance ratio of 15/85, and the error bars do not include the uncertainty in the composition.

TABLE 1. Atmospheric Data

p, mbar	$n_t \times 10^{-17}$, cm^{-3}	T, K	$n_{CH_4} \times 10^2/n_t$, %	h, km
0.25	0.19	96.1		232.5
0.28	0.20	100.1		227.7
0.32	0.22	105.3		222.7
0.35	0.23	110.4		217.5
0.40	0.25	113.4		212.1
0.45	0.29	113.3		206.6
0.50	0.34	107.3		201.4
0.56	0.42	98.0		196.4
0.63	0.50	90.8		191.9
0.71	0.60	85.6		187.7
0.79	0.71	80.8		183.6
0.89	0.85	75.8		179.8
1.00	0.99	73.0		176.3
1.12	1.14	71.0		172.8
1.26	1.30	70.2		169.4
1.41	1.48	69.4		166.0
1.58	1.67	68.6		162.6
1.78	1.90	67.8		159.4
2.00	2.16	67.0		156.1
2.24	2.43	66.8		152.9
2.51	2.72	66.8		149.7
2.82	3.04	67.1		146.4
3.16	3.36	68.2		143.1
3.55	3.73	68.8		139.9
3.98	4.20	68.7		136.5
4.47	4.75	68.1		133.2
5.01	5.35	67.9		130.0
5.62	6.08	67.0		126.7
6.31	7.07	64.6		123.6
7.08	8.10	63.3		120.5
7.94	9.04	63.6		117.4
8.91	10.18	63.4		114.4
10.00	11.42	63.4		111.3
11.22	12.58	64.6		108.2
12.59	13.79	66.1		105.1
14.13	15.36	66.6		101.9
15.85	19.25	59.6		98.8
17.78	21.93	58.7		96.0
19.95	24.81	58.2		93.2
22.39	28.29	57.3		90.4
25.12	32.12	56.6		87.7
28.18	36.46	56.0		85.0
31.62	41.31	55.5		82.3
35.48	46.64	55.1		79.7
39.81	52.58	54.8		77.0
44.67	59.27	54.6		74.4
50.12	67.07	54.1		71.8
56.23	75.81	53.7		69.2
63.10	85.21	53.6		66.6
70.79	95.66	53.6		64.1
79.43	107.62	53.5		61.5
89.13	120.96	53.4		59.0
100.00	136.20	53.2		56.4
109.65	149.87	53.0		54.4
120.23	163.86	53.1		52.3
131.83	179.54	53.2		50.3
144.54	195.66	53.5		48.3
158.49	214.68	53.5		46.2
173.78	234.12	53.8		44.2
190.55	254.70	54.2		42.1
208.93	277.86	54.5		40.0
229.09	302.69	54.8		37.9
251.19	329.51	55.2		35.8
275.42	359.18	55.5		33.7
302.00	390.06	56.1		31.6
331.13	423.91	56.6		29.4
363.08	458.48	57.4		27.3
398.11	494.42	58.3		25.1
436.52	532.76	59.3		22.8
478.63	572.01	60.6		20.5
524.81	612.95	62.0		18.2
549.54	634.33	62.7		17.0
575.44	655.74	63.6		15.8
602.56	677.58	64.4		14.6
630.96	700.04	65.3		13.3
660.69	723.05	66.2	0.04	12.1
691.83	746.28	67.1	0.05	10.8
724.44	769.96	68.1	0.07	9.5
758.58	793.54	69.2	0.08	8.2
794.33	818.61	70.3	0.10	6.9
831.76	844.18	71.4	0.13	5.6
870.96	869.50	72.6	0.16	4.2
912.01	895.47	73.8	0.20	2.8
954.99	921.44	75.1	0.25	1.4
1000.00	948.27	76.4	0.31	0.0
1047.13	974.99	77.8	0.39	−1.4
1096.48	1001.25	79.3	0.50	−2.9
1116.86	1011.86	79.9	0.56	−3.5
1137.63	1022.49	80.6	0.61	−4.1
1158.78	1034.49	81.1	0.66	−4.7
1180.32	1048.05	81.6	0.71	−5.3
1202.26	1062.06	82.0	1.08	−5.9
1224.62	1076.89	82.4	1.60	−6.4
1247.38	1092.34	82.7	2.07	−7.0
1270.57	1108.20	83.0	2.24	−7.6
1294.20	1124.27	83.4	2.26	−8.1
1318.26	1138.71	83.9	2.26	−8.7
1380.38	1173.19	85.2	2.26	−10.1
1445.44	1209.41	86.6	2.26	−11.5
1513.56	1246.94	87.9	2.26	−13.0
1584.89	1286.54	89.2	2.26	−14.5
1659.59	1327.06	90.6	2.26	−16.0
1737.80	1369.35	91.9	2.26	−17.5
1819.70	1413.47	93.2	2.26	−19.1
1905.46	1458.75	94.6	2.26	−20.7
1995.26	1505.33	96.0	2.26	−22.3
2089.30	1552.86	97.5	2.26	−23.9
2187.76	1601.24	99.0	2.26	−25.5
2290.87	1650.08	100.6	2.26	−27.2
2308.81	1657.33	100.9	2.26	−27.5

This table gives the number density (n_t), temperature (T), and methane mixing ratio ($n_{CH_4} \times 100/n_t$) as a function of the pressure level (p) for the nominal atmospheric model discussed in the text. Also provided is the local altitude (h) of the measurements relative to the 1-bar level. Note that n_t and n_{CH_4} include CH_4 molecules in the gas, liquid, and solid states. The percentage of CH_4 that is assumed to be in the condensed form reaches a maximum of 10% in the middle of the cloud (i.e., near the 1240-mbar level) and is negligible outside the cloud layer. The table was obtained from the ingress data by assuming a helium to hydrogen abundance ratio of 15/85.

geodetic surfaces may be calculated is available in an earlier publication [*Lindal et al.*, 1985].) Because of the rather limited data on cloud motion we believe the uncertainty in the polar radius is of the order of 20 km. The corresponding oblateness, $(R_{eq} - R_p)/R_{eq}$, is 0.02293 ± 0.00080. Note that these results are based on wind velocity data acquired in the southern hemisphere only and that seasonal variations in the atmospheric circulation might produce significant asymmetries between the northern and southern hemispheres.

The right-hand portion of Figure 8 shows the altitude of the 1-bar geoid relative to a reference geoid that has a polar radius of 24,973 km and whose shape is defined by the external gravity field and the uniform angular velocity given by the magnetic field rotation period. The slight altitude depression seen at the equator is the result of the subrotation in this region.

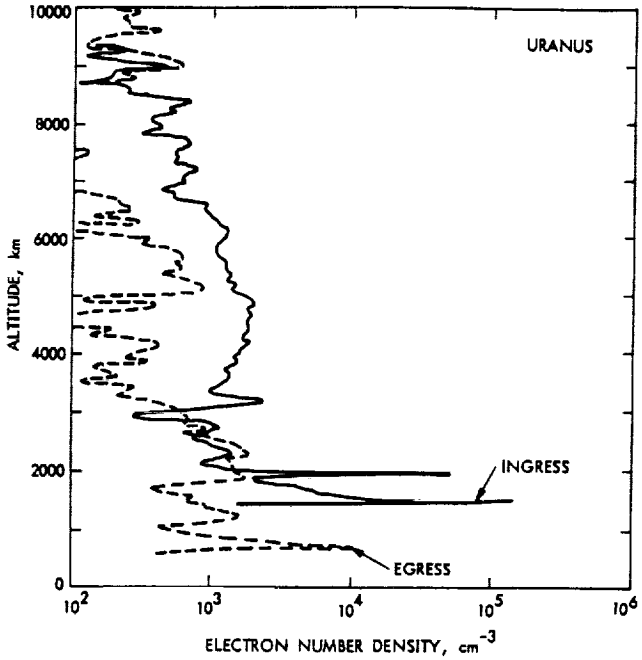

Fig. 7. Vertical electron number density profiles obtained from radio occultation measurements near the terminator in the equatorial ionosphere of Uranus. The ordinate scale gives the local altitude relative to the 1-bar level. As in previous measurements at Jupiter and Saturn the data show several sharp ionization layers which may consist of heavy ions of meteoric, ring, or satellite origin [*Chen*, 1981].

DISCUSSION

At the lowest level reached by the tracking link the atmospheric pressure was about 2.3 bars. For the nominal model the temperature at that level was 101 K with a 1σ uncertainty of 2 K due to the propagation of frequency noise, plus ephemeris, gravity, and pole direction uncertainties. As outlined in the previous section and in the appendix, the temperature computed from the radio data is also a function of the helium to hydrogen abundance ratio and the methane distribution. Changes in the helium to hydrogen ratio can be accounted for in a straight-forward manner by noting that the temperature is approximately proportional to the mean molecular mass in regions where the constituents are uniformly mixed. The methane effect is more complex, however, as discussed below.

Figure 9 shows the temperature and methane distribution for various models of the Uranian troposphere. These models, which are marked A, B, C, D, E, and F, were calculated from the ingress data by using a helium to hydrogen abundance ratio of 15/85. The approach used in deriving the profiles is outlined in the previous section and in the appendix. As discussed below, curves A and F provide lower and upper bounds on the temperature and methane distribution, and D corresponds to the intermediate and more plausible case which we refer to as the nominal model. For comparison the equatorial temperature profile acquired with the IRIS instrument [*Hanel et al.*, 1986] has also been included in the figure. Note from Figure 9 that methane does not have an appreciable effect on the radio temperature calculations above the 700-mbar level. The reason is, of course, that this region of the troposphere is too cold to contain a significant amount of CH_4 vapor.

Model A in Figure 9 was computed for the case of a methane free atmosphere. In this model the layer with the small refractivity scale height detected at the 1.2-bar level is interpreted in terms of a temperature inversion. Although similar inversions occur on Earth due to adiabatic warming in layers of subsiding air, this interpretation of the refractivity data seems less plausible than the other models, since infrared spectroscopic studies indicate that significant amounts of methane should be present at these pressure levels.

The other models depicted in Figure 9 were obtained by assuming that the base of the layer with the small refractivity scale height corresponds to the bottom of a methane cloud. Below the cloud the methane mixing ratio was taken to be constant and independent of altitude. Within the cloud layer the temperature lapse rate was set equal to the wet adiabat, and the percentage of CH_4 in the condensed form was assumed to reach a maximum value of 10% in the middle of the layer. (This 10% figure represents an average along a horizontal distance of the order of 100 km.) The different models containing CH_4 were derived by varying the height of the cloud top and the relative humidity (or the CH_4 partial pressure to saturation pressure ratio) above the cloud. For example, case B assumes that the cloud top is located in the middle of the layer with the small refractivity scale height and that there is no methane above the cloud. These assumptions produce a model with a temperature inversion above the cloud top. This interpretation is based on an analogy with the temperature inversion observed in the terrestrial trade winds which serves as a boundary or barrier between the ground trades that contain relatively moist, cold, and unstable air and the upper trades that are dry, warm, and stable. Model B has a methane mixing ratio of 1.1% below the cloud, and the relative humidity reaches a maximum value of 62% at the bottom of the cloud.

Model C is similar to model B except that the temperature inversion has been eliminated by raising the cloud top. Thus the entire layer with the small refractivity scale height is in this case assumed to be a region where the methane mixing ratio drops rapidly with increasing altitude and where the temperature lapse rate is equal to the wet adiabat. Model C has no methane above the cloud. The CH_4 mixing ratio below the cloud is 1.8%, and the relative humidity reaches a maximum value of 78% near the cloud base.

The nominal model is shown as case D in Figure 9. It is similar to model C except that the region between the cloud top and the tropopause is assumed to be 30% saturated with methane. Model D has a methane mixing ratio of 2.3% below the cloud, which corresponds to a carbon to hydrogen (C/H) abundance ratio of 1/76. Near the cloud base at the 1.3-bar level the relative humidity reaches a maximum value of 78%. Note that this relative humidity value represents an average over a resolution cell which extends a horizontal distance of the order of 100 km along the ray path that is tangentially grazing the base of the cloud.

Figure 10 shows the tropospheric temperature lapse rate for the nominal model. Also included are the adiabatic rates expected from theory for a mixture of hydrogen, helium, and methane where H_2 is either fully equilibrated or in "frozen" equilibrium. Below the cloud layer the nominal model has a lapse rate that falls between the adiabatic rates for equilibrium and "frozen" equilibrium hydrogen, and this may be due to ortho-para conversion. *Massie and Hunten* [1982] have shown, for instance, that conversion between ortho and para H_2 may reduce the adiabatic temperature lapse rate by about 10%.

As can be seen from Figure 10, the lapse rate for the nominal model is superadiabatic in a small altitude interval just above the cloud top. The model is not convectively unstable in this region, however, because the mean molecular mass rises

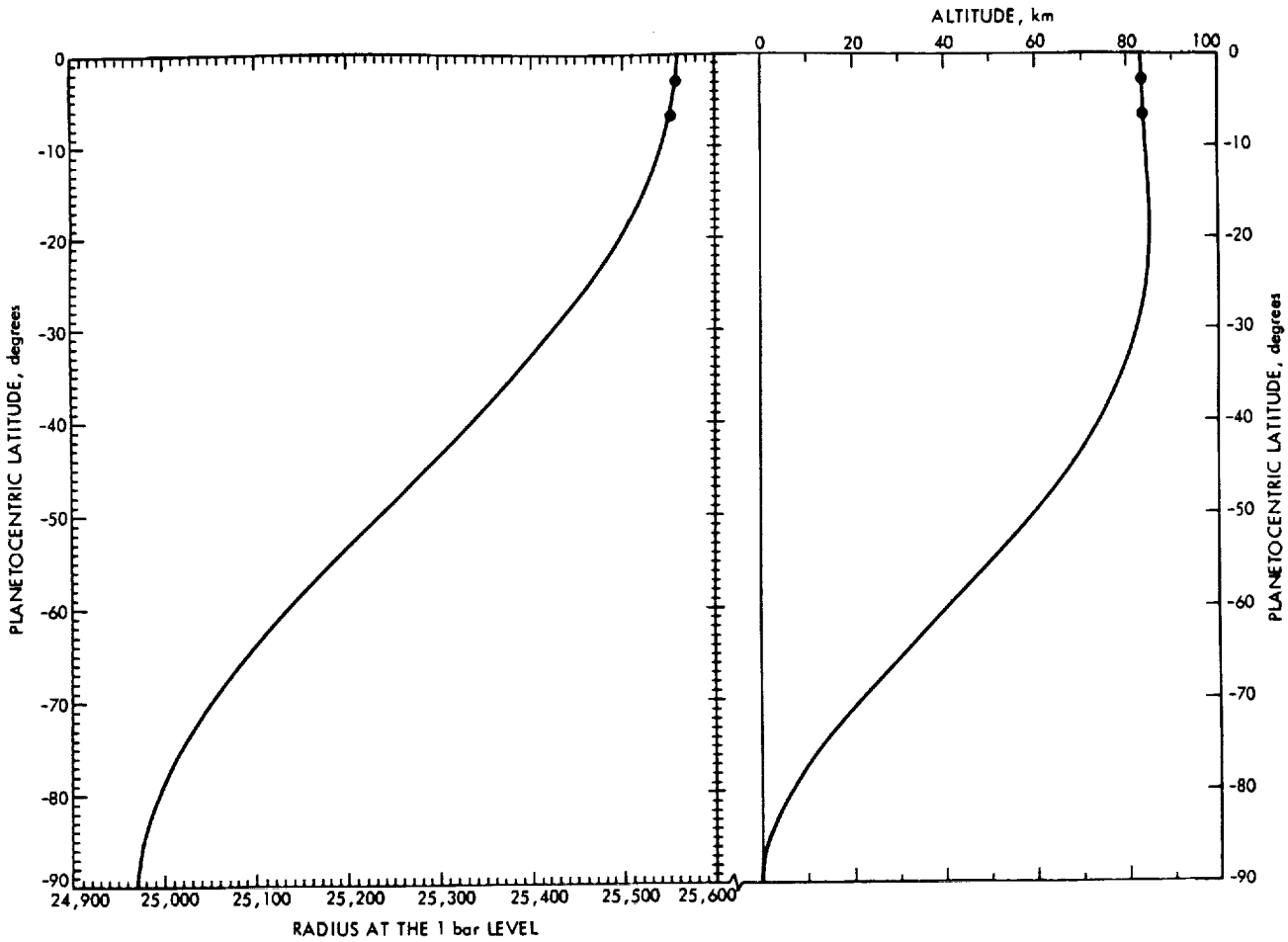

Fig. 8. The physical shape of Uranus. The discrete points in the left-hand portion of the chart show the radii observed at the 1-bar pressure level during ingress and egress, and the curve through these points represents the horizontal surface or geoid which best fits the radio occultation data. At the 1-bar level in the atmosphere the equatorial radius is 25,559 km. Extrapolation to the south pole using data on the gravity field (GM, J_2, and J_4) and the zonal winds observed with Voyager 2 gives a polar radius of 24,973 km. The right-hand portion of the figure shows the observed altitude of the 1-bar isobaric surface (discrete points) and the corresponding best fit geoid (solid curve). Altitudes are measured relative to a reference geoid that has a polar radius of 24,973 km and whose shape is defined by the external gravity field and a uniform angular velocity given by the magnetic field rotation period.

rapidly with decreasing altitude in the superadiabatic region. As a result of this a gas parcel displaced adiabatically upward will have a greater density than the ambient gas, even though its temperature is higher than the ambient temperature. A more detailed discussion of this stability criterion is provided in the appendix. Note also that a gas parcel in the superadiabatic region must be displaced several kilometers upward before condensation and precipitation can occur.

When the relative humidity above the cloud top is increased above 30%, it causes the temperature lapse rate in this region to rise and become more superadiabatic. For example, models E and F in Figure 9 were obtained by increasing the relative humidity above the cloud to 45% and 53%, respectively, and this produced peak lapse rates of about 1.4 and 2 K/km near the cloud top. However, a test based on the stability criterion given in the appendix shows that these models are not convectively unstable. If the relative humidity between the tropopause and the cloud top is raised to 54%, an abrupt discontinuity of the order of 200 K appears in the temperature profile. This temperature increase occurs because the temperature rises sufficiently fast with decreasing altitude to allow methane to become the principal constituent. It should be noted, however, that models where the region between the cloud and the tropopause is more than 53% saturated can be ruled out, since they lead to much higher temperatures and methane mixing ratios than indicated by Earth-based observations [*Wallace*, 1980; *Hunten*, 1984; *Appleby*, 1986]. Thus model F provides reasonable upper limits for the temperature and methane distribution in the region probed by the radio link.

Table 2 summarizes the characteristics of models B, C, D, E, and F that are germane to the discussion of the methane distribution. For example, the second column from the left lists the relative humidities assumed above the cloud top. The corresponding values derived for the relative humidity at the cloud base and the methane mixing ratio below the cloud are given in the two rightmost columns of the table.

As can be seen from Table 2, all atmospheric models have a relative humidity less than 100% in the cloud layer. Note that these humidity values represent averages over a resolution cell which extends horizontally on the order of 100 km in the north-south direction. Thus the relative humidities obtained here are not unrealistic for a cloud layer that has some gaps in it.

The nominal model is among the models that have the highest relative humidity at the cloud base. Increasing the relative humidity in the region between the cloud top and the

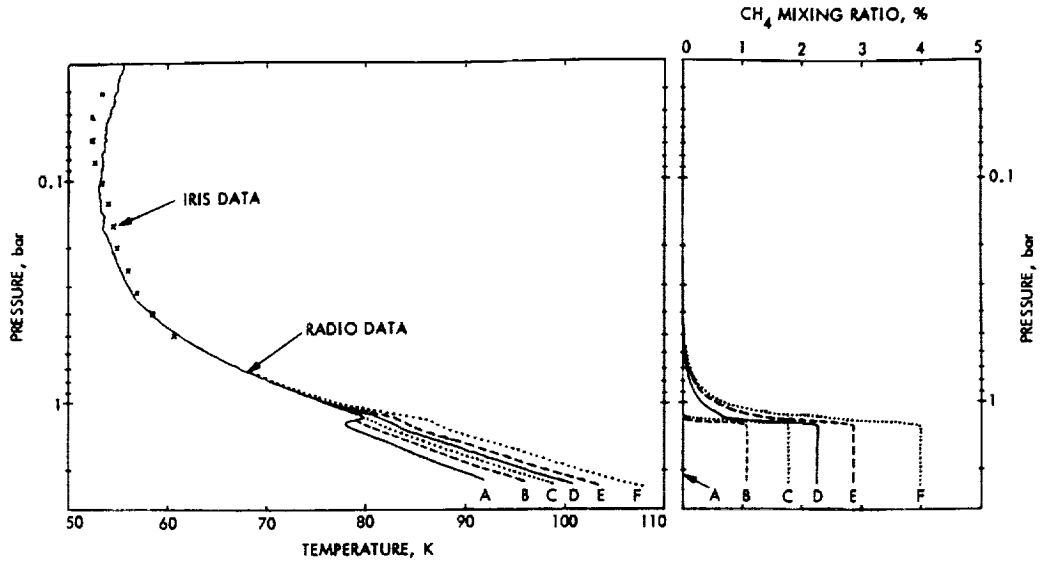

Fig. 9. Models for the troposphere of Uranus. The profiles were computed from the ingress data by using a helium to hydrogen abundance ratio of 15/85. Model A provides a lower bound for the temperature distribution. It was computed by assuming a methane free atmosphere. The remaining models were obtained by assuming that the layer with the small refractivity scale height observed at the 1.2-bar level is a methane cloud layer and by varying the altitude of the cloud top and the relative humidity above the cloud. Note that methane has a negligible effect on the temperature distribution above the 700-mbar level. Model D corresponds to the nominal model discussed in the text, and the profiles labeled F provide upper limits on the temperature and methane distribution. Also shown are the IRIS data acquired in the equatorial region of Uranus [*Hanel et al.*, 1986].

tropopause above 30% causes the relative humidity near the cloud base to begin to drop. The reason for this is that the temperature and therefore also the methane saturation pressure in the cloud increase when the relative humidity above the cloud top is increased.

Other parameters that affect the relative humidity in the cloud are the helium mixing ratio and the fraction of methane that is in the condensed phase. Lowering the helium mixing ratio reduces the temperature calculated from the radio data. This causes the methane saturation pressure to drop—which, in turn, raises the relative humidity in the cloud layer. (In order to raise the relative humidity at the cloud base to 100% for the nominal model it is necessary to reduce the helium mixing ratio at the tropopause to about 13%.) On the other hand, changing the fraction of methane that is assumed to be in the condensed form has relatively little effect on the pressure-temperature profiles computed from the refractivity data. It does, however, change the average vapor pressure and therefore also the average relative humidity within the resolution cell.

Finally, the precise value of the temperature lapse rate in the cloud layer is not known. However, since the cloud layer is quite thin, the uncertainty in this parameter has little effect on the pressure-temperature profiles computed from the radio data. In conclusion, it can therefore be stated that the major uncertainty affecting the interpretation of the radio data pertains to the relative humidity between the cloud and the 700-mbar level.

Model D in Figure 9 was chosen as the nominal model in this study because it maximizes the relative humidity at the cloud base, allows for a realistic humidity above the cloud top, and provides for a good fit with the IRIS data. (Although the equatorial spectra taken with the IRIS instrument—because of high emission angles—do not provide a strong constraint on the methane distribution, it should be noted that relative humidity values in the 0–30% range appear to provide the best fit between the radio and infrared data in the region near the cloud top [*Conrath et al.*, this issue].) Thus on the basis of these criteria one would conclude that the methane mixing ratio below the cloud probably falls in the middle of the range given in Table 2. This conclusion is in good agreement with studies of microwave radiation from Uranus which indicate a methane mixing ratio in the deep atmosphere of about 2% [*Orton et al.*, 1986].

The global circulation of the Uranian atmosphere is expected to produce a downdraft in the equatorial region [*Read*, 1986; *Flasar et al.*, this issue] that may bring gas with a low

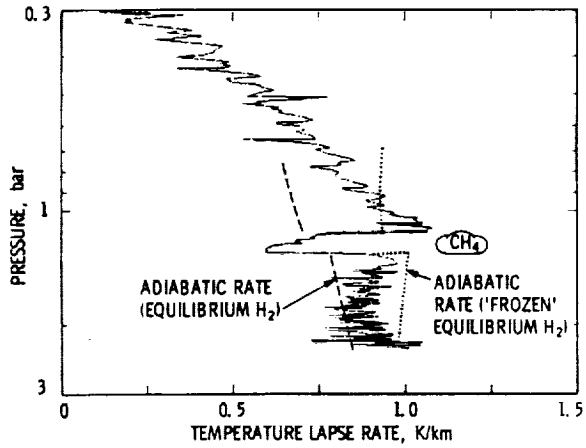

Fig. 10. Temperature lapse rate versus pressure level for the nominal model. The corresponding temperature profile is shown as curve D in Figure 9. Also shown are the adiabatic lapse rates expected from theory for the nominal model when H_2 is either fully equilibrated or in "frozen" equilibrium. Convection may be the dominant mechanism of vertical heat transport below the cloud top, and radiative transfer may dominate above this level.

TABLE 2. Characteristics of Atmospheric Models Containing CH_4

Model	Relative Humidity[a] Above Cloud Top, %	Relative Humidity at Cloud Base,[b] %	Methane Mixing[c] Ratio Below Cloud, %
B	0	62	1.1
C	0	78	1.8
D	30	78	2.3
E	45	76	2.9
F	53	72	4.0

[a]Relative humidity is defined here as the ratio between the partial pressure and the saturation pressure of CH_4 at the same temperature.

[b]In the models discussed here the maximum relative humidity occurs at the cloud base. The numerical values listed in this column represent averages over a horizontal distance of the order of 100 km.

[c]Mixing ratio by number density.

methane content down to the 1-bar level. This effect together with weak convection due to a small internal heat source may help explain why the equatorial troposphere is not saturated with CH_4 in the region above the cloud top. As mentioned earlier, we have modeled the methane distribution above the cloud by considering the effects of upward eddy diffusion in a downward gas current that might turn into a horizontal flow near the cloud top. This approach allowed us to utilize the radio data to put a constraint on the ratio between the downdraft velocity (v) and the eddy diffusion coefficient (K). Assuming steady state conditions with a zero net vertical flux of methane yields a value for v/K of the order of 10^{-6} cm^{-1} near the 1-bar pressure level for models similar to the nominal model. For an eddy diffusion coefficient of 10^5 cm^2/s, which is comparable to values obtained for the terrestrial troposphere [*Hunten*, 1975], this gives a downward gas velocity of 0.1 cm/s near the 1-bar level. It should be noted however, that both the value of K at the 1-bar level and its altitude dependence are quite uncertain. *Herbert et al.* [this issue] give a value of 10^4 cm^2/s at the Uranian turbopause. This is 2 orders of magnitude lower than the corresponding terrestrial value [*Hunten*, 1975]. If we scale down the value of K at the 1-bar level by a factor of 100 from 10^5 to 10^3 cm^2/s, we find that a downdraft velocity of the order of 0.001 cm/s would be required for models that have a methane distribution similar to the nominal model. This is comparable to the vertical velocity reported by *Flasar et al.* [this issue] for the tropopause region at 30°S latitude. Current studies of the scintillations observed on the radio link might provide more reliable information on the eddy diffusion coefficient in the Uranian troposphere.

Earlier radio occultation experiments at Jupiter and Saturn showed signal loss believed to be caused by absorption by ammonia vapor, and this limited the depth of the tropospheric measurements [*Lindal et al.*, 1981, 1985]. Although the microwave brightness spectrum of Uranus shows evidence of atmospheric NH_3 [*Gulkis and de Pater*, 1984], no clear sign of propagation loss was observed during the occultation of Voyager 2 by Uranus. This was to be expected, however, because the tropospheric region probed by the radio link is too cold to contain enough NH_3 vapor to produce detectable absorption.

As illustrated in Figure 6, the temperature distribution reached a minimum of 53 ± 1 K near the 100-mbar level, and this corresponds to the tropopause. Above the tropopause the data show thermal structure which bears some resemblance to earlier observations in the equatorial stratospheres of Jupiter and Saturn. However, there is an important difference between the profiles obtained at Uranus and those obtained previously at Jupiter and Saturn, and that is that the structure seen in Figure 6 appears to be essentially invariant to changes in location and local time, whereas the previous profiles show a great deal of variation. Thus while the data acquired at Jupiter and Saturn are suggestive of vertically propagating planetary waves [*Allison*, 1982, 1983; *Flasar*, 1986; *Lindal et al.*, 1981, 1985], the warm layers detected in the stratosphere of Uranus seem more likely to have been caused by other effects—perhaps absorption of solar radiation by aerosols.

Modeling and laboratory studies indicate that hydrocarbons such as acetylene (C_2H_2), biacetylene (C_4H_2), ethane (C_2H_6), and ethylene (C_2H_4) are being produced photochemically from methane in the stratosphere of Uranus [*Allen*

TABLE 3. Physical Data on Jupiter, Saturn, and Uranus

	Jupiter	Saturn	Uranus
Magnetic field rotation period[a]	9 hours 55 min 29.7 s	10 hours 39 min 22.4 s	17.24 hours
At the 1-bar pressure level			
Radius, km			
Equatorial	71492 ± 4	60268 ± 4	25559 ± 4
Polar[b]	66854 ± 10	54364 ± 10	24973 ± 20
Oblateness $(R_{eq} - R_p)/R_{eq}$	0.06487 ± 0.00015	0.09796 ± 0.00018	0.02293 ± 0.00080
Acceleration of gravity, m/s^2			
Equatorial[c]	23.12 ± 0.01	8.96 ± 0.01	8.69 ± 0.01
Polar	27.01 ± 0.01	12.14 ± 0.01	9.19 ± 0.02
Atmospheric temperature,[d] K	165 ± 5	134 ± 4	76 ± 2

[a]From *Davies et al.* [1983] and *Warwick et al.* [1986].

[b]For Jupiter and Saturn the polar radii are average values for the north and south poles. In the case of Uranus the value given here represents an extrapolation to the south pole.

[c]Values apply to objects corotating with the atmospheric gas.

[d]Temperature values assume that the atmospheres of Jupiter, Saturn, and Uranus consist of 89 ± 3%, 94 ± 3%, and 85 ± 3% hydrogen, respectively, with the remainder being mostly helium.

et al., 1980; *Atreya and Romani*, 1983; *Atreya*, 1984; *Romani and Atreya*, 1986; *Khare et al.*, 1986]. (The presence of acetylene and methane in this region has been confirmed experimentally by ultraviolet spectroscopy [*Broadfoot et al.*, 1986; *Encrenaz et al.*, 1986].) Precipitation and polymerization of these hydrocarbons may give rise to aerosols, and this could be the source of the stratospheric haze that was observed by the imaging and the photopolarimeter instrumentation on board Voyager 2 [*Lane et al.*, 1986; *Pollack et al.*, this issue; *Smith et al.*, 1986; *West et al.*, this issue]. Since aerosols are relatively effective absorbers of solar radiation [*Appleby*, 1986], it is also possible that they may be responsible for the warm layers seen in the radio profiles near the 4- and 12-mbar levels. These are also approximately the pressure levels where acetylene and ethane are expected to condense [*Atreya and Romani*, 1983; *Appleby*, 1986; *Pollack et al.*, this issue] and where the Voyager imaging data show abrupt increases in the aerosol extinction coefficients obtained at visible wavelengths [*Pollack et al.*, this issue].

Table 3 provides a summary of the more significant results of the atmospheric radio occultation measurements at Uranus. In order to allow comparisons, previous results from Jupiter and Saturn have also been included in the table.

APPENDIX: DERIVING DENSITY, PRESSURE, AND TEMPERATURE PROFILES

This appendix contains a brief outline of the procedure used in deriving vertical number density, pressure, and temperature profiles from the refractivity data acquired with the radio occultation experiment. As discussed in the data analysis section the refractivity profiles do not uniquely define the vertical changes in both the composition and the temperature of the atmosphere. In the formulation discussed below we have chosen to express the total number density, pressure, and temperature in terms of the refractivity, the helium to hydrogen abundance ratio, and the methane mixing ratio or mole fraction.

The refractivity (N) of a mixture of atoms and nonpolar molecules is to first order directly proportional to the total number density (n_t). (Note that N is defined here as the refractive index reduced by one and multiplied by 10^6.) When the composition of the atmosphere is known, the number density profile ($n_t(h)$) may be obtained from

$$n_t(h) = N(h)/\bar{\kappa}(h) \tag{1}$$

where h and $\bar{\kappa}(h)$ denote the local altitude and the mean molecular refractivity, respectively. The term "mean molecular refractivity" is defined here as the refractivity of the mixture when the number density is equal to 1 per unit of volume. To first order, $\bar{\kappa}(h)$ is proportional to the average electric dipole polarizability of the atoms and molecules that make up the atmosphere. For an atmosphere consisting of hydrogen, helium, and methane one has

$$\bar{\kappa}(h) = \kappa_{H_2} f_{H_2}(h) + \kappa_{He} f_{He}(h) + \kappa_{CH_4} f_{CH_4}(h) \tag{2}$$

where $f_{H_2}(h)$, $f_{He}(h)$, and $f_{CH_4}(h)$ represent the mixing ratios by number density. The numerical values of the constants κ_{H_2}, κ_{He}, and κ_{CH_4} are in units of cm^3, 0.5062×10^{-17}, 0.1302×10^{-17}, and 1.629×10^{-17}, respectively [*Essen*, 1953; *Orcutt and Cole*, 1967; *Bose et al.*, 1972]. Note that κ_{CH_4} is essentially invariant to changes in the state of methane and that $f_{CH_4}(h)$ accounts for methane molecules in the gas, liquid, and solid states. Also, κ_{H_2} is insensitive to changes in the ortho to para H_2 ratio [*Kolos and Wolniewicz*, 1967]. Thus unknown variations in the ortho to para ratio do not produce appreciable errors in the gas state profiles derived from the radio occultation measurements.

If the percentage of other constituents is negligible, one has

$$f_{H_2}(h) + f_{He}(h) + f_{CH_4}(h) = 1 \tag{3}$$

Since the turbopause is believed to be located well above the 0.1-mbar level [*Atreya and Romani*, 1983], one expects hydrogen and helium to be uniformly mixed in the pressure range of interest here. This implies that

$$f_{He}(h)/f_{H_2}(h) = \rho \tag{4}$$

where ρ, which represents the helium to hydrogen abundance ratio, is assumed to be independent of altitude.

Combining equations (2), (3), and (4) gives the following expression for $\bar{\kappa}(h)$ in terms of ρ and $f_{CH_4}(h)$

$$\bar{\kappa}(h) = \frac{\kappa_{H_2} + \rho\kappa_{He}}{1+\rho} + \frac{(1+\rho)\kappa_{CH_4} - \kappa_{H_2} - \rho\kappa_{He}}{1+\rho} f_{CH_4}(h) \tag{5}$$

Thus equations (1) and (5) may be employed to compute $n_t(h)$ from $N(h)$ when ρ and $f_{CH_4}(h)$ are known.

The vertical pressure distribution in the atmosphere ($p(h)$) may, in turn, be determined by utilizing the equation for hydrostatic equilibrium:

$$p(h) = \int_h^\infty n_t(h)\bar{m}(h)g(h)\,dh \tag{6}$$

where $\bar{m}(h)$ is the mean molecular mass and $g(h)$ is the local acceleration of gravity given by the external gravity field and the zonal wind velocities [*Lindal et al.*, 1985]. By using equations (3) and (4), $\bar{m}(h)$ may be expressed in terms of ρ and $f_{CH_4}(h)$ as follows:

$$\bar{m}(h) = \frac{m_{H_2} + \rho m_{He}}{1+\rho} + \frac{(1+\rho)m_{CH_4} - m_{H_2} - \rho m_{He}}{1+\rho} f_{CH_4}(h) \tag{7}$$

which together with equations (1), (5), and (6) allows $p(h)$ to be computed from $N(h)$, ρ, and $f_{CH_4}(h)$.

From the number density and the pressure one may determine the temperature ($T(h)$) of the gas. As in earlier studies we have adopted the following formulation for the equation of state:

$$T(h) = \frac{p(h)F_c}{kn_t(h)\,[1 - f_{CH_4}(h)f_c(h)]} \tag{8}$$

where k is Boltzmann's constant, $f_c(h)$ is the fraction of methane in the condensed form, and F_c is a temperature correction factor that is the reciprocal of the compressibility factor and accounts for deviations from the ideal gas law [*Lindal et al.*, 1983]. For the nominal model, F_c is within 0.1% of unity.

Hydrocarbon vapors and aerosols are not expected to have an appreciable effect on $\bar{\kappa}(h)$ and $\bar{m}(h)$ near the tropopause and in the stratosphere. Thus $\bar{\kappa}$ and $\bar{m}$ are presumably constant and independent of altitude in this region of the atmosphere. Using this assumption and combining equations (1), (6), and (8), one can show that the radio temperature ($T(h)$) in this case is independent of $\bar{\kappa}$ and directly proportional to $\bar{m}$:

$$T(h) = \frac{\bar{m}}{kN(h)} \int_h^\infty N(h)g(h)\,dh \tag{9}$$

where F_c has been set equal to 1 since the gas in this case is expected to behave as an ideal gas.

The gas state profiles presented in this report were obtained by following a procedure consisting of two basic steps. The first step involved computing $\bar{m}$ and ρ near the tropopause. This was done by initially neglecting methane and using equation (9) to calculate $T(h)/\bar{m}$ in the stratosphere and down to the tropopause. The mean molecular mass was estimated by solving for the value of $\bar{m}$ that provided best agreement between the radio and IRIS temperature profiles near the tropopause. Once $\bar{m}$ was obtained in this manner, the corresponding value for ρ was computed from equation (7) by noting that the term containing $f_{CH_4}(h)$ is negligible in this case.

Finally, complete vertical number density, pressure, and temperature profiles were computed for different assumptions regarding the methane distribution. This was done by starting at the top of the detectable stratosphere and proceeding downward, computing gas state parameters for one altitude level at a time. In the stratosphere the methane mixing ratio was set equal to the mixing ratio selected at the tropopause, and n, p, and T were computed from the refractivity data by using the formulas given above. From the tropopause and down to the cloud top, n, p, T, and f_{CH_4} were computed in an iterative manner at each altitude level either by assuming a constant relative humidity or by modeling the eddy diffusion of methane in a current of descending gas. Within the cloud layer the temperature lapse rate was assumed to be equal to the adiabatic rate expected when methane condensation occurs, and the refractivity data were instead used to determine f_{CH_4}, n, and p in an iterative manner. From the base of the cloud and down to the lowest level probed by the radio link the methane mixing ratio was kept constant, and the data were again utilized to compute n, p, and T. The results are summarized in Figures 5, 6, and 9.

The radio data indicate an upper limit of about 53% for the relative humidity above the cloud top. The reasoning leading to this limit is as follows. For relative humidity values less than 53% there are three real solutions for the gas state parameters at each altitude level. The solution giving the lowest T and f_{CH_4} was used in computing the profiles in this paper because it is the only solution that is in reasonable agreement with infrared spectroscopic studies. Increasing the relative humidity above 53% causes the number of real solutions to drop from three to one in the region near the cloud top, and the remaining solution yields a composition consisting primarily of methane and a gas temperature of several hundred Kelvin. This implies that the gas above the cloud was less than 53% saturated with methane in the area probed by the radio link—since higher relative humidity values result in a large discrepancy with infrared observations.

Another parameter of interest is the maximum temperature lapse rate that one can have above the cloud top before this region becomes convectively unstable. Since the region of interest here is not saturated with methane, we will simplify the problem by using the ideal gas law approximation.

Consider an elemental gas parcel at the altitude h that has the same pressure (p), temperature (T), number density (n), and mean molecular mass ($\bar{m}$) as the surrounding gas. If the parcel is displaced adiabatically a distance dh upward, its new pressure ($p + dp$) will be equal to the pressure prevailing at the altitude $h + dh$. The new temperature of the gas parcel is $T + dT$. Using the first law of thermodynamics and the ideal gas law, one can show for an adiabatic change in the gas state that dT is related to dh by

$$dT = -(g/C_p)\, dh \tag{10}$$

where C_p is the specific heat of the gas at constant pressure.

The atmosphere is stable if the density of the displaced gas parcel is greater than the density of the ambient gas. This requires that

$$\frac{(p + dp)\bar{m}}{(T + dT)k} > \frac{(p + dp)(\bar{m} + d\bar{m})}{(T - \Gamma\, dh)k} \tag{11}$$

where Γ denotes the temperature lapse rate of the atmosphere. Solving for Γ and replacing dT with the expression given by equation (10) gives the following stability criterion:

$$\Gamma < \frac{g}{C_p} - \frac{T\, d\bar{m}}{\bar{m}\, dh} \tag{12}$$

Note that the term $d\bar{m}/dh$ is negative above the cloud layer on Uranus because the methane mixing ratio drops with increasing altitude. Thus the presence of methane is expected to increase the stability of this region. This effect might help explain why few plumes of rising cloud material were observed with the spacecraft imaging system.

Acknowledgments. The radio data discussed in this article were acquired through the coordinated efforts of the Voyager Project staff, the Deep Space Net personnel, the Radio Science Support Team, and the Radio Science Team. The support team consisted of S. Borutzki, M. Connally, P. Eshe, H. Hotz, S. Kinslow, R. Kursinski, K. Moyd, and D. Sweetnam (team leader). The science team consisted of J. D. Anderson, J. K. Campbell, T. A. Croft, V. R. Eshleman, D. P. Hinson, G. S. Levy, G. F. Lindal, E. A. Marouf, R. A. Simpson, D. N. Sweetnam, G. L. Tyler (team leader), and G. E. Wood. We thank the Voyager Navigation Team for providing the ephemeris data needed to analyze the occultation measurements, and the referees for helpful comments. Stimulating discussions with B. Conrath, F. M. Flasar, D. Gautier, A. P. Ingersoll, D. O. Muhleman, and R. A. West are gratefully acknowledged. The research described in this article was carried out at the Jet Propulsion Laboratory of the California Institute of Technology and at Stanford University under contracts with the National Aeronautics and Space Administration.

The Editor thanks F. M. Flasar and another referee for their assistance in evaluating this paper.

REFERENCES

Allen, M., J. P. Pinto, and Y. L. Yung, Titan: Aerosol photochemistry and variations related to the sunspot cycle, *Astrophys. J.*, *242*, L125–L128, 1980.

Allison, M. D., Dynamics of the Jovian atmosphere: Voyager infrared observations and diagnostic wave theory, Ph.D. dissertation, Rice Univ., Houston, Tex., 1982.

Allison, M. D., Planetary waves in Jupiter's equatorial atmosphere. *Bull. Am. Astron. Soc.*, *15*, 836, 1983.

Anders, E., and M. Ebihara, Solar system abundances of the elements, *Geochim. Cosmochim. Acta*, *46*, 2363–2380, 1982.

Appleby, J. F., Radiative convective equilibrium models of Uranus and Neptune, *Icarus*, *65*, 383–405, 1986.

Atreya, S. K., Aeronomy, Uranus and Neptune, *NASA Conf. Publ.*, *CP-2330*, 55–88, 1984.

Atreya, S. K., and P. N. Romani, Photochemistry and clouds of Jupiter, Saturn, and Uranus, in *Recent Advances in Planetary Meteorology*, edited by G. Hunt, Cambridge University Press, New York, 1983.

Baines, K. H., Interpretation of the 6818.9-A methane feature observed on Jupiter, Saturn, and Uranus, *Icarus*, *56*, 543–559, 1983.

Baines, K. H., and J. T. Bergstralh, The structure of the Uranian atmosphere: Constraints from the geometric albedo spectrum and H_2 and CH_4 line profiles, *Icarus*, *65*, 406–441, 1986.

Bergstralh, J. T., and K. H. Baines, Properties of the upper tropospheres of Uranus and Neptune derived from observations at "visible" to near-infrared wavelengths, Uranus and Neptune. *NASA Conf. Publ.*, *CP-2330*, 179–212, 1984.

Bose, T. K., J. S. Sochanski, and R. H. Cole, Dielectric and pressure virial coefficients of imperfect gases, V, Octopole moments of CH_4 and CF_4, *J. Chem. Phys.*, *57*, 3592–3595, 1972.

Broadfoot, A. L., et al., Ultraviolet spectrometer observations of Uranus, *Science*, *233*, 74–79, 1986.

Cameron, A. G. W., Elementary and nuclidic abundances in the solar system, in *Essays in Nuclear Astrophysics*, edited by C. A. Barnes, D. N. Schramm, and D. D. Clayton, Cambridge University Press, New York, 1982.

Chen, R. H., Studies of Jupiter's lower ionospheric layers, *J. Geophys. Res.*, *86*(A9), 7792–7794, 1981.

Conrath, B., D. Gautier, R. Hanel, G. Lindal, and A. Marten, The helium abundance of Uranus from Voyager measurements, *J. Geophys. Res.*, this issue.

Davies, M. E., V. K. Abalakin, J. H. Lieske, P. K. Seidelmann, A. T. Sinclair, A. M. Sinzi, B. A. Smith, and Y. S. Tjuflin, Report of the IAU working group on cartographic coordinates and rotational elements of the planets and satellites: 1982, *Celestial Mech.*, *29*, 309–321, 1983.

Edelson, R. E., B. D. Madsen, E. K. Davis, and G. W. Garrison, Voyager telecommunications: The broadcast from Jupiter, *Science*, *204*, 913–921, 1979.

Encrenaz, T., et al., A study of the upper atmosphere of Uranus using the IUE, *Astron. Astrophys.*, *162*, 317–322, 1986.

Eshleman, V. R., G. L. Tyler, J. D. Anderson, G. Fjeldbo, G. S. Levy, G. E. Wood, and T. A. Croft, Radio science investigations with Voyager, *Space Sci. Rev.*, *21*, 207–232, 1977.

Eshleman, V. R., D. P. Hinson, G. F. Lindal, and G. L. Tyler, Past and future of radio occultation studies of planetary atmospheres, paper presented at 26th COSPAR Plenary Meeting, Comm. on Space Res., Toulouse, France, 1986.

Essen, L., The refractive indices of water vapor, air, oxygen, nitrogen, hydrogen, deuterium and helium, *Proc. Phys. Soc. London, Sect. B*, *66*, 189–193, 1953.

Evans, J. V., and T. Hagfors, *Radar Astronomy*, McGraw-Hill, New York, 1966.

Flasar, F. M., Global dynamics and thermal structure of Jupiter's atmosphere, *Icarus*, *65*, 280–303, 1986.

Flasar, F. M., B. J. Conrath, P. J. Gierasch, and J. A. Pirraglia, Voyager infrared observations of Uranus' atmosphere: Thermal structure and dynamics, *J. Geophys. Res.*, this issue.

French, R. G., J. L. Elliot, and S. E. Levine, Structure of the Uranian rings, II, Ring orbits and widths, *Icarus*, *67*, 134–163, 1986.

Friedson, J., and A. P. Ingersoll, Seasonal meridional energy balance and thermal structure of the atmosphere of Uranus: A radiative-convective-dynamical model, *Icarus*, *69*, 135–156, 1987.

Gautier, D., B. Conrath, R. Hanel, and G. Lindal, The helium abundance in Uranus, *Bull. Am. Astron. Soc.*, *18*, 757, 1986.

Gulkis, S., and I. de Pater, A review of the millimeter and centimeter observations of Uranus, Uranus and Neptune, *NASA Conf. Publ.*, *CP-2330*, 225–262, 1984.

Hanel, R., et al., Infrared observations of the Uranian system, *Science*, *233*, 70–74, 1986.

Herbert, F., B. R. Sandel, R. V. Yelle, J. B. Holberg, A. L. Broadfoot, D. E. Shemansky, S. K. Atreya, and P. N. Romani, The upper atmosphere of Uranus: EUV occultations observed by Voyager 2, *J. Geophys. Res.*, this issue.

Hinson, D. P., Magnetic field orientations in Saturn's upper ionosphere inferred from Voyager radio occultations, *J. Geophys. Res.*, *89*, 65–73, 1984.

Hinson, D. P., and G. L. Tyler, Spatial irregularities in Jupiter's upper ionosphere observed by Voyager radio occultations, *J. Geophys. Res.*, *87*, 5275–5289, 1982.

Hinson, D. P., and G. L. Tyler, Internal gravity waves in Titan's atmosphere observed by Voyager radio occultation, *Icarus*, *54*, 337–352, 1983.

Houghton, J. T., *The Physics of Atmospheres*, p. 19, Cambridge University Press, New York, 1977.

Hunten, D. M., Vertical transport in atmospheres, in *Atmospheres of Earth and the Planets*, edited by B. M. McCormac, pp. 59–72, D. Reidel, Hingham, Mass., 1975.

Hunten, D. M., Atmospheres of Uranus and Neptune, Uranus and Neptune, *NASA Conf. Publ.*, *CP-2330*, 27–54, 1984.

Khare, B. N., T. Henry, W. R. Thompson, L. Flynn, C. Sagan, E. T. Arakawa, and P. Votaw, The Uranian stratosphere: Hydrocarbon gases and solids from coronal discharge, *Bull. Am. Astron. Soc.*, *18*, 765, 1986.

Kolos, W., and L. Wolniewicz, Polarizability of the hydrogen molecule, *J. Chem. Phys.*, *46*, 1426–1432, 1967.

Lane, A. L., et al., Photometry from Voyager 2: Initial results from the Uranian atmosphere, satellites, and rings, *Science*, *233*, 65–70, 1986.

Lindal, G. F., et al., The atmosphere of Jupiter: An analysis of the Voyager radio occultation measurements, *J. Geophys. Res.*, *86*(A10), 8721–8727, 1981.

Lindal, G. F., G. E. Wood, H. B. Hotz, D. N. Sweetnam, V. R. Eshleman, and G. L. Tyler, The Atmosphere of Titan: An analysis of the Voyager 1 radio occultation measurements, *Icarus*, *53*, 348–363, 1983.

Lindal, G. F., D. N. Sweetnam, and V. R. Eshleman, The atmosphere of Saturn: An analysis of the Voyager radio occultation measurements, *Astron. J.*, *90*(6), 1136–1146, 1985.

Lindal, G. F., J. R. Lyons, D. N. Sweetnam, V. R. Eshleman, D. P. Hinson, and G. L. Tyler, The atmosphere of Uranus: Results of the Voyager 2 radio occultation measurements, *Bull. Am. Astron. Soc.*, *18*(3), 756, 1986.

Massie, S. T., and D. M. Hunten, Conversion of para and ortho hydrogen in the Jovian planets, *Icarus*, *49*, 213–226, 1982.

Ness, N. F., M. H. Acuña, K. W. Behannon, L. F. Burlaga, J. E. P. Connerney, R. P. Lepping, and F. M. Neubauer, Magnetic fields at Uranus, *Science*, *233*, 85–89, 1986.

Orcutt, R. H., and R. H. Cole, Dielectric constants of imperfect gases, III, Atomic gases, hydrogen, and nitrogen, *J. Chem. Phys.*, *46*, 697–702, 1967.

Orton, G. S., and J. F. Appleby, Temperature structures and the infrared-derived properties of the atmospheres of Uranus and Neptune, Uranus and Neptune, *NASA Conf. Publ.*, *CP-2330*, 89–155, 1984.

Orton, G. S., M. J. Griffin, P. A. R. Ade, I. G. Nolt, J. V. Radostitz, E. I. Robson, and W. K. Gear, Submillimeter and millimeter observations of Uranus and Neptune, *Icarus*, *67*, 289–304, 1986.

Orton, G. S., D. K. Aitken, C. Smith, P. F. Roche, J. Caldwell, and R. Snyder, The spectra of Uranus and Neptune at 8–14 and 17–23 μm, *Icarus*, *70*, 1–12, 1987.

Owen, T., An identification of the 6800 A methane band in the spectrum of Uranus and a determination of atmospheric temperatures, *Astrophys. J.*, *146*, 611–613, 1966.

Pollack, J. B., K. Rages, S. Pope, M. Tomasko, P. N. Romani, and S. K. Atreya, Nature of the stratospheric haze on Uranus: Evidence for condensed hydrocarbons, *J. Geophys. Res.*, this issue.

Read, P. L., Super-rotation and diffusion of axial angular momentum, II, A review of quasi-axisymmetric models of planetary atmospheres, *Q. J. R. Meteorol. Soc.*, *112*, 253–272, 1986.

Romani, P. N., and S. K. Atreya, Polyacetylene photochemistry and condensation on Uranus, *Bull. Am. Astron. Soc.*, *18*, 758, 1986.

Sandel, B. R., F. Herbert, A. L. Broadfoot, J. B. Holberg, D. E. Shemansky, R. V. Yelle, and S. K. Atreya, Structure of the upper atmosphere of Uranus, *Bull. Am. Astron. Soc.*, *18*, 758, 1986.

Smith, B. A., et al., Voyager 2 in the Uranian system: Imaging science results, *Science*, *233*, 43–64, 1986.

Stone, E. C., and E. D. Miner, The Voyager 2 encounter with the Uranian system, *Science*, *233*, 39–43, 1986.

Stone, E. C., J. F. Cooper, A. C. Cummings, F. B. McDonald, J. H. Trainor, N. Lal, R. McGuire, and D. L. Chenette, Energetic charged particles in the Uranian magnetosphere, *Science*, *233*, 93–97, 1986.

Teifel, V. G., Methane abundance in the atmosphere of Uranus, *Icarus*, *53*, 389–398, 1983.

Trafton, L., Model atmospheres of the major planets, *Astrophys. J.*, *147*, 765–781, 1967.

Trafton, L., The atmospheres of the outer planets and satellites, *Rev. Geophys.*, *19*(1), 43–89, 1981.

Tyler, G. L., D. N. Sweetnam, J. D. Anderson, J. K. Campbell, V. R. Eshleman, D. P. Hinson, G. S. Levy, G. F. Lindal, E. A. Marouf, and R. A. Simpson, Voyager 2 radio science observations of the Uranian system: Atmosphere, rings, and satellites, *Science*, *233*, 79–84, 1986.

Wallace, L., The structure of the Uranus atmosphere, *Icarus*, *43*, 231–259, 1980.

Warwick, J. W., et al., Voyager 2 radio observations of Uranus, *Science*, *233*, 102–106, 1986.

West, R. A., A. L. Lane, C. W. Hord, L. W. Esposito, K. E. Simmons, R. M. Nelson, and B. D. Wallis, Temperature and aerosol structure

of the nightside Uranian stratosphere from Voyager 2 photopolarimeter stellar occultation measurements, *J. Geophys. Res.*, this issue.

V. R. Eshleman, D. P. Hinson, and G. L. Tyler, Center for Radar Astronomy, Stanford University, Stanford, CA 94305.

G. F. Lindal, J. R. Lyons, and D. N. Sweetnam, Jet Propulsion Laboratory, California Institute of Technology, 4800 Oak Grove Drive, Pasadena, CA 91109.

(Received January 29, 1987;
revised September 14, 1987;
accepted August 26, 1987.)